Fabrication and Studies of $MAPbI_3$ Perovskite Thin Films and Solar Cells

A thesis submitted

by

PILIK BASUMATARY
Roll No: 156151001

In partial fulfillment of the requirement for the award of the degree of
Doctor of Philosophy

School of Energy Science and Engineering
Indian Institute of Technology Guwahati
Guwahati - 781039, Assam, India

JUNE 2022

DECLARATION

The work contained in this thesis entitled **"Fabrication and Studies of $MAPbI_3$ Perovskite Thin Films and Solar Cells"** has been carried out by me under the supervision of Dr. Pratima Agarwal, Professor, Department of Physics and School of Energy Science & Engineering, Indian Institute of Technology, Guwahati, Assam, India. This thesis does not contain any materials previously submitted for the award of any degree or diploma.

Date: 01-06-2022

Pilik Basumatary
Roll No: 156151001
School of Energy Science & Engineering
Indian Institute of Technology Guwahati
Guwahati-781039, Assam, India

भारतीय प्रौद्योगिकी संस्थान गुवाहाटी
Indian Institute of Technology Guwahati
North Guwahati, Guwahati
PIN- 781 039, Assam State, INDIA
Phone: +91 361 2583000 Extn 2702, 2582702
Fax: +91 361 2690 762 (Institute), 2582749 (Department)

Dr. Pratima Agarwal
Professor
Department of Physics
E-mail:pratima@iitg.ernet.in

Dated: June 06, 2022

Certificate

This is certified that the work contained in this thesis entitled **"Fabrication and Studies of $MAPbI_3$ Perovskite Thin Films and Solar cells"** submitted by Mr. Pilik Basumatary, a Ph. D. student at School of Energy Science and Engineering, Indian Institute of Technology, Guwahati, Assam, India, for the award of the degree of Doctor of Philosophy has been carried out under my supervision. This work has not been submitted elsewhere for the award of any degree or diploma.

Pratima Agarwal

(Dr. Pratima Agarwal)

Dedicated
to
My Family and
Friends

ACKNOWLEDGMENTS

First of all, I would like to express my sincere gratitude to my thesis supervisor, Prof. Pratima Agarwal, for her constant guidance and support throughout my Ph. D. work. I am very thankful for her encouragement and motivation throughout my Ph.D. research work. She taught me a lot about approaching research problems, analyzing and understanding the results from an experimentalist perspective. I am very thankful to her for giving me an opportunity to work under her supervision and will remain ever grateful to her.

I am grateful to my doctoral committee members, Prof. Gaurav Trivedi (Chairman), Prof. Vimal Katiyar and Dr. Pankaj Kalita, for reviewing my research work regularly and sharing their guidance to enrich my research and dissertation. I extend my sincere gratitude to the former and present Head of the School of Energy Science and Engineering, Prof. P. Goswami, Prof. V.S. Moholkar and Prof. K. Mohanty, for their encouragement and allowing me to use the facilities in school throughout my research work. I am also thankful to all the faculty members and staff of the School of Energy Science and Engineering for their support and help. I also extend my sincere thanks to former and present Head of the Department of Physics, Prof. P. Poulose, Prof. S. Ghosh and Prof. P. Alagarsamy for extending their help in carrying out my research works. I also express my sincere thanks to Dr. S. Sarma, Technical Officer, Department of Physics for helping me during my thesis work and allowing me to use departmental facilities.

I am also grateful to Late. Prof. S.C. Agarwal, visiting faculty in the Department of Physics for valuable technical discussions on various topics related to research work. I am also thankful to all the staff of Central Instruments Facility, IIT Guwahati, for their help in using CIF facilities. I would like to thank Prof. P. K. Iyer, Department of Chemistry, for allowing me to use some of the facilities in his lab.

I am thankful to all my seniors, Dr. Himanshu S. Jha, Dr. Mukesh Singh, Dr. Lalhriatzuala, Dr. Ramakrisha Madaka, Dr. Asha Yadav, Dr. Venkanna Kanneboina, and my current lab mates Ms. Juhi Kumari, Mr. Manvendra Singh Gangwar, Ms. Jai Shree Bhardwaj, Mr. Himangshu Deka, Mr. Anterdipan Singh, Mr. Rahul, Mr. Tulsiram, Mr. Gaurav Singh, Mrs. Ranju Kumari, Mr. Rohan Ghosh and Ms. Vaishnavi Chouksey for

their help and cooperation during my research works. I would also like to thank past lab members Vivek, Shubhangi, Niharika, Ankit, Jaydeep, Jiten, Gaurav, Rakesh, Bhagwat, Dharmendra, Mahipal, Kaushalya, Jamal, Nisharg and Jay for their help during my research work and wonderful time shared with me. I am also thankful to all the research scholars of the School of Energy Science and Engineering and the Department of Physics for their various help during my research work.

I am thankful for having met supportive friends in the institute and outside. Their support and encouragement helped me to overcome setbacks. I greatly value their friendship and I sincerely appreciate them. I am fortunate to have my friends who have constantly encouraged me throughout my thesis work.

I am grateful to The Ministry of Education (MoE), Govt. of India, for the financial assistance in the form of a scholarship.

My parents' love and countless sacrifices afforded me this opportunity. I have no words to acknowledge them. I thank my wife Purabi, daughter Jaishnavi, my sisters Dolina and Jasmine and all other family members for their boundless love and support.

Pilik Basumatary
IIT Guwahati, India, June 2022

PREFACE

Hybrid metal halide perovskites are the new emerging materials that have been used in photovoltaic (PV) technology for the last decade. The hybrid perovskite materials have gained tremendous attention due to its several interesting optoelectronic properties and low fabrication cost. The perovskite solar cells have been one of the fastest-growing PV technology for the last few years, with the highest efficiency record of 25.7% in 2022. The fast progress in power conversion efficiency has attracted many researchers worldwide to explore this material class. Besides solar cells, the halide perovskites are also suitable for other optoelectronic devices such as light-emitting diodes and photodetectors. Despite several fascinating features of halide perovskite, a well-known issue in perovskite solar cells (PSC) is its instability to humidity. When exposed to moisture, the efficiency of PSC reduces drastically within a few hours or days due to the degradation of the halide perovskite, the absorber layer in PSC. However, the ability to withstand moisture depends on the perovskite composition and the deposition method used to some extent. Therefore, the motivation for the present thesis work has been to study $MAPbI_3$ thin films deposited using one-step and two-step deposition methods from the device application point of view. Another motivation was to optimize various parameters of $MAPbI_3$ perovskite (absorber) layer to achieve high-efficiency solar cells.

Based on these motivations, the following objectives of the present thesis work have been set.

- Deposition of perovskite thin films by one-step and two-step methods using thermal evaporation (vacuum technique), spin coating and dip coating to gain insight into the structural, optical and electrical properties of the perovskite thin films and check their stability in ambient moisture.
- Fabrication of planar $MAPbI_3$ perovskite based solar cells.
- Optimization of $MAPbI_3$ absorber layer parameters, such as bulk defect density, interface defects, and thickness using the Sentaurus-TCAD simulation tool for high-efficiency solar cells.

The present thesis contains seven (07) chapters. Chapter 1 introduces metal halide perovskite (MHP) material and MHP based solar cells. Chapter 2 describes the deposition process of $MAPbI_3$ thin films and the fabrication of solar cells. This chapter also briefly

describes different characterization techniques used to study different properties of $MAPbI_3$ thin films and the performance of fabricated solar cells. This chapter also details optimizing absorber layer parameters for $MAPbI_3$ perovskite solar cells using Sentaurus-TCAD simulation tool. Chapter 3 presents studies on the structural, optical, and electrical properties of the $MAPbI_3$ perovskite thin films deposited using a one-step solution method. A detailed study of luminescence features of $MAPbI_3$ perovskite thin films was carried out using photoluminescence (PL) and photoluminescence excitation (PLE) spectroscopy at varying excitation wavelength (λ_{ex}) and emission wavelength (λ_{em}) are also discussed in this chapter. Chapter 4 contains studies on the structural, optical, electrical properties and stability of the $MAPbI_3$ perovskite thin films deposited using the two-step method TE&DC (thermal evaporation and dip coating) and SC&DC (spin coating and dip coating). In addition, transient photocurrent measurements were done to study the charge transport and carrier recombination process in $MAPbI_3$ perovskite thin films at different illumination time duration (30-90 s) and temperatures (25-70 °C) at varying illumination intensity (100-1000 Wm^{-2}). Chapter 5 presents the fabrication and studies on p-i-n planar heterojunction $MAPbI_3$ PSC. The influence of absorber layer thickness variation on the performance of one-step deposited PSC (*FTO/PEDOT:PSS/$MAPbI_3$/PCBM/BCP/Ag*) and the role of a thin ITO layer as a passivation layer in the two-step deposited PSC (*ITO/PEDOT:PSS/$MAPbI_3$/PCBM/ITO/Ag*) are discussed in this chapter. Chapter 6 presents the optimization of absorber layer parameters for high-efficiency $MAPbI_3$ solar cells with n-i-p (*FTO/SnO_2/$MAPbI_3$/Spiro-OMeTAD/Ag*) and p-i-n (*FTO/ PEDOT:PSS/$MAPbI_3$/PCBM/Ag*) configurations using Sentaurus-TCAD simulation software. Chapter 7 is the final chapter of the thesis, which summarizes the contents of each chapter and gives the conclusion of the work reported in the thesis. The thesis work is concluded with the scope for future work from the present investigation.

LIST OF ABBREVIATIONS AND SYMBOLS

AFM	Atomic force microscopy
Ag	Silver
Al	Aluminum
Ar	Argon
Au	Gold
CB	Conduction band
DC	Dip coating
Ec	Conduction band energy
EQE	External quantum efficiency
ETL	Electron transport layer
FESEM	Field emission scanning electron microscopy
Fig.	Figure
FWHM	Full width at half maximum
FTO	Fluorine-doped tin oxide
HTL	Hole transport layer
HOMO	Highest occupied molecular orbital
ITO	Indium tin oxide
LUMO	Lowest unoccupied molecular orbital
PCE	Power conversion efficiency
PL	Photoluminescence
PLE	Photoluminescence excitation
PP	Process pressure
PSC	Perovskite solar cells
R	Reflectance
R^2	Goodness of fit
RF	Radio frequency
RH	Relative humidity
SCCM	Standard cubic centimeter per minute
SE	Spectroscopic ellipsometry
Si	Silicon
TCO	Transparent conducting oxide
TE	Thermal evaporation
UV-Vis-NIR	Ultraviolet visible near infrared
VB	Valence band
XRD	X-Ray diffraction
A	Amplitude parameter
d	Separation between electrodes
d_{xrd}	Crystallite size
E_a	Activation energy
E_g	Optical bandgap
eV	Electron volt

FF	Fill factor
h	Planck's constant
I	Current
I_d	Dark current
J	Current density
J_o	Saturation current density
J_{sc}	Short circuit current density
J_{ph}	Photocurrent density
k	Extinction coefficient
K	Kelvin
K_B	Boltzmann constant
l	Length
M	Molecular weight
n	Refractive index
P_{in}	Input power
q	Electron charge
R_s	Series resistance
R_{sh}	Shunt resistance
t	Film thickness
T	Temperature in kelvin
V	Voltage
V_{oc}	Open circuit voltage
α	Absorption coefficient
β	Full width at half maximum
η	Efficiency
θ	Bragg's angle
λ	Wavelength
λ_{ex}	Excitation wavelength
λ_{em}	Emission wavelength
μ	Carrier mobility
ν	Frequency
ρ	Resistivity
σ	Conductivity
σ_d	Dark conductivity
σ_{ph}	Photo conductivity
τ	Decay time constant
Φ_e	Evaporation rate
$\sim$	Approximately
^oC	Degree celsius

CONTENTS

LIST OF FIGURES

LIST OF TABLES

CHAPTER 1

Introduction

The worldwide energy demand is continuously rising with the growth of the human population. Conventional energy resources like coal, oil, and natural gas have been extensively used to meet the rising energy demand. On the other hand, the extensive use of such conventional energy resources causes severe environmental issues and affects human health in various ways. So, there is a requisite for alternate sustainable energy sources to meet the high energy demand for the sustainable growth of human civilization. Renewable energy resources like solar energy, wind energy and tidal energy are sustainable, environmentally friendly and do not cause environmental pollution after use. Among the various renewable energy resources, solar energy is an abundant form of energy accessible at different geographical locations. Each year, the total sunlight energy reaching the earth's surface is 3,400,000 EJ which is 7000 to 8000 times annual

global primary energy consumption [1]. Thus, the well-established photovoltaic (PV) technology that converts solar energy into electricity has a great potential to satisfy the huge energy demand. Photovoltaic technology plays a significant role in the sustainable development and utilization of renewable energy sources to reduce carbon emissions. The advances in PV technology have improved efficiency, decreased the cost, and increased the reliability of photovoltaic systems. Remarkably, the use of solar PV technology for solar energy harvesting has been rapidly rising worldwide because solar PV panels are reliable and easy to install without any complex moving parts. However, further improvements can be made to enhance the economic feasibility of solar PV. A well-known candidate in advancing photovoltaics is the halide perovskite-based solar cells. In recent years, the emerging hybrid metal halide perovskite (MHP) materials have been studied extensively and found to be a promising low-cost alternate material for solar PV applications [2-9].

1.1 Hybrid metal halide perovskite solar cells (PSC)

The term 'perovskite' refers to the materials having the same stoichiometry as the mineral $CaTiO_3$ (calcium titanium oxide). The halide perovskites used as absorber layers in solar cells are typically called 'hybrid' because they are composed of organic and inorganic components. A typical PSC generally consists of an electron transport layer (ETL) covered with a light absorber (perovskite) layer widely known as the active layer and a hole transport layer (HTL). In 2009, Miyasaka's team first used the hybrid perovskite ($CH_3NH_3PbI_3$, $MAPbI_3$) as an absorber layer in a solar cell based on the architecture of a dye-sensitized solar cell (DSSC), which showed a power conversion efficiency (PCE) of 3.8% [10]. Following the same architecture, Park et al. could improve the PCE up to 6.5% in 2011[11]. The perovskite layer had a dissolution issue while using liquid electrolytes

in PSC fabrication. In 2012 Gratzel et al. fabricated PSC using spiro-MeOTAD (2,2′ ,7,7′ -tetrakis (N,N-di-p-methoxyphenylamine)-9,9′-spirobifluorene) hole transport layer (HTL), which was earlier developed for organic LED and solid-state DSSC [12, 13]. Usage of spiro-MeOTAD HTL increased the PSC stability and efficiency from 6.54% to 9.7% [14]. The drastic efficiency improvement using spiro-MeOTAD was an important breakthrough that accelerated the progress of PSC. It can be noted that most of the reported high-efficiency PSC are developed using spiro-MeOTAD as HTL. Subsequently, higher efficiencies were achieved by optimizing device fabrication parameters and using new deposition techniques such as the two-step method and thermal co-evaporation [15, 16]. Various modifications in growth techniques for depositing uniform perovskite films with large grain sizes (~1 μm) and low non-radiative recombination losses in the perovskite layer have facilitated for higher cell efficiencies [17-19]. Along with material selection, different treatments such as structure modification [20, 21], thermal annealing [22], variation of substrate temperature [23], precursor concentrations, solvent treatment [24], and mixed solvents [18] have also been investigated to improve the efficiency of PSC. However, control over the structure, grain size, and degree of crystallinity remains a key scientific challenge in achieving high-performance devices [19, 25-29].

In 2022, perovskite solar cells reached a high-efficiency record of 25.7%, close to the efficiencies of inorganic solar cells [30]. Because of the rapidly rising high-efficiency records in the last few years, hybrid perovskite semiconductors and perovskite solar cells have gained tremendous attention worldwide. The field of PSC is exploding, with newly engineered materials such as fully inorganic perovskites, lead-free perovskites, being used as photo absorbers. In addition to solar cells, the halide perovskites are also found suitable for other optoelectronic devices such as light-emitting diodes (LED), photodetectors and lasers [31-37].

1.2 Properties of hybrid metal halide perovskite (MHP)

1.2.1 Structure of hybrid metal halide perovskite

The hybrid halide perovskite compounds have the general crystal structural formula ABX_3 [4, 38], typically consist of an organic cation, A = methylammonium ($CH_3NH_3^+$); formamidinium ($CH_3(NH_2)^{2+}$), a divalent metal, B = (Pb^{2+}; Sn^{2+}) and halide X = (Cl^-; Br^-; I^-). The single halide perovskite $MAPbI_3$ and the mixed halide perovskites $MAPb(I_{1-x}Br_x)_3$ and $MAPb(I_{1-x}Cl_x)_3$ ($0 \leq x \leq 1$) are often used as absorber materials in perovskite solar cells (PSC) [24, 39, 40]. The cubic crystal structure of a halide perovskite material is as shown in Fig. 1.1.

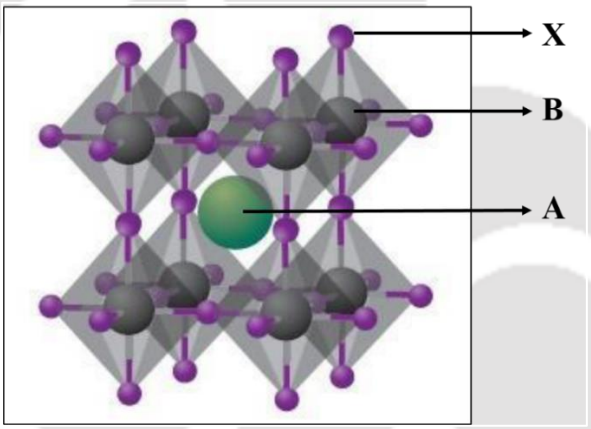

Figure 1.1: *Structure of a cubic metal halide perovskites with the formula ABX_3. The organic or inorganic cations occupy the center position A (green, large circle), whereas metal cations and halides occupy the position B (grey, medium circle) and position X (purple, small circle) [38]*

Scheffler and co-workers in 2019 have introduced a tolerance factor (τ) to predict a stable perovskite structure with better accuracy than the Goldsmith tolerance factor introduced earlier [9, 41]. The τ relation is given in Eq. 1.1, where the value of $\tau < 4.18$ indicates a stable perovskite structure.

$$\tau = \frac{r_X}{r_B} - n_A\left(n_A - \frac{{}^{r_A}/_{r_B}}{ln({}^{r_A}/_{r_B})}\right) \quad (1.1)$$

Where n_A is the oxidation state of A, r is the ionic radius of ion, and $r_A > r_B$ by definition.

The tolerance factor τ has an overall accuracy of 92% for predicting the probability of practically achieving a stable perovskite structure. Perovskite structural phase change occurs with the temperature variation. The $MAPbI_3$ ($CH_3NH_3PbI_3$) perovskite has a cubic phase above 327 K, which changes to a tetragonal phase from 162 K to 327 K and orthorhombic phase below 162 K [6, 42]. It has been found that the PCE of PSC is directly related to perovskite's crystal orientation. In the case of $MAPbI_3$ perovskite, the CH_3NH_3 does not contribute to the optical and electronic response, but it helps to their structural cohesion [43]. The metal-halide mainly governs the optoelectronic properties of ABX_3 perovskite because the valence band and the conduction band are formed by the combination of the metal and the halide orbitals [44]. Although the A-site cation does not directly contribute to the band edge energy levels, lattice contraction and octahedral tilting can indirectly impact the band positions [45]. The lattice contraction increases the metal halide orbital overlap, which raises the bands to shallower energy and hence decreases the bandgap. On the other hand, the octahedral tilting reduces the metal-halide orbital overlap, thus pushing the bands to deeper energy levels and the bandgap increases. The perovskite layer's proper crystal orientation at the interface with suitable charge transport layers results in higher short circuit current density and PCE [46].

1.2.2 Optoelectronic properties of hybrid metal halide perovskite

MHP exhibits an impressive cell performance due to its ideal optoelectronic properties, such as a direct bandgap, a strong absorption coefficient of ~10^5 cm^{-1}, and long carrier diffusion lengths (~1 µm) [5, 47, 48]. Other exciting features of MHP are weak exciton binding energy of ~10 meV, the high carrier mobility of ~25 $cm^2V^{-1}s^{-1}$, and low charge recombination rate on microseconds time scale [49-51]. The crystallization process of perovskite ends quickly in seconds with large grain growth up to ~1 µm, which is

beneficial for achieving high-efficiency PSC [19]. These inherent properties make MHP an excellent absorber material for solar cells that convert a significant portion of the visible spectrum into photocurrent and exhibit good cell performance. Moreover, the optical bandgap of halide perovskite can be tuned by varying the ratio of two different halides in the mixed-halide perovskite compounds [52]. For instance, the bandgap of $MAPb(I_{1-x}Cl_x)_3$ can be tuned from 1.6 to 3 eV by varying the ratio of I and Cl [53]. Similarly, in the case of $MAPb(I_{1-x}Br_x)_3$ and $MAPb(Br_{1-x}Cl_x)_3$, the bandgap can be tuned from 1.6 to 2.3 eV and 2.42 to 3.16 eV, respectively [54, 55]. Depending on the halide ratio variation, the mixed-halide perovskite exhibits different photovoltaic performance and stability due to its modified structural and optical properties [52]. The mixed-halide $MAPbI_{3-x}Cl_x$ perovskite has diffusion lengths greater than 1 μm; in contrast, the single halide $MAPbI_3$ perovskite has electron-hole diffusion lengths of ~100 nm [48]. Therefore, the device with $MAPbI_{3-x}Cl_x$ as an active layer showed higher PCE compared to $MAPbI_3$ based PSC. The high bandgap perovskites can be stacked as a top cell with other solar cells for fabricating tandem solar cells and blue LED [55, 56]. The reported high short circuit current density (J_{sc}) and open-circuit voltage (V_{oc}), along with the high efficiency of PSC, are comparable with stable inorganic solar cells, and these notable features have attracted many researchers globally to explore MHP materials [57-60]. The feasibility of using different compatible organic charge transport layers have also encouraged to explore many of the available materials conventionally used for organic solar cells.

1.3 Structure of perovskite solar cells

A perovskite solar cell (PSC) consists of a perovskite absorber layer sandwiched between two layers, namely the electron transport layer and the hole transport layer, to transport only one type of carrier (and block the other) to the respective electrode as shown in Fig.

1.2 [10]. The typical device configuration of PSC is: FTO-coated glass/ETL/perovskite/HTL/Ag or Au electrode [6, 11, 18].

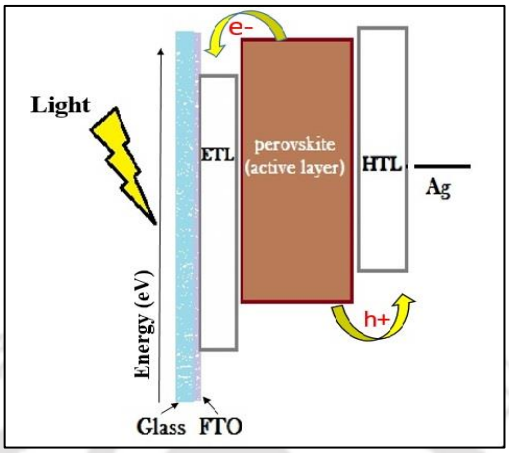

Figure 1.2: *Typical structure of a perovskite solar cell. The perovskite absorber layer is between ETL and HTL on FTO coated glass substrate with Ag as a top metal electrode. ETL- electron transport layer, HTL- hole transport layer, and FTO- Fluorine doped tin oxide*

The evolution of PSC structures is shown in Fig. 1.3(a-c). The Fig. 1.3(a) shows the original architecture mesoscopic(mp) n-i-p structure of PSC [10, 61, 62] having the device configuration of FTO/c-TiO_2/mpTiO_2(ETL)/perovskite/HTL/metal electrode. It is still a widely used device structure to fabricate high-performance PSC [63]. For this structure, the device fabrication starts with ETL deposition (E.g., mp-TiO_2 or mp-SnO_2) on transparent conductive oxides (FTO or ITO, Indium-doped tin oxide) coated glass substrate. In the next step, the perovskite absorber layer is deposited (by using one-step or two-step method) over the ETL, after that, a thin layer of HTL (E.g.- spiro-MeOTAD) is deposited on the perovskite layer, and finally, metal (Ag or Au) electrode is evaporated on HTL to complete the device stack. The planar n-i-p structure is similar to that of the mesoscopic n-i-p structure but without mesoporous TiO_2, as shown in Fig. 1.3(b) [16, 17]. The inverted planar (p-i-n) device structure has a device configuration of FTO/HTL/perovskite/ETL/metal electrode, as shown in Fig. 1.3(c) [59, 64, 65], where the device architecture is inverse of the n-i-p structure.

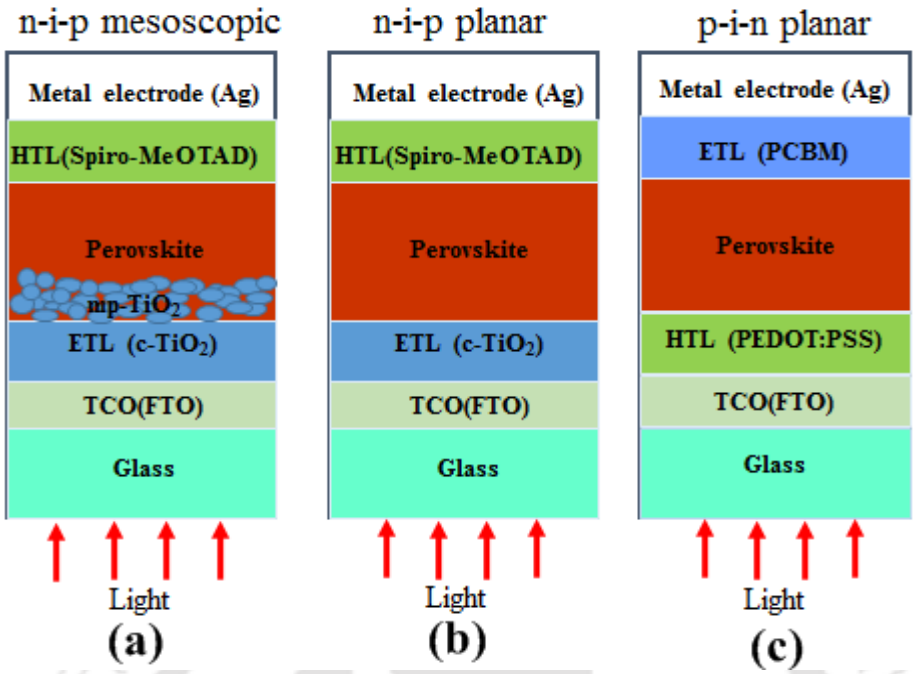

Figure 1.3: *Structural evolution of perovskite solar cells (a) mesoscopic n-i-p structure, (b) planar n-i-p structure and (c) planar p-i-n structure*

It is to be noted that the structure of a PSC is dependent on the choice of HTL and ETL materials for solar cell fabrication. Since PSC utilizes similar device architectures to DSSC and OSC(organic solar cells), these predecessors provide an understanding of physical, chemical and electronic properties of charge transport layers, electrode contacts, transparent conducting oxides (TCOs), and interfacial layers to be directly applied to PSC development [66]. Thus, PSC have another vital advantage of having the understanding of available applicable materials for device fabrication.

To further improve the stability and performance of PSC, interfacial layers are incorporated between the perovskite absorber and charge transport layers [67, 68]. These interfacial layers block carriers' reverse flow, reduce carrier recombination rate, assist carrier injection into the carrier selective layers, and maintain proper carrier extraction at the electrodes [69, 70]. However, extra interfacial layers increase the number of fabrication steps, total fabrication time and cost of PSC.

1.4 Challenges in perovskite solar cells

The primary drawback in PSC is the degradation of MHP in moisture, which deteriorates the PSC performance within a few hours or days. Therefore commercializing these solar cells with long-duration stability comparable to conventional inorganic solar cells is a major challenge [71, 72]. This degradation phenomenon of MHP is discussed in detail in the next section. Typically, solar cells operate in harsh environmental conditions such as high humidity and full solar irradiation with frequently varying weather conditions. In contrast, the PSC have a very short lifetime due to instability of the perovskite layer in high humidity conditions, which constrains the outdoor use of PSC [4]. Other factors influencing PSC's stability are perovskite composition, ambient temperature, and ultra-violet (UV) radiation in the atmosphere [73, 74]. Furthermore, the effects of interfacial defects, selective contacts and metal electrode stability, light-induced degradation, and instability under bias are the critical factors influencing PSC's stability. These factors are inevitable during device operation, even with perfect encapsulation to exclude humidity [54, 69, 75, 76].

In addition, lead (Pb) is toxic and harmful, so it has been a concern for the broad application of lead halide perovskite in photovoltaics. Finding a suitable alternative for Pb has been a prime target to address the toxicity issue. So lead-free PSC have also been fabricated using non-toxic tin(Sn) and bismuth(Bi) [3, 77]. However, the drawback of Sn^{2+} is the poor chemical stability as it quickly oxidizes to Sn^{4+} [78]. Though Bi-based perovskites have better stability than Pb-based perovskites, the bismuth perovskites-based PSC shows lower cell efficiencies than Pb-based PSC [79, 80]. Therefore, the challenge is to find the ideal perovskite composition to achieve stable and high-efficiency PSC. Moreover, maintaining the good photovoltaic properties in the PV module similar to devices fabricated in the research laboratories is another challenging task.

1.5 Degradation mechanism in halide perovskites

When exposed to moisture, the PCE of PSC falls drastically within a few hours or days due to the degradation of the halide perovskite absorber layer. Seok et al. reported that $CH_3NH_3PbI_3$ starts to degrade at relative humidity (*RH*) ~55%, which could be witnessed by the change in $CH_3NH_3PbI_3$ perovskite films from dark brown to yellow and becomes transparent [52]. In moisture (water molecule) and oxygen, the $CH_3NH_3PbI_3$ perovskite degrades irreversibly and produces various volatile products such as CH_3NH_2, HI and PbI_2 [81]. UV-induced degradation is also a well-known issue for mesoporous TiO_2 based PSC [82].

Moreover, metal electrode [silver (Ag) or gold (Au)] diffusion into the absorber layer of PSC is another cause of potential degradation. The volatile by-product hydrogen iodide (HI) escapes from the perovskite layer through the pinholes of the charge transport layer and it reacts with the top Ag electrode to form silver iodide (AgI), which further diffuses into the solar cell and deteriorates the device performance and stability [75, 83]. It is also experimentally explained that the reactive polyiodide [I_3^-] released during the degradation of iodide-based perovskite reacts with the Au electrodes in PSC to form the $[AuI_2]^-$ and $[AuI_4]^-$ complexes, which ultimately worsens the performance of PSC [84]. Another issue related to mixed halide perovskite is the halide phase segregation under illumination. Hoke et al. demonstrated the light-induced phase segregation in mixed halide perovskite $MAPb(Br_xI_{1-x})_3$, forming iodine (I) rich and bromine (Br) rich domains, which is reversible to the original unsegregated state again in dark conditions [54]. This phase segregation during illumination creates trap-states formed by the I-rich phases having lower bandgap value than the mixed halide perovskite, leading to a lower V_{oc} value than the estimated value. This kind of photo-induced instability can have severe implications for the operation of the devices based on this material.

1.6 Fabrication techniques of perovskite solar cells

PSC are generally fabricated by simple solution process techniques like spin coating, dip coating, blade coating, and spray coating at low temperatures (~100 °C) [23, 24, 85-87]. These solution techniques require relatively low processing time without using any complex high vacuum systems. Thus, the perovskite fabrication process consumes less energy and is inexpensive. At a lab-scale, spin-coating is the most widely used technique for PSC fabrication because: (i) it is a low-cost process for lab-scale, simple, and fast, (ii) film thickness can be controlled easily, and (iii) multi-layer deposition can be quickly done. However, this technique is not suitable for a large scale due to the non-uniformity in film thickness and material wastage. Other techniques, such as thermal evaporation and chemical vapor deposition, have also shown good cell results [16, 88].

It is also feasible for large-scale production of PSC by an industrial process such as roll-to-roll manufacturing and printing technology [85, 89, 90]. Currently, several research teams are scaling up the PSC fabrication process for mass production and high throughput [91, 92]. Large area deposition procedures such as blade coating, slot-die coating, inkjet printing, and spray coating for cost-effective processing and roll-to-roll printing techniques are being used for scaling up the PSC fabrication through optimized automation [85, 93-95]. The current research on PSC also focuses on improving the perovskite material's inherent stability, modifying the device architecture, and finding resilient encapsulating materials to protect the device from moisture effects to increase the performance and stability of PSC [76]. Since PSC are printable and require low-temperature processing [89], the overall manufacturing cost is low. Therefore, these low-cost PSC can be widely used to fulfill the high energy demand in the future.

1.7 Motivation and objectives

Halide perovskites have been the widely studied hybrid semiconductor material for photovoltaic applications due to their several exciting features, as discussed in the previous sections. The high efficiencies of halide perovskite solar cells attainable with simple and cost-effective fabrication techniques make them exceptionally unique in photovoltaic technology. These unique features have attracted the scientific community to explore these materials for various optoelectronic devices and contribute basic scientific knowledge concerned with the material property. Most of the recent reports are on the efficiency enhancement of the PSC using various halide perovskite formulation and fabrication techniques. Primarily, the performance of PSC depends on the deposition techniques used for preparing halide perovskite (absorber) thin films. Thus, it is essential to gain insight into the fundamental properties of halide perovskites synthesized using different applicable methods. Moreover, only a few reports deal with perovskite film deposition using vacuum techniques. These facts have motivated us to synthesize halide perovskite thin films and solar cells using different techniques, including the vacuum technique to deposit large area thin film with better qualities than the solution-processed films. Therefore, our motivation behind the thesis work is to fabricate and study methylammonium lead iodide ($CH_3NH_3PbI_3$ or $MAPbI_3$) perovskite thin films synthesized by different methods such as one-step and two-step methods and gain insight into the structural, optical and electrical properties of the halide perovskite thin films and then fabricate PSC. Another motivation is to optimize various parameters of $MAPbI_3$ perovskite layer using Sentaurus-TCAD simulation tool for achieving high-efficiency solar cells.

In view of the above mentioned points, the following objectives and work plan have been set for the thesis.

1. Synthesis of $MAPbI_3$ thin films by the one-step and two-step deposition techniques using thermal evaporation, spin coating, and dip coating methods.
2. Investigate the optical, structural and electrical properties and stability of the $MAPbI_3$ thin films using various characterization techniques.
3. Systematic investigation into the electrical transport properties of the thin films by transient current measurements in coplanar geometry at various measurement conditions.
4. Fabrication of $MAPbI_3$ perovskite-based solar cells and study their performance and stability.
5. Simulation of $MAPbI_3$ perovskite-based solar cells by optimizing absorber layer parameters such as bulk defect density, interface defects, and thickness for cell efficiency improvement.

1.8 Contents of thesis chapters

The present thesis contains seven (07) chapters.

Chapter 1 is the Introduction chapter.

Chapter 2 gives a brief description of details of sample preparation and different characterization techniques used for the analysis of the structural, morphological, optical, and electrical properties of $MAPbI_3$ thin films and the performance of solar cells. This chapter also details optimizing absorber layer parameters for $MAPbI_3$ perovskite solar cells using Sentaurus-TCAD simulation tool.

Chapter 3 contains studies on the structural, optical, and electrical properties of the $MAPbI_3$ perovskite thin films deposited using a one-step solution method. Studies on luminescence features of $MAPbI_3$ thin films carried out using photoluminescence (PL) and photoluminescence excitation (PLE) spectroscopy at varying excitation wavelength (λ_{ex}) and emission wavelength (λ_{em}) are also presented in this chapter.

Chapter 4 presents systematic studies on the structural, optical, electrical properties and stability of the $MAPbI_3$ thin films deposited using the two-step methods TE+DC (thermal evaporation and dip coating) and SC+DC (spin coating and dip coating). In addition, transient photocurrent measurements were done to study the charge transport and carrier recombination process in $MAPbI_3$ thin films at different illumination time duration (30-90 s) and temperatures (25-70 °C) at varying illumination intensity (100-1000 Wm^{-2}).

Chapter 5 presents the fabrication and studies on p-i-n planar heterojunction $MAPbI_3$ PSC. The influence of absorber layer thickness variation on the performance of one-step deposited PSC (*FTO/PEDOT:PSS/$MAPbI_3$/PCBM/BCP/Ag*) and the role of a thin ITO layer as a passivation layer in the two-step deposited PSC (*ITO/PEDOT:PSS/$MAPbI_3$/PCBM/ITO/Ag*) are discussed in this chapter.

Chapter 6 presents the optimization of absorber layer parameters such as bulk defect density, interface defects and thickness for high-efficiency solar cells with n-i-p (*FTO/SnO_2/$MAPbI_3$/Spiro-OMeTAD/Ag*) and p-i-n (*FTO/PEDOT:PSS/$MAPbI_3$/PCBM/Ag*) configurations using Sentaurus-TCAD simulation tool.

Chapter 7 is the final chapter of the thesis, which summarizes the contents of each chapter and gives the conclusion of the works reported in the thesis. The thesis work is concluded with the scope for future work from the present investigation.

1.9 References

1. Breeze, P., *Chapter 13 - Solar Power*, in *Power Generation Technologies (Third Edition)*, P. Breeze, Editor. 2019, Newnes. p. 293-321.
2. Mahapatra, A., et al., *A review of aspects of additive engineering in perovskite solar cells.* Journal of Materials Chemistry A, 2020. **8**(1): p. 27-54.
3. Yang, S., et al., *Recent advances in perovskite solar cells: efficiency, stability and lead-free perovskite.* Journal of Materials Chemistry A, 2017. **5**(23): p. 11462-11482.
4. Wang, D., et al., *Stability of perovskite solar cells.* Solar Energy Materials and Solar Cells, 2016. **147**: p. 255-275.
5. Fujiwara, H., et al., *Optical Characteristics and Operational Principles of Hybrid Perovskite Solar Cells.* physica status solidi (a), 2018. **215**(12): p. 1700730.
6. Kim, H.-S., S.H. Im, and N.-G. Park, *Organolead Halide Perovskite: New Horizons in Solar Cell Research.* The Journal of Physical Chemistry C, 2014. **118**(11): p. 5615-5625.
7. Lang, L., et al., *First-principles study on the electronic and optical properties of cubic ABX_3 halide perovskites.* Physics Letters A, 2014. **378**(3): p. 290-293.
8. Lin, Q., et al., *Electro-optics of perovskite solar cells.* Nature Photonics, 2015. **9**(2): p. 106.
9. Yin, W.-J., et al., *Halide perovskite materials for solar cells: a theoretical review.* Journal of Materials Chemistry A, 2015. **3**(17): p. 8926-8942.
10. Kojima, A., et al., *Organometal halide perovskites as visible-light sensitizers for photovoltaic cells.* J Am Chem Soc, 2009. **131**(17): p. 6050-6051.
11. Im, J.-H., et al., *6.5% efficient perovskite quantum-dot-sensitized solar cell.* Nanoscale, 2011. **3**(10): p. 4088-4093.
12. J. Salbeck , N.Y.b., J. Bauer by F. WeissGrtel , H. Bestgen *Low molecular organic glasses for blue electroluminescence.* Synthetic Metals, 1997. **91**
13. Hsu, C.-Y., et al., *Solid-state dye-sensitized solar cells based on spirofluorene (spiro-OMeTAD) and arylamines as hole transporting materials.* Physical Chemistry Chemical Physics, 2012. **14**(41): p. 14099-14109.
14. Kim, H.S., et al., *Lead iodide perovskite sensitized all-solid-state submicron thin film mesoscopic solar cell with efficiency exceeding 9%.* Sci Rep, 2012. **2**: p. 591.
15. Burschka, J., et al., *Sequential deposition as a route to high-performance perovskite-sensitized solar cells.* Nature, 2013. **499**(7458): p. 316-9.
16. Liu, M., M.B. Johnston, and H.J. Snaith, *Efficient planar heterojunction perovskite solar cells by vapour deposition.* Nature, 2013. **501**(7467): p. 395-8.
17. Huang, F., et al., *Gas-assisted preparation of lead iodide perovskite films consisting of a monolayer of single crystalline grains for high efficiency planar solar cells.* Nano Energy, 2014. **10**: p. 10-18.

18. Ahn, N., et al., *Highly Reproducible Perovskite Solar Cells with Average Efficiency of 18.3% and Best Efficiency of 19.7% Fabricated via Lewis Base Adduct of Lead(II) Iodide.* J Am Chem Soc, 2015. **137**(27): p. 8696-9.

19. Chen, J., et al., *Origin of the high performance of perovskite solar cells with large grains.* Applied Physics Letters, 2016. **108**(5): p. 053302.

20. Lee, M.M., et al., *Efficient Hybrid Solar Cells Based on Meso-Superstructured Organometal Halide Perovskites.* SCIENCE 2012. **338**: p. 643.

21. Tao, H., et al., *Perovskite solar cell based on network nanoporous layer consisted of TiO_2 nanowires and its interface optimization.* Journal of Power Sources, 2015. **290**: p. 144-152.

22. Xu, J., et al., *A rapid annealing technique for efficient perovskite solar cells fabricated in air condition under high humidity.* Organic Electronics, 2016. **34**: p. 84-90.

23. Nie, W., et al., *High-efficiency solution-processed perovskite solar cells with millimeter-scale grains.* Science, 2015. **347**(6221): p. 522.

24. Wang, X., et al., *Improving efficiency of planar hybrid $CH_3NH_3PbI_{3-x}Cl_x$ perovskite solar cells by isopropanol solvent treatment.* Organic Electronics, 2015. **24**: p. 205-211.

25. Im, J.-H., H.-S. Kim, and N.-G. Park, *Morphology-photovoltaic property correlation in perovskite solar cells: One-step versus two-step deposition of $CH_3NH_3PbI_3$.* APL Materials, 2014. **2**(8): p. 081510.

26. Almutawah, Z.S., et al., *Enhanced grain size and crystallinity in $CH_3NH_3PbI_3$ perovskite films by metal additives to the single-step solution fabrication process.* MRS Advances, 2018. **3**(55): p. 3237-3242.

27. Erin M. Sanehira, B.J.T.d.V., Philip Schulz, Matthew O. Reese, and K.Z. Suzanne Ferrere, Lih Y. Lin, Joseph J. Berry, and Joseph M. Luther, *Influence of Electrode Interfaces on the Stability of Perovskite Solar Cells: Reduced Degradation Using MoO_x/Al for Hole Collection.* Energy Letters, 2016.

28. Momblona, C., et al., *Efficient methylammonium lead iodide perovskite solar cells with active layers from 300 to 900 nm.* APL Materials, 2014. **2**(8): p. 081504.

29. Nukunudompanich, M., et al., *Dominant effect of the grain size of the $MAPbI_3$ perovskite controlled by the surface roughness of TiO_2 on the performance of perovskite solar cells.* CrystEngComm, 2020. **22**(16): p. 2718-2727.

30. *National Renewable Energy Laboratory Best Research Cell Efficiency Chart. https://www.nrel.gov/pv/assets/pdfs/best-research-cell-efficiencies-rev220126.pdf, 2021 [Accessed on 11 MAY 2022]*

31. Kim, H., et al., *Hybrid perovskite light emitting diodes under intense electrical excitation.* Nature Communications, 2018. **9**(1): p. 1-9.

32. Kim, Y.-H., H. Cho, and T.-W.J.P.o.t.N.A.o.S. Lee, *Metal halide perovskite light emitters.* Proc Natl Acad Sci U S A, 2016. **113**(42): p. 11694-11702.

33. Yang, X., et al., *Efficient green light-emitting diodes based on quasi-two-dimensional composition and phase engineered perovskite with surface passivation.* Nature Communications, 2018. **9**(1): p. 1-8.

34. Dou, L., et al., *Solution-processed hybrid perovskite photodetectors with high detectivity.* Nature Communications, 2014. **5**(1): p. 5404.

35. Guo, Y., et al., *Air-stable and solution-processable perovskite photodetectors for solar-blind UV and visible light.* The Journal of Physical Chemistry Letters, 2015. **6**(3): p. 535-539.

36. Xing, G., et al., *Low-temperature solution-processed wavelength-tunable perovskites for lasing.* Nature Materials, 2014. **13**(5): p. 476-480.

37. Zhu, H., et al., *Lead halide perovskite nanowire lasers with low lasing thresholds and high quality factors.* Nature Materials, 2015. **14**(6): p. 636-642.

38. Gratzel, M., *The light and shade of perovskite solar cells.* Nature Materials, 2014. **13**(9): p. 838-42.

39. Kulkarni, S.A., et al., *Bandgap tuning of lead halide perovskites using a sequential deposition process.* Journal of Materials Chemistry A, 2014. **2**(24): p. 9221-9225.

40. Yin, X., et al., *Moisture annealing effect on $CH_3NH_3PbI_3$ films deposited by solvent engineering method.* Thin Solid Films, 2017. **636**: p. 664-670.

41. Bartel, C.J., et al., *New tolerance factor to predict the stability of perovskite oxides and halides.* Science Advances, 2019. **5**(2): p. eaav0693.

42. Baikie, T., et al., *Synthesis and crystal chemistry of the hybrid perovskite $(CH_3NH_3)PbI_3$ for solid-state sensitised solar cell applications.* Journal of Materials Chemistry A, 2013. **1**(18): p. 5628.

43. Motta, C., et al., *Revealing the role of organic cations in hybrid halide perovskite $CH_3NH_3PbI_3$.* Nature Communications, 2015. **6**: p. 7026.

44. Yin, W.-J., T. Shi, and Y. Yan, *Unusual defect physics in $CH_3NH_3PbI_3$ perovskite solar cell absorber.* Applied Physics Letters, 2014. **104**(6): p. 063903.

45. Prasanna, R., et al., *Band Gap Tuning via Lattice Contraction and Octahedral Tilting in Perovskite Materials for Photovoltaics.* J Am Chem Soc, 2017. **139**(32): p. 11117-11124.

46. Sfyri, G., et al., *Study of perovskite solar cells synthesized under ambient conditions and of the performance of small cell modules.* Solar Energy Materials and Solar Cells, 2015. **134**: p. 60-63.

47. Song, Z., et al., *Pathways toward high-performance perovskite solar cells: review of recent advances in organo-metal halide perovskites for photovoltaic applications.* Journal of Photonics for Energy, 2016. **6**(2): p. 022001.

48. Stranks, S.D., et al., *Electron-hole diffusion lengths exceeding 1 micrometer in an organometal trihalide perovskite absorber.* Science, 2013. **342**(6156): p. 341-344.

49. Muljarov, E.A., et al., *Excitons in self-organized semiconductor/insulator superlattices: PbI-based perovskite compounds.* Physical Review B, 1995. **51**(20): p. 14370-14378.

50. Ponseca, C.S., Jr., et al., *Organometal halide perovskite solar cell materials rationalized: ultrafast charge generation, high and microsecond-long balanced mobilities, and slow recombination.* J Am Chem Soc, 2014. **136**(14): p. 5189-92.

51. Chen, X., et al., *Excitonic Effects in Methylammonium Lead Halide Perovskites.* The Journal of Physical Chemistry Letters, 2018. **9**(10): p. 2595-2603.

52. Noh, J.H., et al., *Chemical management for colorful, efficient, and stable inorganic-organic hybrid nanostructured solar cells.* Nano Letters, 2013. **13**(4): p. 1764-9.

53. Cheng, X., et al., *Crystal orientation-dependent optoelectronic properties of $MAPbCl_3$ single crystals.* Journal of Materials Chemistry C, 2018. **6**(6): p. 1579-1586.

54. Hoke, E.T., et al., *Reversible photo-induced trap formation in mixed-halide hybrid perovskites for photovoltaics.* Chemical Science, 2015. **6**(1): p. 613-617.

55. Kumawat, N.K., et al., *Band Gap Tuning of $CH_3NH_3Pb(Br_{1-x}Cl_x)_3$ Hybrid Perovskite for Blue Electroluminescence.* ACS Applied Materials & Interfaces, 2015. **7**(24): p. 13119-13124.

56. Sahli, F., et al., *Fully textured monolithic perovskite/silicon tandem solar cells with 25.2% power conversion efficiency.* Nature Materials, 2018. **17**(9): p. 820-826.

57. Chiang, C.-H., Z.-L. Tseng, and C.-G. Wu, *Planar heterojunction perovskite/$PC_{71}BM$ solar cells with enhanced open-circuit voltage via a (2/1)-step spin-coating process.* J. Mater. Chem. A, 2014. **2**(38): p. 15897-15903.

58. Correa Baena, J.P., et al., *Highly efficient planar perovskite solar cells through band alignment engineering.* Energy Environ. Sci., 2015. **8**(10): p. 2928-2934.

59. Luo, H., et al., *Efficient and air-stable planar perovskite solar cells formed on graphene-oxide-modified PEDOT:PSS hole transport layer.* Nano-micro letters, 2017. **9**(4): p. 39.

60. Liu, D., et al., *Efficient planar heterojunction perovskite solar cells with Li-doped compact TiO_2 layer.* Nano Energy, 2017. **31**: p. 462-468.

61. Saliba, M., et al., *Cesium-containing triple cation perovskite solar cells: improved stability, reproducibility and high efficiency.* Energy & Environmental Science, 2016. **9**(6): p. 1989-1997.

62. Etgar, L., et al., *Mesoscopic $CH_3NH_3PbI_3/TiO_2$Heterojunction Solar Cells.* J Am Chem Soc, 2012. **134**(42): p. 17396-17399.

63. Wu, J., et al., *DMF as an additive in a two-step spin-coating method for 20% conversion efficiency in perovskite solar cells.* ACS Applied Materials & Interfaces, 2017. **9**(32): p. 26937-26947.

64. Park, S.-M., et al., *Efficient planar heterojunction perovskite solar cells fabricated via roller-coating.* Solar Energy Materials and Solar Cells, 2016. **155**: p. 14-19.

65. Hu, L., et al., *PEDOT:PSS monolayers to enhance the hole extraction and stability of perovskite solar cells.* Journal of Materials Chemistry A, 2018. **6**(34): p. 16583-16589.

66. Bi, D., et al., *Effect of Different Hole Transport Materials on Recombination in $CH_3NH_3PbI_3$Perovskite-Sensitized Mesoscopic Solar Cells.* The Journal of Physical Chemistry Letters, 2013. **4**(9): p. 1532-1536.

67. Zhou, H., et al., *Interface engineering of highly efficient perovskite solar cells.* Science, 2014. **345**(6196): p. 542-546.

68. Chen, C., et al., *Effect of BCP buffer layer on eliminating charge accumulation for high performance of inverted perovskite solar cells.* RSC Advances, 2017. **7**(57): p. 35819-35826.

69. Lin, Z., et al., *Interface studies of the planar heterojunction perovskite solar cells.* Solar Energy Materials and Solar Cells, 2016. **157**: p. 783-790.

70. Lin, W.K., et al., *Enhancing efficiency of perovskite solar cells using a thin buffer layer.* Vacuum, 2017. **140**: p. 82-88.

71. Wang, R., et al., *A review of perovskites solar cell stability.* Advanced Functional Materials, 2019. **29**(47): p. 1808843.

72. Afreen, M., J. Ali, and M. Bilal, *Challenges of Stability in Perovskite Solar Cells*, in *Fundamentals of Solar Cell Design*. 2021. p. 371-391.

73. Shahbazi, M. and H. Wang, *Progress in research on the stability of organometal perovskite solar cells.* Solar Energy, 2016. **123**: p. 74-87.

74. Song, Z., et al., *Impact of Processing Temperature and Composition on the Formation of Methylammonium Lead Iodide Perovskites.* Chemistry of Materials, 2015. **27**(13): p. 4612-4619.

75. Li, H., et al., *Corrosive Behavior of Silver Electrode in Inverted Perovskite Solar Cells Based on Cu:NiO_x.* IEEE Journal of Photovoltaics, 2019. **9**(4): p. 1081-1085.

76. Han, Y., et al., *Degradation observations of encapsulated planar $CH_3NH_3PbI_3$ perovskite solar cells at high temperatures and humidity.* Journal of Materials Chemistry A, 2015. **3**(15): p. 8139-8147.

77. Turkevych, I., et al., *Photovoltaic Rudorffites: Lead-Free Silver Bismuth Halides Alternative to Hybrid Lead Halide Perovskites.* ChemSusChem, 2017. **10**(19): p. 3754-3759.

78. Giustino, F. and H.J. Snaith, *Toward Lead-Free Perovskite Solar Cells.* ACS Energy Letters, 2016. **1**(6): p. 1233-1240.

79. Park, B.W., et al., *Bismuth based hybrid perovskites $A_3Bi_2I_9$ (A: methylammonium or cesium) for solar cell application.* Advanced Materials, 2015. **27**(43): p. 6806-6813.

80. Jain, S.M., T. Edvinsson, and J.R. Durrant, *Green fabrication of stable lead-free bismuth based perovskite solar cells using a non-toxic solvent.* Communications Chemistry, 2019. **2**(1): p. 91.

81. Frost, J.M., et al., *Atomistic Origins of High-Performance in Hybrid Halide Perovskite Solar Cells.* Nano Letters, 2014. **14**(5): p. 2584-2590.

82. Ito, S., et al., *Effects of Surface Blocking Layer of Sb2S3 on Nanocrystalline TiO2 for $CH_3NH_3PbI_3$ Perovskite Solar Cells.* The Journal of Physical Chemistry C, 2014. **118**(30): p. 16995-17000.

83. Kato, Y., et al., *Silver Iodide Formation in Methyl Ammonium Lead Iodide Perovskite Solar Cells with Silver Top Electrodes.* Advanced Materials Interfaces, 2015. **2**(13): p. 1500195.

84. Shlenskaya, Natalia N., et al., *Light-induced reactivity of gold and hybrid perovskite as a new possible degradation mechanism in perovskite solar cells.* Journal of Materials Chemistry A, 2018. **6**(4): p. 1780-1786.

85. Razza, S., et al., *Research update: large-area deposition, coating, printing, and processing techniques for the upscaling of perovskite solar cell technology.* APL Materials, 2016. **4**(9): p. 091508.

86. Adam, G., et al., *Solution processed perovskite solar cells using highly conductive PEDOT:PSS interfacial layer.* Solar Energy Materials and Solar Cells, 2016. **157**: p. 318-325.

87. Singh, R., et al., *Synthesis of active absorber layer by dip-coating method for perovskite solar cell.* Journal of Molecular Structure, 2018. **1158**: p. 229-233.

88. Matthew R. Leyden, L.K.O., Sonia R. Raga, Yuichi Kato, Shenghao Wang and a.Y. Qi, *High performance perovskite solar cells by hybrid chemical vapor deposition.* Journal of Materials Chemistry A, 2014. **2**: p. 18742–18745.

89. Schmidt, T.M., et al., *Upscaling of perovskite solar cells: fully ambient roll processing of flexible perovskite solar cells with printed back electrodes.* Advanced Energy Materials, 2015. **5**(15): p. 1500569.

90. Ku, Z., et al., *Full printable processed mesoscopic $CH(_3)NH(_3)PbI(_3)/TiO(_2)$ heterojunction solar cells with carbon counter electrode.* Sci Rep, 2013. **3**: p. 3132.

91. Jena, A.K., A. Kulkarni, and T. Miyasaka, *Halide perovskite photovoltaics: background, status, and future prospects.* Chemical reviews, 2019. **119**(5): p. 3036-3103.

92. Galagan, Y., *Perovskite Solar Cells: Toward Industrial-Scale Methods.* The Journal of Physical Chemistry Letters, 2018. **9**(15): p. 4326-4335.

93. Tzounis, L., et al., *Perovskite solar cells from small scale spin coating process towards roll-to-roll printing: Optical and Morphological studies.* Materials Today: Proceedings, 2017. **4**(4, Part B): p. 5082-5089.

94. Shalan, A.E.J.M.A., *Challenges and approaches towards upscaling the assembly of hybrid perovskite solar cells.* Materials Advances, 2020. **1**(3): p. 292-309.

95. Mohamad, D.K., et al., *Spray-Cast Multilayer Organometal Perovskite Solar Cells Fabricated in Air.* Advanced Energy Materials, 2016. **6**(22): p. 1600994.

CHAPTER 2

Experimental details and characterization techniques

In the course of the thesis work, several experimental and characterization techniques have been used for processing and characterizing thin film samples and solar cells. This chapter describes the synthesis of $MAPbI_3$ thin films, device fabrication and characterization techniques used to study the perovskite thin films and solar cells. Extra care was taken to avoid the ambient moisture effect on the $MAPbI_3$ perovskite samples. All the measurements and characterizations were performed immediately after sample preparation by transferring the samples in a vacuum desiccator as required.

2.1 Thin film preparation techniques

Generally, halide perovskite thin films are prepared by various solution process techniques like spin coating [1, 2], dip coating [3], blade coating [4], and spray coating [5]. Other than the solution process, vacuum techniques like chemical vapor deposition [6] and thermal

evaporation techniques [7] are also used. Each of the above mentioned methods has its own merits and demerits, and we shall confine our discussion only to spin coating, dip coating and thermal evaporation, which we have employed for $MAPbI_3$ perovskite film preparation in the present thesis work. Indium tin oxide (ITO) thin films were deposited by the RF sputtering technique and bathocuproine (BCP) thin films were deposited using the thermal evaporation technique. Brief descriptions of these techniques are given in the following sections.

2.1.1 Spin coating

The spin coating technique is a commonly used solution process technique for thin-film fabrication. The two standard methods of solution dispense are static dispense and dynamic dispense. The schematic of steps involved in the spin coating technique are shown in Fig. 2.1 [8]. Most of the reported high-efficiency perovskite solar cells are fabricated using this low-cost spin coating technique. In this technique, a small quantity of coating material (solution) is dispensed onto the center of the flat substrate mounted on the chuck, and then the substrate is spun at a particular speed (typically in the range 1000-8000 rpm). During the spinning of the substrate, centrifugal force spreads the solution radially outward on the substrate, leaving a uniform thin film [8, 9]. The volatile solvents used in the solution mostly evaporate during the spinning process itself. Eventually, the uniformly coated thin film is annealed to dry out the residual solvents and obtain the crystalline nature of the film. Film thickness greatly depends on the viscosity and concentration of the solution [10]. Film thickness obtained by this method lies in the range of nanometer to micrometer, and it is an excellent technique for laboratory scale [8, 11].

The advantages of this technique are

- uniform thin films can be fabricated

- fast fabrication process
- low energy consumption
- the film thickness can be adjusted by simply fine-tuning the spin speed, time, and solution concentration.

However, the spin coating technique is not suitable for coating large-size substrates because, at high rpm the substrate will vibrate more and eventually break. If the solution viscosity is shear-dependent, the lower shear rate experienced near the substrate's center results in higher viscosity and thicker film [9].

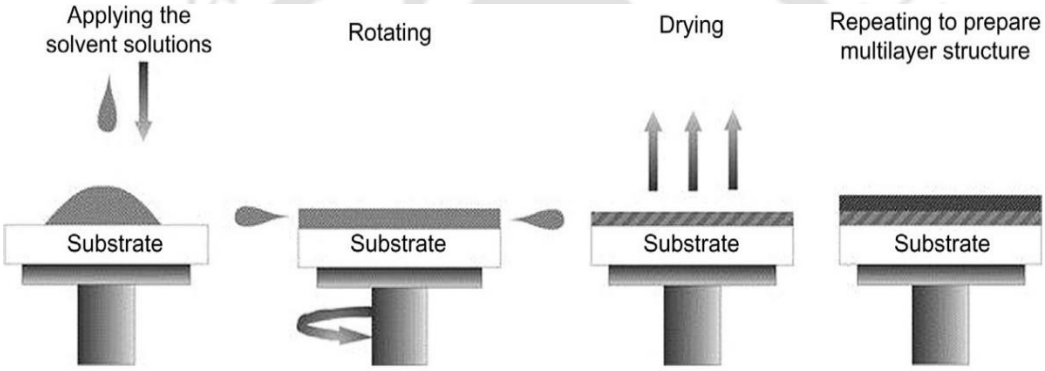

***Figure 2.1**: Process flow of spin coating technique*

2.1.2 Thermal evaporation

The thermal evaporation technique is a widely used Physical Vapor Deposition (PVD) technique for thin film deposition. This technique is simple and generally uses resistively heated filament or boat made of refractory materials such as tungsten (W), molybdenum (Mo) and tantalum (Ta) to evaporate the solid evaporant (to be deposited) in a high vacuum chamber to form a thin film on a chosen substrate [12]. It consists mainly of a vacuum chamber, vacuum pumps, heating filament or boat, substrate holder with or without substrate heater. The film deposition process consists of several steps, such as

(i) sublimation of the evaporant to the vapor phase, (ii) transfer of vapors from the evaporant to the substrate, (iii) condensation of vapors upon arrival on the substrate and (iv) their arrangement or modifications of their binding on the substrate surface.

This method is commonly used for the deposition of metal electrical contacts such as gold, silver, and aluminum for thin-film devices such as solar cells, LED, thin-film transistor (TFT), etc [13, 14]. Besides this, co-evaporation of more than one source/material is also done by carefully controlling the source temperature to maintain the desired stoichiometry of the films [15-17]. The evaporation rate and condensation have wide limits, depending upon the type of source and the materials used. We have used a molybdenum boat as the evaporation source. The characteristics/quality of the films is influenced by the rate of evaporation, deposition pressure, the thickness of the film, angle of evaporation, the temperature of the substrate, and residual gas atmosphere [18]. All these parameters can be controlled in the thermal evaporation technique. Another advantage of this method is that evaporation yields a large area of more or less uniform thickness [12, 19]. The evaporation of material requires heating to a sufficiently high temperature to produce the desired vapor pressure.

The rate of evaporation (Φ_e) is given by Eq. 2.1 [18].

$$\Phi_e = 3.513 \times 10^{22} P_e/(MT)^{1/2} \text{ [molecules cm}^{-2}\text{ s}^{-1}\text{]} \quad (2.1)$$

Where P_e is the equilibrium vapor pressure (in torr) of the evaporant under saturated-vapor conditions at a temperature T, and M is the molecular weight of the vapor species.

2.1.3 Dip coating

Dip coating (DC) is a simple, fast and inexpensive method for thin-film preparation [10]. In this method, the substrate to be coated is cleaned and immersed into the coating material solution for some time and then withdrawn slowly at a constant speed. After that, the coated substrates are dried in the air to remove excess volatile solvents and obtain a thin film [20]. Occasionally, the thin films may be annealed to form a good quality film having the desired properties. This method is used widely due to its simplicity and free of sophisticated equipment. However, non-uniformity in the film is sometimes observed due to the manual steps involved in this method [21]. The film properties largely depend on the parameters, such as immersion time, withdrawal speed, dipping cycles, solution composition, concentration, temperature and environmental conditions.[22]. The main steps involved in the dip-coating process are as follows [23].

1. Immersion: After cleaning, the substrate is slowly dipped into the coating solution. Depending on the type of substrate, a pre-treatment process would be carried out before dipping.

2. Startup: The substrate remains in the solution for some time and is slowly pulled out.

3. Deposition: While the substrate is being pulled out, the thin film starts to deposit on it. The thickness of the coating is directly dependent on the speed of pulling out the substrate. The slower pull will give a thinner coating layer.

4. Drainage: In this step, excess material is drained from the coated substrate.

5. Evaporation: Finally, the solvent starts to evaporate from the surface of the substrate, forming a thin film on it. In the case of volatile solvent, this might happen in step 3 itself.

2.1.4 RF Sputtering

In this thesis, indium-tin-oxide (ITO) layers in the device fabrication were deposited by using RF sputtering. Sputtering is the ejection of atoms from a solid target or source material to be coated on a substrate as a result of energetic gas ions bombardment on the target surface [24]. The RF-sputtering technique is a physical vapor deposition (PVD) technique that uses a high voltage radio frequency (RF) source, often fixed at 13.56 MHz, to create plasma for the deposition process [24, 25]. In the sputtering deposition process, at first base pressure of ~10^{-6}-10^{-7} mbar is created inside the deposition chamber. Once the chamber base pressure is achieved, the inert argon (Ar) gas is introduced into the vacuum chamber at a controlled/required flow rate. A high voltage between the two electrodes, cathode (target) and anode (substrate), leads to the ionization of Ar gas [25]. The ionized Ar^+ gas is then accelerated towards the negatively biased cathode (target), which strikes the target surface and sputter the target atoms. The sputtered atoms from the target move towards the anode and impinge on the substrate to form a thin film. RF Magnetron sputtering uses magnets behind the negative cathode to trap electrons over the negatively charged target material, so they are not free to bombard the anode side (deposited film), allowing for a faster deposition rate. The target area used in the sputtering system was 20.25 cm^2. RF-sputtering offers advantages over DC-sputtering; in particular, sputtering insulating or dielectric target materials like silicon oxide and aluminum oxide becomes possible [24].

2.2 Preparation of $MAPbI_3$ ($CH_3NH_3PbI_3$) perovskite thin films

For thin film deposition and characterization, the perovskite films were deposited on Corning 1737 glass substrates. Prior to that, the substrates were sequentially cleaned with soap solution, deionized water, acetone, and isopropanol in an ultrasonic bath for 15

minutes each, followed by drying in the fast flow of dry nitrogen gas. After that, the substrates were dried on a hot plate at 110 °C for 10 minutes, followed by UV-Ozone treatment for 15 minutes. The perovskite film deposition methods used in this thesis are briefly described in the following sections.

2.2.1 Using one-step method

The one-step deposition of $MAPbI_3$ perovskite thin films is done with the spin coating technique by following the procedure reported elsewhere [26]. For preparing $MAPbI_3$ solution, 461 mg of PbI_2 and 159 mg of MAI were added to 635 µl DMF and 70 µl DMSO (dimethyl sulfoxide) together and then let to stir in a vial till a clear yellow solution was obtained. The $MAPbI_3$ solution was spin-coated at 4000 rpm for 60 sec on cleaned substrates in a nitrogen-filled chamber having *RH* (relative humidity) ~ 22% (measured by a commercially available hygrometer). During the spin coating process, chlorobenzene (an anti-solvent) was dripped over the spinning substrate. After that, the films were annealed at 100 °C for 10 minutes [in the same nitrogen-filled chamber], and finally, $MAPbI_3$ perovskite thin films (thickness ~500 nm) having dark shiny surfaces were obtained.

2.2.2 Using two-step methods

For the deposition of $MAPbI_3$ perovskite thin films using the two-step methods, lead iodide (PbI_2) thin films are deposited in the first step and then in the second step, PbI_2 films were dip-coated in methylammonium iodide (CH_3NH_3I, MAI) solution to get $MAPbI_3$ perovskite films. Thermal evaporation and dip coating (TE+DC) and spin coating and dip coating (SC+DC) are the two different two step methods used for deposition of $MAPbI_3$ perovskite thin films.

2.2.2.1 Thermal evaporation and dip coating (TE+DC)

In the TE+DC method for $MAPbI_3$ thin films deposition, PbI_2 powder (~50 mg) (99.99% pure, Alfa Aesar) was thermally evaporated using a thermal Evaporator system (Hind High Vacuum, Model-12A4D) at the substrate temperature of 100 °C and process pressure ~ 2×10^{-5} mbar to get PbI_2 thin films (thickness ~200±10 nm). A molybdenum boat source was used to evaporate the PbI_2 powder at a secondary LT (low tension) supply of 33 A. In the second step, the PbI_2 films were dipped in the MAI solution (99% pure, Sigma-Aldrich), having a concentration of 10 $mgml^{-1}$ in 2-propanol (anhydrous, 99.5% pure, Sigma-Aldrich). Soon after a few minutes of dipping, the films were annealed at 100 °C for 10 minutes to obtain dark perovskite films eventually (~thickness 395±10 nm). The dip-coating step was performed in an ambient atmosphere (*RH*~ 40% and temperature ~28 °C) and/or inside the dry nitrogen-filled glove box.

2.2.2.2 Spin coating and dip coating (SC+DC)

In the SC+DC method for $MAPbI_3$ thin film deposition, PbI_2 is first spin-coated, followed by dip-coating in MAI in a dry nitrogen-filled glove box (pressure ~1010 mbar and temperature ~28 °C). For coating PbI_2 film, one molar PbI_2 solution was prepared using dimethylformamide (DMF) solvent by stirring at 70 °C for 12 hours. The PbI_2 solution was spun on cleaned corning glass substrates at 3000 rpm for 30 seconds and then transferred to a hot plate and dried at 70 °C for 30 minutes. In the next step, the spin-coated PbI_2 films (thickness 190±18 nm) were dipped in MAI solution to form $MAPbI_3$ and annealed at 100 °C for 10 minutes to get perovskite layers of thickness 390±21 nm, similar to that for the thermally evaporated PbI_2 films.

2.3 Fabrication of solar cells

The planar heterojunction (p-i-n) perovskite solar cells are fabricated using one-step and the two-step (TE+DC) methods. The fabrication steps are briefly described below.

2.3.1 Using one-step method

The fabrication is started after cleaning the transparent conducting oxide (TCO) coated glass substrates in a similar procedure as mentioned in section 2.2. After proper masking on the substrate for the back electrode on the cleaned substrates, PEDOT:PSS (Poly(2,3-dihydrothieno-1,4-dioxin)-poly(styrene sulfonate)) [Clevios AI 4083], was spin-coated at 4000 rpm. The PEDOT:PSS layer (HTL) was then annealed at 120 ºC for 15 minutes and allowed to cool down. The thickness of PEDOT:PSS was found to be ~50 nm. After that, the samples were transferred to a glove box where $MAPbI_3$ was spin-coated using the one-step method as described in section 2.2.1. In the next step, the ETL layer PCBM ((6, 6)-phenyl C61-butyric acid methyl ester) 20 $mgml^{-1}$ in chlorobenzene was spin-coated at 2000 rpm for 30 seconds on top of the perovskite absorber layer, which yields a thickness of 30-40 nm. The samples were then transferred into the thermal evaporator chamber for the bathocuproine (BCP). The BCP layer of thickness ~15 nm was deposited by thermal evaporation at room temperature. Finally, the silver electrode (80-100 nm thickness) was deposited in a thermal evaporator chamber at a process pressure of ~3×10^{-6} mbar to complete the device structure.

2.3.2 Using two-step method (TE+DC)

The two-step fabrication steps are similar to one-step method till the deposition of PEDOT:PSS. Then the $MAPbI_3$ perovskite absorber layer was deposited using the two-step deposition (TE+DC) method as described in section 2.2.2.1. In the next step, the ETL layer PCBM ((6, 6)-phenyl C61-butyric acid methyl ester) 20 $mgml^{-1}$ in

chlorobenzene was spin-coated at 2000 rpm for 30 seconds on top of the perovskite absorber layer, which yields a thickness of 30-40 nm. The samples were then transferred into the thermal evaporator chamber for the Ag electrode deposition. Finally, the Ag electrode (thickness ~100 nm) was deposited at room temperature and process pressure of ~3×10^{-6} mbar to complete the device structure. For devices having the ITO layer in the stack, we have deposited the ITO layer as an interfacial layer between the PCBM and Ag layers to prevent the diffusion of the top silver electrode layer. The ITO thin film (thickness ~40-50 nm) was deposited on top of the PCBM layer using the RF-sputtering technique by following our previous work [27]. The deposition parameters used for ITO film were: Argon flow rate of 7 SCCM (standard cubic centimetre per minute), RF power of 60 W (power density~2.96 Wcm^{-2}), process pressure (PP) of 0.05 mbar, and substrate temperature of 50 °C.

2.4 Characterization techniques

The various techniques used for characterizing $MAPbI_3$ perovskite thin films and solar cells are described below.

2.4.1 X-ray diffraction (XRD)

X-ray diffraction or XRD is a non-destructive characterization technique used to study microstructural properties of a material based on X-ray diffraction to find out the nature of the material as amorphous or crystalline. This technique is used for the analysis of the material composition, crystalline structure, crystal orientations, phase, average crystallite size, lattice strain, and crystal defects [28].

In the present thesis, XRD is performed using Rigaku, TTRAX III or Rigaku, Smart Lab equipped with CuK_α radiation of 1.54 Å, for the structural study of $MAPbI_3$ thin films deposited on corning 1737 glass substrates. The measurements are performed in thin-film

mode at a grazing angle of incidence 1° with a scan rate of 3° per minute in 2θ range ~ 10-60°. The mean crystallite size (d) are calculated using Scherrer's formula given as in Eq. 2.2.

$$d = \frac{0.9\lambda}{B\cos\theta} \tag{2.2}$$

Where λ is the wavelength of x-ray, B is the broadening or Full Width at Half Maximum (FWHM) of the peak and θ is Bragg's angle.

2.4.2 UV-Vis-NIR spectroscopy

Ultraviolet-Visible-Near Infrared (UV-Vis-NIR) spectrometry is a useful characterization technique for measuring the absorbance, transmittance, or reflectance of thin films. The measurements are performed using Perkin-Elmer Lambda 950 spectrometer corning on the films deposited on 1737 glass substrates in various wavelength ranges. The absorbance and transmittance are measured with reference to air. The optical bandgap (E_g) is calculated using the Tauc relation given in Eq. 2.3 [29].

$$\alpha h\upsilon = B\left(h\nu - E_g\right)^n \tag{2.3}$$

Where α is the absorption coefficient (cm^{-1}), $h\nu$ is the incident photon energy (eV), B is proportionality constant. The values of the exponent n are ½ and 2 for direct and indirect bandgap material, respectively. Using Eq.2.3, the bandgap values of thin films are calculated from the $(\alpha h\nu)^{1/n}$ vs. $h\nu$ plot.

2.4.3 Atomic force microscopy (AFM)

AFM is a powerful tool to study the surface topography of thin films. AFM generates an image by scanning a small cantilever with a sharp tip on the sample surface. As the tip

moves in response to the interaction force with the film surface, the cantilever deflects. The deflection of the cantilever is detected by a focused laser beam reflected from the top surface of the cantilever to the photodiode. Thus the tip movement is traced with the reflected laser beam and then the surface image is generated [30, 31]. Two basic modes of operating AFM are contact and tapping mode. In contact mode, the tip is in contact with the film surface. On the other hand, in the tapping mode, the AFM cantilever is vibrated above the sample surface such that the tip is only in intermittent contact with the surface. The tapping mode is commonly used for AFM imaging as it helps to reduce the shear forces associated with the tip movement.

In this thesis, the AFM measurement were performed using Cypher, Oxford instrument in tapping mode. The measurement results are analyzed using WSxM software for the root mean square(RMS) roughness estimation for a selected area of 5 μm × 5 μm.

2.4.4 Field emission scanning electron microscopy (FESEM)

In FESEM, a high-energy narrow electrons beam is used to obtain images from the sample surface. FESEM uses a field emission gun as the electron source. After the electron beam exits the electron gun, they are confined and focused on a small spot using metal apertures and magnetic lenses. Finally, detectors in the microscope collect electron signals emitted from the specimen to produce an image [32].

The confined small spot size of the electron probe makes FESEM a high-resolution instrument. FESEM produces a cleaner image, less electrostatic distortions and spatial resolution <2 nm, which is 3 to 6 times better than a scanning electron microscope (SEM). The surface morphology of the thin films is obtained by field emission scanning electron microscopy (FESEM, ZEISS, SIGMA 300). FESEM was operated with an accelerating

voltage of 2 to 4 KeV and the films were coated with a very thin gold layer by sputtering to avoid the surface charging effect during measurement.

2.4.5 Photoluminescence (PL) spectroscopy

PL spectroscopy is a contactless, non-destructive technique to probe the electronic structure of materials. In PL spectroscopy, the incident light (excitation) is absorbed by the material and then photoexcitation occurs, followed by the relaxation process accompanied by the photon emission. A charge coupled device (CCD) camera collects the spectrum for each examined point while scanning over the sample. The intensity and spectral content of the emitted photoluminescence directly measure various important material properties, including bandgap, impurity levels, defects, and recombination mechanisms [33, 34]. When a semiconductor material is excited with a light source with photon energy larger than the bandgap energy of the semiconductor, the excited electron and hole will not remain in their excited states for very long; instead, they will relax very rapidly (10^{-13} s) to the lowest energy states within their respective bands by emitting phonons. When the electron (hole) finally arrives at the bottom (top) of the conduction (valence) band, the electron-hole pair recombines radiatively with the emission of a photon (luminescence), or non-radiatively by transferring the electron's energy to impurities or defects in the material or dangling bonds at the surface. The energy of the emitted photon directly measures the energy difference between the involved bands. Thus, the direct bandgap of semiconductors or the HOMO-LUMO gap in the molecules can be determined. In semiconductors, it is also expected that the point defects yield states in the bandgap, so the PL signal is observed at photon energies below the bandgap showing the characteristics of different defects [35, 36]. In the present thesis, steady-state PL measurements on thin film samples are carried out using Horiba Jobin- Yvon, Flouromax-4 at room temperature.

2.4.6 Current-Voltage (*I-V*) measurements of perovskite thin films

Current-Voltage measurements of perovskite thin-film are performed using the two-probe method in co-planar geometry by keeping the thin-film in a closed chamber. The Keithley 2450 source measurement unit (SMU) was used for *I-V* measurements. For *I-V* measurements, silver (Ag) electrodes were deposited on the thin films by thermal evaporation of high purity (99.999%) Ag wire. The length and separation of electrodes are 10 mm and 1 mm, respectively, in co-planar geometry. A 100 W halogen lamp with incident power density of 1000 Wcm^{-2} was used for photocurrent measurements. In the co-planar geometry, the conductivity (σ) of the film is given by Eq.2.4. This equation is suitable for our case as the perovskite film are of few hundred nanometres and current flow across the film while applying field between the two electrodes.

$$\sigma = \frac{I \times d}{V \times l \times t} \tag{2.4}$$

Where l is the length of electrodes, d is the separation between the electrodes, V is the applied voltage, I is the measured current, and t is the film thickness.

The activation energy (E_a) is estimated from temperature-dependent dark conductivity data using the Arrhenius plot [37]. The relation between the dark conductivity (σ_d) and activation energy (E_a) is given by Eq.2.5.

$$\sigma_d = \sigma_0 \, exp\left(-\frac{E_a}{K_B T}\right) \tag{2.5}$$

Where σ_d is the dark conductivity, σ_0 is the pre-factor, k is the Boltzmann constant, T is the absolute temperature in Kelvin.

2.4.7 Current-time (*I-t*) measurements of perovskite thin films

The *I-t* measurements of $MAPbI_3$ thin films are done under vacuum (~0.05 mbar) to avoid surface-related processes induced by chemisorption and desorption of oxygen. Here the

transient current as a function of time at different light intensities and temperatures (25 °C-70 °C) are recorded. The neutral density (ND) filters (Make: Melles Griot) are used to vary the light intensity to 10%, 30%, 50%, and 80% of full intensity (1000 Wm^{-2}). During measurements, the light intensity and temperature were increased from low to high. Time step 0.1s (100 ms) was used to record the *I-t* data.

Aluminum (Al) electrodes of 10 mm length and 1mm separation were made by thermal evaporation of high purity (99.999%) Al wire on the perovskite thin films for *I-t* measurements. The samples were mounted on a stainless-steel sample holder in a vacuum chamber, which has a heater within it. The temperature of the film sample was measured with the help of a platinum resistance thermometer (PT-100) on a digital multimeter (Agilent, model: 34401A).

2.4.8 Current-Voltage (*I-V*) measurements of solar cells

The performance of a solar cell can be determined from the current-voltage (*I-V*) measurement. The *I-V* characteristic measurements of fabricated $MAPbI_3$ perovskite based heterojunction solar cells were done under 100 $mWcm^{-2}$ of incident power density from a Xenon lamp with AM1.5 conditions. The Keithley 2450 source measurement unit has been used to apply voltage sweep and measure the current from solar cells. Fig. 2.2 shows the schematic diagram of current density-voltage (*J-V*) characteristics of a solar cell.

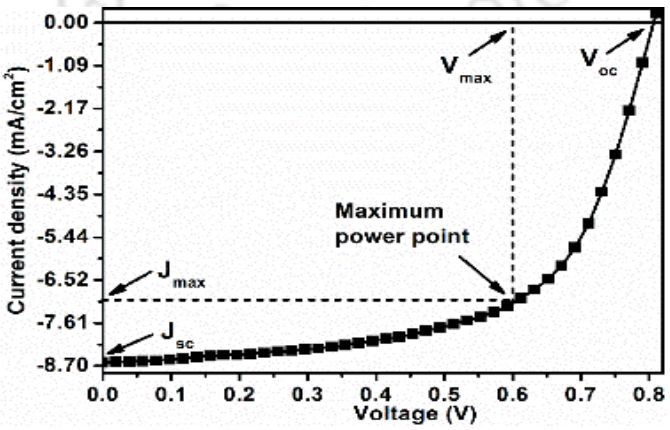

Figure 2.2: *Current density-voltage (J-V) characteristics of solar cell*

From the *J-V* characteristics of the solar cell, short-circuit current density (J_{sc}), open-circuit voltage (V_{oc}), and fill factor (*FF*) can be determined. J_{sc} is short-circuit current density at which voltage across the solar cell is zero. The V_{oc} is the maximum voltage output of a solar cell, at which no current flows through the external circuit; that is, at zero current $J_{sc} = 0$. The *FF* is the ratio of the maximum power that can be obtained from the cell to the product of J_{sc} and V_{oc}. Graphically FF is a measure of the squareness of the *I-V* curve. The solar cell efficiency (η) is the fundamental parameter for comparing one solar cell's performance to another working cell. The solar cell efficiency (η) is defined as the ratio of maximum electrical energy output from the solar cell to the input solar energy on the cell. The performance of a solar cell is described by a power conversion efficiency (η).

The $\eta(\%)$ is determined by the following equations Eq.2.6 and Eq.2.7.

$$\eta(\%) = \frac{J_{sc} \times V_{oc} \times FF}{P_{in}} \times 100 \tag{2.6}$$

$$FF = \frac{J_{max} \times V_{max}}{J_{sc} \times V_{oc}} \tag{2.7}$$

Where J_{sc}, V_{oc}, *FF* and P_{in} are short-circuit current density, open-circuit voltage, fill factor and input power.

2.5 Simulation details of $MAPbI_3$ based perovskite solar cells (n-i-p and p-i-n) using Sentaurus-TCAD software

The simulation studies were carried out for n-i-p and p-i-n planar structure $MAPbI_3$ solar cells using Sentaurus-TCAD simulation software under the AM 1.5 solar spectrum condition at room temperature (300 K). This simulation tool simulates the electrical behaviour in a semiconductor device that is represented as a mesh grid file [38]. All the electrical simulations are performed using the drift-diffusion transport model, in which the electrostatic Poisson equation and carrier continuity equation for electron and hole are solved iteratively [39]. The n-i-p and p-i-n device structures used for simulations are

FTO/SnO_2/$MAPbI_3$/Spiro-OMeTAD/Ag(n-i-p) and *FTO/PEDOT:PSS/$MAPbI_3$/PCBM/Ag (p-i-n).* In the n-i-p configuration, FTO is used as the front contact, SnO_2 as ETL, $MAPbI_3$ is the absorber layer, spiro-OMeTAD is HTL, and Ag is the metal back contact. In the p-i-n device structure, PEDOT:PSS (Poly(2,3-dihydrothieno-1,4-dioxin)-poly(styrene sulfonate) and PCBM ([6,6]-phenyl-C_{61}-butyric acid methyl ester) act as HTL and ETL, respectively and the other layers are the same as given for the n-i-p configuration. In the n-i-p structure, the light was shone through SnO_2 (ETL) and in the p-i-n structure, the light was shone through PEDOT:PSS (ETL). Through this simulation, we studied the influence of varying some key parameters of the absorber ($MAPbI_3$) layer, such as (i) bulk defect density variation (1×10^{14} to 1×10^{19} cm^{-3}), (ii) interface defect density variation (1×10^{6} to 1×10^{12} cm^{-2}), at ETL/$MAPbI_3$ and $MAPbI_3$/HTL interfaces and (iii) thickness variation of the perovskite absorber layer (200 to 1000 nm), on the performance of the solar cell.

2.6 References

1. Nie, W., et al., *High-efficiency solution-processed perovskite solar cells with millimeter-scale grains.* Science, 2015. **347**(6221): p. 522.
2. You, J., et al., *Low-temperature solution-processed perovskite solar cells with high efficiency and flexibility.* ACS nano, 2014. **8**(2): p. 1674-1680.
3. Singh, R., et al., *Synthesis of active absorber layer by dip-coating method for perovskite solar cell.* Journal of Molecular Structure, 2018. **1158**: p. 229-233.
4. Back, H., et al., *Interfacial modification of hole transport layers for efficient large-area perovskite solar cells achieved via blade-coating.* Solar Energy Materials and Solar Cells, 2016. **144**: p. 309-315.
5. Bishop, J.E., et al., *Fully Spray-Coated Triple-Cation Perovskite Solar Cells.* Scientific Reports, 2020. **10**(1): p. 6610.
6. Matthew R. Leyden, L.K.O., Sonia R. Raga, Yuichi Kato, Shenghao Wang and a.Y. Qi, *High performance perovskite solar cells by hybrid chemical vapor deposition.* Journal of Materials Chemistry A, 2014. **2**: p. 18742–18745.
7. Liu, M., M.B. Johnston, and H.J. Snaith, *Efficient planar heterojunction perovskite solar cells by vapour deposition.* Nature, 2013. **501**(7467): p. 395-8.

8. Mishra, A., N. Bhatt, and A. Bajpai, *Nanostructured superhydrophobic coatings for solar panel applications*, in *Nanomaterials-Based Coatings*. 2019, Elsevier. p. 397-424.

9. Kumar, S., et al., *14 - Metal oxides for energy applications*, in *Colloidal Metal Oxide Nanoparticles*, S. Thomas, A. Tresa Sunny, and P. Velayudhan, Editors. 2020, Elsevier. p. 471-504.

10. Scriven, L., *Physics and applications of dip coating and spin coating.* MRS Online Proceedings Library Archive, 1988. **121**.

11. Birnie, D.P., *Spin Coating Technique*, in *Sol-Gel Technologies for Glass Producers and Users*, M.A. Aegerter and M. Mennig, Editors. 2004, Springer US: Boston, MA. p. 49-55.

12. Chopra, K.L., *Thin film phenomena*. 1979: Krieger Publishing Company.

13. Etgar, L., et al., *Mesoscopic $CH_3NH_3PbI_3/TiO_2$Heterojunction Solar Cells.* J Am Chem Soc, 2012. **134**(42): p. 17396-17399.

14. Correa Baena, J.P., et al., *Highly efficient planar perovskite solar cells through band alignment engineering.* Energy Environ. Sci., 2015. **8**(10): p. 2928-2934.

15. Gao, C., et al., *Formation of organic–inorganic mixed halide perovskite films by thermal evaporation of $PbCl_2$ and CH_3NH_3I compounds.* RSC Adv., 2015. **5**(33): p. 26175-26180.

16. Li, J., et al., *Highly Efficient Thermally Co-evaporated Perovskite Solar Cells and Mini-modules.* Joule, 2020. **4**(5): p. 1035-1053.

17. Liu, M., M.B. Johnston, and H.J.J.N. Snaith, *Efficient planar heterojunction perovskite solar cells by vapour deposition.* Nature, 2013. **501**(7467): p. 395-398.

18. Ohring, M., *Chapter 3 - Thin-Film Evaporation Processes*, in *Materials Science of Thin Films (Second Edition)*, M. Ohring, Editor. 2002, Academic Press: San Diego. p. 95-144.

19. Goswami, A., *Thin film fundamentals*. 1996: New age international.

20. Basumatary, P. and P. Agarwal, *Two-step fabrication of $MAPbI_3$ perovskite thin films with improved stability.* Bulletin of Materials Science, 2019. **42**(6): p. 268.

21. Neacşu, I.A., et al., *Chapter 9 - Inorganic micro- and nanostructured implants for tissue engineering*, in *Nanobiomaterials in Hard Tissue Engineering*, A.M. Grumezescu, Editor. 2016, William Andrew Publishing. p. 271-295.

22. Lončarević, D. and Ž. Čupić, *Chapter 4 - The perspective of using nanocatalysts in the environmental requirements and energy needs of industry*, in *Industrial Applications of Nanomaterials*, S. Thomas, Y. Grohens, and Y.B. Pottathara, Editors. 2019, Elsevier. p. 91-122.

23. Kakaei, K., M.D. Esrafili, and A. Ehsani, *Chapter 8 - Graphene and Anticorrosive Properties*, in *Interface Science and Technology*, K. Kakaei, M.D. Esrafili, and A. Ehsani, Editors. 2019, Elsevier. p. 303-337.

24. Ohring, M., *Chapter 4 - Discharges, Plasmas, and Ion–Surface Interactions*, in *Materials Science of Thin Films (Second Edition)*, M. Ohring, Editor. 2002, Academic Press: San Diego. p. 145-202.

25. Mattox, D.M., *Chapter 5 - The Low Pressure Plasma Processing Environment*, in *Handbook of Physical Vapor Deposition (PVD) Processing (Second Edition)*, D.M. Mattox, Editor. 2010, William Andrew Publishing: Boston. p. 157-193.

26. Liu, X., C. Xu, and E.-C. Lee, *Chlorobenzene-Mediated Control of Crystallization in Perovskite Films for High-Performance Solar Cells.* ACS Applied Energy Materials, 2020. **3**(12): p. 12291-12297.

27. Kanneboina, V., P. Basumatary, and P. Agarwal, *Influence of deposition temperature on indium tin oxide thin films for solar cell applications.* AIP Conference Proceedings, 2019. **2091**(1): p. 020016.

28. Kohli, R. and K.L. Mittal, *Developments in Surface Contamination and Cleaning*, in *Developments in Surface Contamination and Cleaning, Volume 12*, R. Kohli and K.L. Mittal, Editors. 2019, Elsevier. p. 23-105.

29. Eom, K., et al., *Depth-resolved band alignments of perovskite solar cells with significant interfacial effects.* Journal of Materials Chemistry A, 2017. **5**(6): p. 2563-2571.

30. Eaton, P. and P. West, *Atomic force microscopy*. 2010: Oxford university press.

31. Giessibl, F.J.J.R.o.m.p., *Advances in atomic force microscopy*. 2003. **75**(3): p. 949.

32. Leng, Y., *Materials characterization: introduction to microscopic and spectroscopic methods*. 2009: John Wiley & Sons.

33. Adams, F. and C. Barbante, *Chapter 9 - Spectroscopic Imaging*, in *Comprehensive Analytical Chemistry*, F. Adams and C. Barbante, Editors. 2015, Elsevier. p. 339-384.

34. Kiligaridis, A., et al., *Excitation wavelength dependence of photoluminescence flickering in degraded $MAPbI_3$ perovskite and its connection to lead iodide formation.* Journal of Luminescence, 2020. **222**: p. 117129.

35. Fox, M. *Optical Properties of Solids*. 2002.

36. Fang, H.H., et al., *Photophysics of organic–inorganic hybrid lead iodide perovskite single crystals.* Advanced Functional Materials, 2015. **25**(16): p. 2378-2385.

37. Street, R.A., *Hydrogenated Amorphous Silicon*. Cambridge Solid State Science Series. 1991, Cambridge: Cambridge University Press.

38. Rahman, T. and K.J.C.P.C. Fobelets, *Efficient tool flow for 3D photovoltaic modelling.* Computer Physics Communications, 2015. **193**: p. 124-130.

39. Kumar, R.R., S.K.J.S. Pandey, and Microstructures, *Performance evaluation and material parameter perspective of eco-friendly highly efficient $CsSnGeI_3$ perovskite solar cell.* Superlattices and Microstructures, 2019. **135**: p. 106273.

CHAPTER 3

Synthesis and study of $MAPbI_3$ perovskite thin films deposited using one-step method

This chapter presents the fabrication of $MAPbI_3$ perovskite thin films (on corning 1737 glass substrates) using a one-step solution method and study of optoelectronic properties. Among the different halide perovskite, $MAPbI_3$ ($CH_3NH_3PbI_3$) has been broadly studied, focusing on thin films for application in photovoltaics as a light absorber layer [1, 2]. $MAPbI_3$ has an optical bandgap of ~1.6 eV and numerous excellent optoelectronic properties, which are ideal for solar cells [3-5]. Thus, $MAPbI_3$ perovskite has shown good cell performance with high efficiency [6, 7]. Besides solar cells, hybrid perovskite has also been studied and found suitable for other optoelectronic devices like light-emitting diodes (LEDs), photodetectors, and lasers [5, 8-11]. Thus, hybrid perovskite materials have the potential for broad applications in next-generation optoelectronic devices. However, it is also necessary to investigate the nature of defects and defect levels

present in the material. For photovoltaic applications, understanding the nature of defects in the absorber layer is essential to minimize non-radiative decay pathways by improving the material properties to achieve a high internal quantum efficiency and a high open-circuit voltage (V_{oc}) [12].

With this motivation, the structural and optoelectronic properties of the synthesized perovskite thin films are studied. The room temperature PL spectroscopy technique is suitable for evaluating semiconductor material properties such as optical band gap, discrete electronic states and defects [13-15]. A detailed study of luminescence features of $MAPbI_3$ perovskite thin films was carried out at room temperature using photoluminescence (PL) and photoluminescence excitation (PLE) spectroscopy at varying excitation wavelength (λ_{ex}) (500 nm to 600 nm) and emission wavelength (λ_{em}) (700 nm to 850 nm) respectively.

3.1 Experimental details

The $MAPbI_3$ perovskite thin films were deposited on Corning 1737 glass substrates by the one-step deposition process using the spin coating technique as mentioned in chapter 2, section 2.2.1 [16]. The X-ray diffraction (XRD) was performed on perovskite thin films deposited on the corning glass substrate at room temperature. Field Emission Scanning Electron Microscope (FESEM) was used to study the surface morphology of perovskite thin films. Optical absorption, transmission, and reflectance spectra were measured using a UV-Vis-NIR spectrometer. PL and PLE spectra were recorded using Horiba Jobin-Yvon, FluoroMax-4 spectrometer at the same sample position. The PL spectra were recorded at fixed excitation energy by scanning the emission energy, whereas the PLE spectra were recorded at fixed emission energy by scanning the excitation energy. The current vs. time (*I-t*) measurements were done in co-planar geometry using aluminum (Al) electrodes of 10 mm length at 1 mm separation on the perovskite film using Keithley 2450 source

measurement unit (SMU) at an applied field of 100 Vcm^{-1}. The measurements were done in vacuum (pressure ~0.05 mbar) to avoid the moisture effect on perovskite film.

3.2 Results and discussion

3.2.1 X-ray diffraction analysis

The XRD analysis confirmed the formation of the $MAPbI_3$ perovskite film on the Corning 1737 glass substrate. XRD pattern of the synthesized $MAPbI_3$ thin film is shown in Fig. 3.1. The XRD graph within the range of 2θ values from 10° to 60° shows the prominent peaks at 14.07°, 28.43°, 31.84°, 40.55°, and 43.10°, corresponding to (110), (220), (222), (224) and (314) planes of the pure tetragonal (β) phase of $MAPbI_3$ perovskite respectively [1, 17, 18]. In addition, small peaks from other planes of $MAPbI_3$ tetragonal structure are also observed in Fig. 3.1 [19]. The XRD pattern confirms that the deposited perovskite films are highly crystalline and pure with no excess or residual PbI_2 reagent [20].

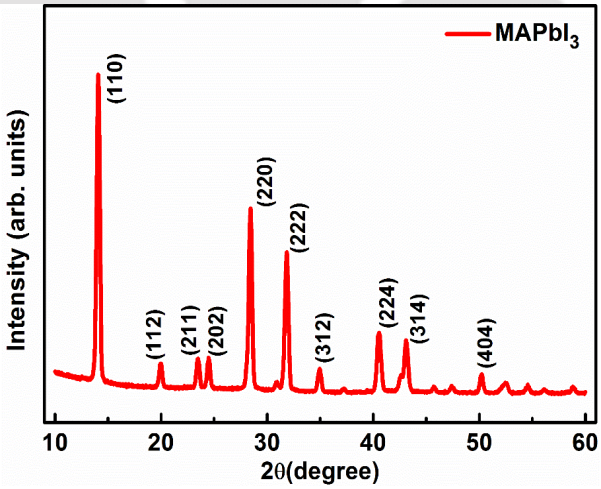

Figure 3.1: *XRD pattern of $MAPbI_3$ perovskite thin film using CuK_α radiation. Peaks correspond to the pure tetragonal (β) phase of $MAPbI_3$ perovskite*

3.2.2 FESEM analysis

The FESEM image in Fig. 3.2 shows the surface morphology of the deposited $MAPbI_3$ film. The films obtained are uniform and pinhole-free with homogeneous morphology and a maximum grain size of ~500 nm.

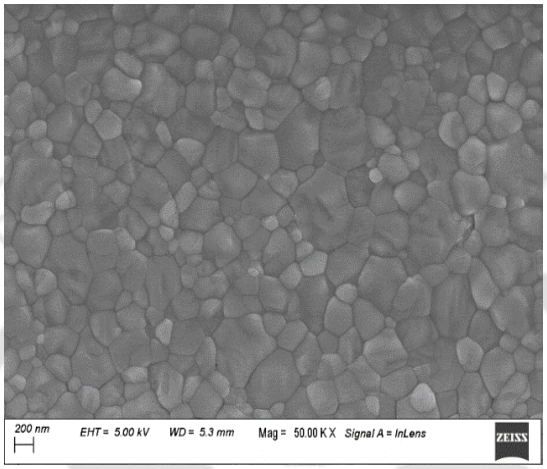

Figure 3.2: *FESEM (top view) image showing the surface morphology of $MAPbI_3$ thin film*

3.2.3 UV-Vis analysis

Fig. 3.3(a) shows the UV-Vis (ultraviolet-visible) absorbance (*A*) spectra of $MAPbI_3$ perovskite thin films. The perovskite thin films have absorption onset at ~783 nm (pointed with arrow mark), with a sharp increase in absorbance up to 750 nm. The strong absorption characteristic of $MAPbI_3$ perovskite is evident for the entire visible range [17, 21]. As seen in Fig. 3.3(b), the transmittance (*T*) and diffuse reflectance (*R*) spectra of $MAPbI_3$ thin film decrease abruptly below 800 nm, consistent with the absorption characteristic. The low values of *T* (< 5%) and *R* (< 20%) in the visible region below ~783 nm is due to the perovskite's high absorption coefficient at the photon energies above its bandgap energy. However, the transmittance and reflectance are high in the near-infrared (NIR) region.

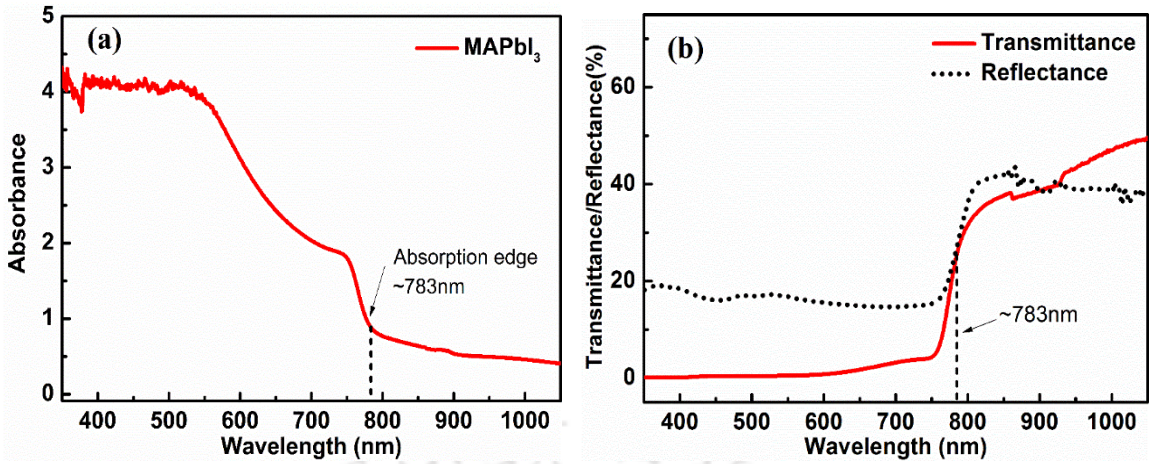

Figure 3.3: *(a) Absorbance and (b) Transmittance and diffuse reflectance spectra of $MAPbI_3$ thin film*

The absorption coefficient (α) is calculated using Eq.3.1.

$$\alpha = \frac{2.303A}{t} \tag{3.1}$$

Where A is the absorbance and t is the film thickness.

The measured UV-Vis absorbance spectra do not account for the reflectance losses from the surface of thin films, and thus the absorbance is usually overestimated. Therefore, for absorption coefficient (α) calculation, the measured diffuse reflectance value (R) (Fig. 3.3(b)) is subtracted from the measured A value [actual absorbance $A^* = (A\text{-}R)$]. The calculated α values of the perovskite films using A^* in Eq. 3.1 are of the order 5×10^4-1×10^5 cm^{-1}, which is similar to the reported values in the literature and comparable to that of the other inorganic semiconductors [22]. Since the absorption coefficient of $MAPbI_3$ perovskite films is high, a thin layer of thickness ~300-400 nm is sufficient as an absorber layer for solar cells [18]. The optical bandgap (E_g) is calculated using the Tauc plot $(\alpha hv)^{1/n}$ vs. hv; where α is the absorption coefficient (cm^{-1}), hv is the photon energy (eV), and n = 1/2 for direct bandgap material [23]. The calculated bandgap is 1.58 ± 0.01 eV, which is close to the reported values [3].

3.2.4 PL and PLE analysis

Fig. 3.4 shows the PL spectra of $MAPbI_3$ thin film recorded at room temperature (~300 K) for a selected range of λ_{ex} from 500 - 600 nm at an interval of 10 nm. A high-intensity PL peak at ~783 nm (1.58 eV) is observed for all values of λ_{ex} (500 - 600 nm) . The peak position is consistent with the bandgap value (~1.58 eV) estimated from the UV-Vis absorbance data and very close to the reported bandgap value of ~1.60 eV of the $MAPbI_3$ tetragonal phase at room temperature (~300 K) [3]. The tetragonal phase of $MAPbI_3$ could also be identified from the XRD analysis as well (Fig. 3.1). This broad PL peak at ~783 nm arises due to the radiative recombination of electrons and holes near the band edge and it depicts the direct bandgap nature of $MAPbI_3$ perovskite [24]. There is no shift in the peak positions with the change in λ_{ex}, though a decrease in the peak intensity is observed towards the longer λ_{ex} due to a decrease in absorbance (Fig. 3.3(a)). The intensity of the emission peak gives a quantitative idea of the radiative recombination of free carriers generated for a particular λ_{ex}. The small peak observed at ~823 nm is identified as an instrumental noise and is believed not to affect the PL spectra.

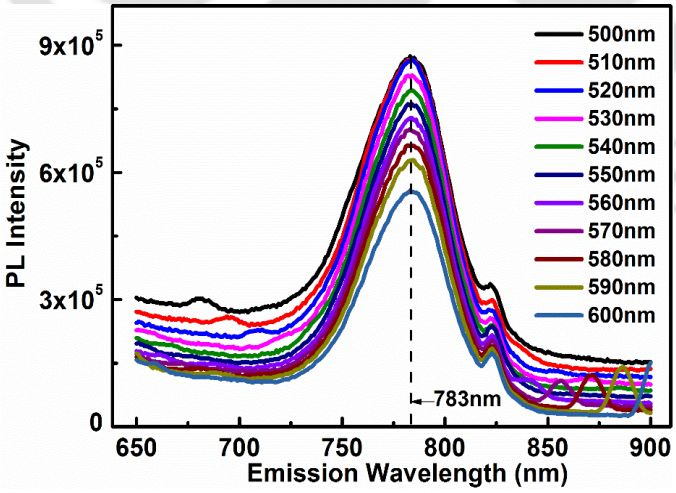

Figure 3.4: *PL spectra of $MAPbI_3$ thin film at different excitation wavelengths (500-600 nm)*

The PL spectra are normalized by the incident photo flux corresponding to the λ_{ex} after considering the reflection losses for quantitative analysis. The peak intensities of normalized PL spectra in Fig. 3.5(a) indicate the fraction of absorbed photons in the top thin layer responsible for the PL signal. A lower normalized intensity for high λ_{ex} is due to the lower absorption coefficient for these photons. From the normalized PL spectra shown in Fig. 3.5(a), it is observed that the peak at 783 nm is slightly asymmetric, indicating the presence of an additional shoulder peak at a lower wavelength. Therefore, to get more insight into the origin of PL emission, the normalized PL spectra are deconvoluted into three peaks named peak1, peak2, and peak3 at the emission wavelengths 754 nm (1.64 eV), 783 nm (1.58 eV), and 823 nm (1.50 eV) (instrumental noise), respectively, as shown in Fig. 3.5(b). The deconvoluted PL spectrum for λ_{ex} = 500 nm after proper baseline correction is shown in Fig. 3.5(b), and similarly, the deconvolution is done for all the PL spectra. The adjusted R^2 values of peak fitting for all the λ_{ex} listed in Table 3.1 are close to 1, indicating a good fit.

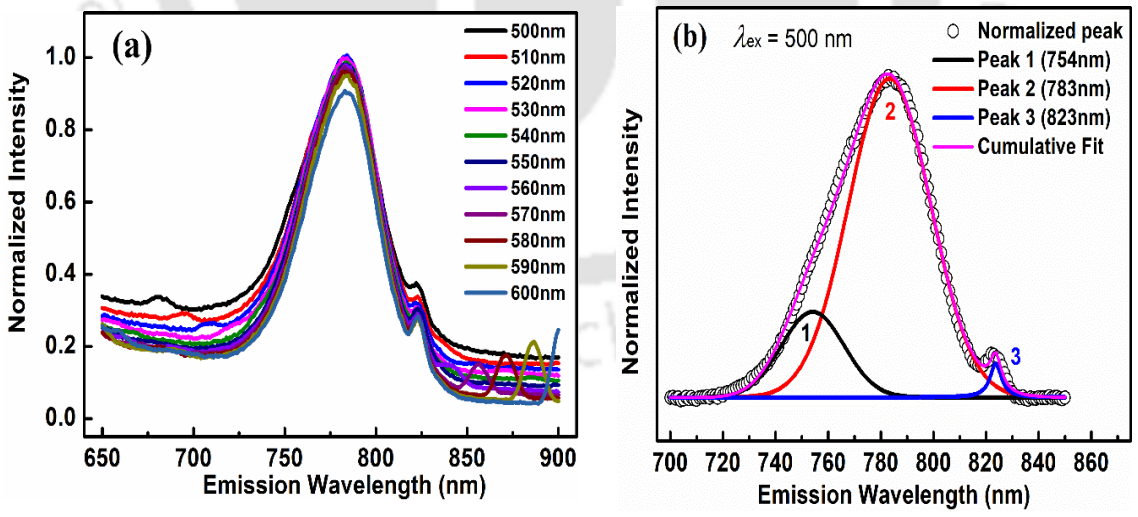

Figure 3.5: *(a) Normalized PL spectra of $MAPbI_3$ thin film at different excitation wavelengths (500-600 nm). The PL spectra are normalized with the incident photon flux of the respective excitation wavelengths after correcting reflection losses (b) The deconvoluted PL spectrum at λ_{ex}= 500 nm with the deconvoluted peaks*

***Table 3.1**: Adjusted R^2 value of the peak fit for PL spectra of $MAPbI_3$ thin film at different excitation wavelengths (500-600 nm)*

λ_{ex} (nm)	500	510	520	530	540	550	560	570	580	590	600
Adj. R^2	0.998	0.997	0.999	0.998	0.998	0.999	0.998	0.998	0.998	0.997	0.998

From the area percentage of the fitted peaks shown in Fig. 3.6, it is observed that the area percentage of peak1 is lower than that of peak2. Peak1 covers at least 10-20% area, and peak2 covers 80-90% area, whereas the instrumental noise peak3 area is <2-3%. There is no significant change in the positions of the deconvoluted peaks with the change in λ_{ex}. Though the variation in FWHM of peak1 (754 nm) is observed from 24 nm to 33 nm, there is no proper variation trend, and the FWHM of peak2 (783 nm) varies slightly from 35 nm to 39 nm.

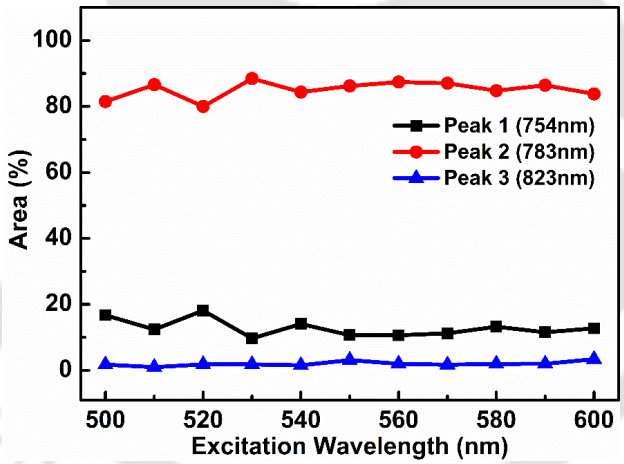

***Figure 3.6:** Area percentage of the peak1, peak2, and peak3 obtained after deconvolution of PL spectra at different excitation wavelengths (500-600 nm)*

These peak positions coincide with the absorption edges of the absorbance spectra, as shown in Fig. 3.7(a). From the peak1 and peak2 intensities, it can be comprehended that the majority of carriers get excited or thermalized to the slightly lower energy states after excitation, which emits photons of the energy ~1.58 eV after relaxation. On the other hand, the lower intensity of peak1 shows that fewer photoexcited carriers remain in the higher energy states, emitting photons having equivalent energy (~1.64 eV) to the bandgap

energy. These carrier recombination processes are shown schematically in Fig. 3.7(b), where two types of possible recombination occur: direct band-edge recombination and the other via shallow traps.

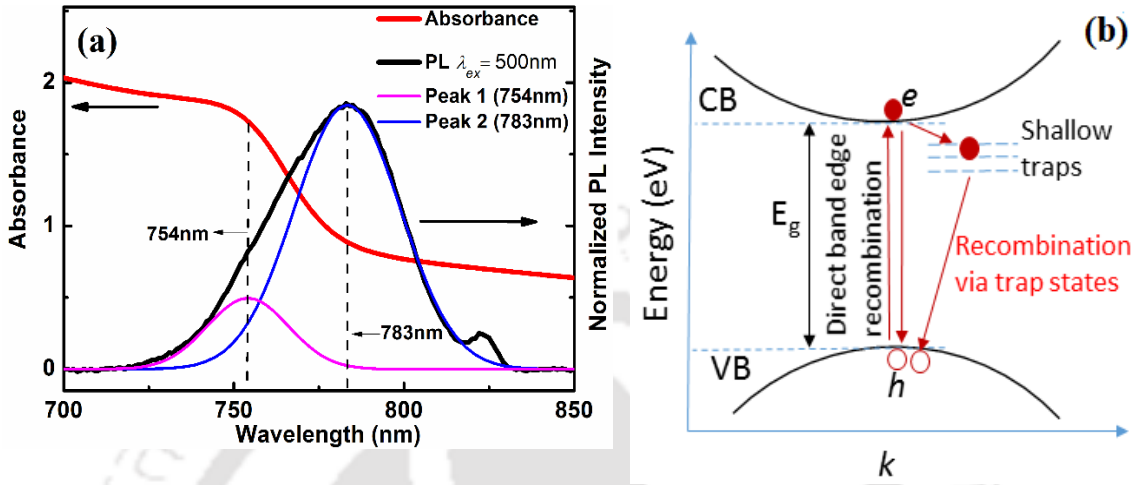

Figure 3.7: *(a) Absorbance and normalized PL spectra of $MAPbI_3$ thin film (λ_{ex} = 500 nm) with the deconvoluted PL peaks at 754 nm (peak1) and 783 nm (peak2) (b) Carrier recombination process, direct band edge and via shallow trap states*

Ideally, for $MAPbI_3$ perovskite with no defect states, only a single PL peak at ~1.60 eV should be observed, corresponding to its bandgap energy. Observation of intense peak at 1.58 eV indicates shallow trap states at ~60 meV (~2kT) below the conduction band minimum (~1.64 eV corresponding to low-intensity peak) in the bandgap energy region. Since the defect levels are very shallow, a fraction of the charge carriers trapped in these shallow traps are reemitted and direct band to band recombination occurs. Hence the direct band-edge recombination is responsible for PL peak1 at 754 nm (~1.64 eV) and another recombination process via shallow traps gives rise to intense PL peak2 at 783 nm (~1.58 eV). The major contribution to the PL is from the radiative recombination via these shallow trap states (peak2). These shallow traps can be attributed to the point defects such as iodine (I) and methylammonium (MA) vacancies in $MAPbI_3$ perovskite, which have low formation energies, and do not contribute to the non-radiative recombination [25-27]. Though a considerable amount of deep trap states can also be present in perovskite

materials, possibly originating from Pb interstitial (Pb_i) and anti-site defects (Pb_I, I_{MA}, I_{Pb}) [26, 28]. These deep defects result in non-radiative monomolecular recombination within perovskite films and do not contribute to PL [26]. Since these deep defects have higher formation energies and thus a low non-radiative recombination rate, long carrier diffusion lengths are observed in the halide perovskite. These lead halide perovskites have been shown to have intrinsic defect tolerance despite having several point defects, as the performance of solar cells is not affected significantly due to these shallow defects [26]. It is also believed that under certain excitation energy, the lowest vibrational level of conduction bands or highest vibrational level of valance bands are split and/or shifted when the photoexcitation energy is tuned around a threshold. The photoexcitation energy may cause some structural changes or deformation in halide perovskite, due to which the lowest level of the conduction bands (CB) or highest level of the valance bands (VB) may get split. As a result, the energy states can be shifted up or down, resulting in photoemission with relatively higher or lower energy than the ideal bandgap value [29]. This could be another reason for the peak at 1.64 eV in PL spectra.

To further understand the PL emission, PLE measurements were done by scanning over the excitation wavelengths. The PLE spectra normalized with incident photon flux for λ_{em}= 700-850 nm are shown in Fig. 3.8(a). The λ_{em} range is selected according to the broadness of the PL peak (700-850 nm). It is observed that the PLE intensity varies with λ_{em}; the intensity starts rising slowly from λ_{em} = 700 nm and reaches the maximum at ~780 nm, and again decreases towards higher λ_{em}. From PLE data in Fig. 3.8(a), the PL spectra are reconstructed for a clear illustration, as shown in Fig. 3.8(b). From Fig.3.8(b), it is seen that the PL peak in reconstructed spectra is similar to the measured PL spectra in Fig. 3.4, with the maximum intensity at λ_{em} ~780 nm. The peak intensity is maximum for the shorter λ_{ex} (470 nm) and decreases towards the longer λ_{ex}. In this reconstructed PL spectra also, a

signature of a small shoulder peak around ~755 nm is witnessed. The decrease in normalized PLE intensity with increasing excitation wavelength could be related to the slight decrease in absorption coefficient with wavelength.

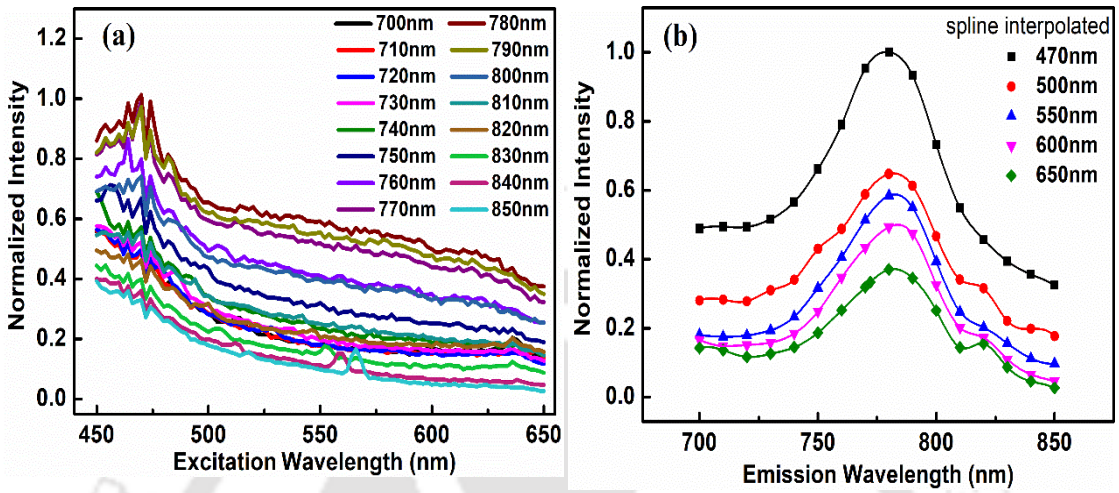

Figure 3.8: *(a) Normalized PLE spectra of $MAPbI_3$ thin film at the different emission wavelengths (700-850 nm). The spectra are normalized with the incident photon flux of the excitation wavelengths and corrected for the reflection losses (b) Reconstructed PL spectra from the PLE spectra in Fig. 3.8(a) at different excitation wavelengths (470-650 nm). The data points are spline interpolated*

3.2.5 Optical absorption fraction calculation

The optical absorption calculation for $MAPbI_3$ perovskite film is done to study the fractional absorption for different thicknesses and further explore the cause of the change in normalized peak intensity with λ_{ex}. Fig. 3.9 shows the calculated optical absorption in the wavelength range from 500- 650 nm using Eq. 3.2 for thickness 1- 400 nm [34].

$$Absorption = (1 - R(\lambda))\left(1 - e^{-\alpha(\lambda)d}\right) \tag{3.2}$$

Where R is reflectance, α is absorption coefficient as a function of wavelength (λ), and d is the film thickness. In general, the (1-$R(\lambda)$) factor is ignored if R = 0. However, in the case of $MAPbI_3$ perovskite the R is dependent on λ as can be seen in Fig. 3.3(b). So, the R is considered for the calculation of optical absorption.

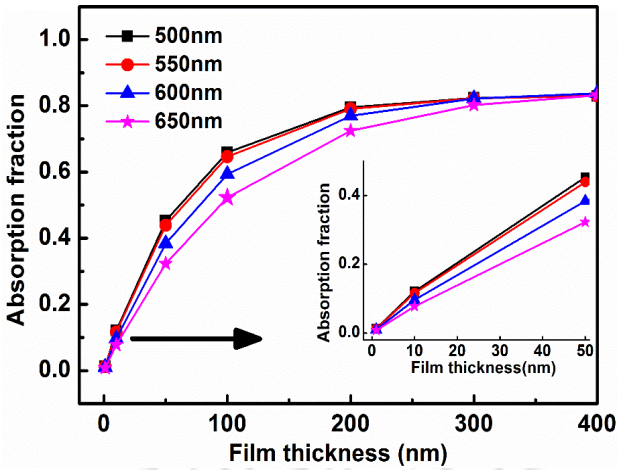

Figure 3.9: *Calculated optical absorption fraction of $MAPbI_3$ perovskite film for different film thicknesses at the wavelength range 500-650 nm. The inset figure shows the variation in absorption fraction of film surface region up to 50 nm thickness*

From Fig. 3.9, we can see that the fraction of light absorption increases with thickness and then saturates after 300 nm, which shows that the incident light is almost completely absorbed within a thickness of 300 nm. Corresponding to the variation in absorption coefficient with wavelength, the absorption fraction slightly decreases with the increase in wavelength for a few nm of initial film thickness (shown in figure inset). Since the absorption coefficient depends upon the wavelength slightly, the variation in PL intensity in Fig. 3.8(b) with λ_{ex} could be related to the variation in the number of photons absorbed within a certain thickness in the film surface region from which the PL spectra is obtained. On further investigation, it is found that for the film thickness ~ 50-60 nm, the ratios of the maximum absorption fraction at λ=500 nm to the corresponding absorption fractions at λ=550 nm, 600 nm & 650 nm are nearly similar to the ratios of the maximum normalized PL intensity at λ_{ex}=500 nm to its corresponding peaks at λ_{ex}=550 nm, 600 nm & 650 nm. This finding suggests that the emission from the perovskite film surface region of approximately 50-60 nm depth effectively contributes to the PL peak.

3.2.6 Transient current measurements

Current vs. time *(I-t)* measurements on $MAPbI_3$ thin films were performed to see the transient current response of the films on exposure to light and the current decay after the illumination is stopped to study the presence of defects. It can be observed from the *I-t* curve in Fig. 3.10 that the $MAPbI_3$ films show good photosensitivity with three orders of magnitude change in current when exposed to light (intensity ~100 $mWcm^{-2}$, for 60 secs). As soon as the light is turned on, the current increases instantaneously and gets stabilized. This fast generation process of photoexcited free carriers in $MAPbI_3$ perovskite occurs in picoseconds timescale [30, 31]. In $MAPbI_3$ perovskite, free charges are the primary species generated after photoexcitation above 80 K [32, 33]. As soon as the light is turned off, the current initially decays sharply, followed by a relatively slow decay before reaching back the dark current value. The inset figure particularly shows the current decay curve region after turning off the illumination. The fast band to band recombination cause sharp decay of current, while the slow decay of current is due to the slow re-emission of the trapped charge carriers in defect states.

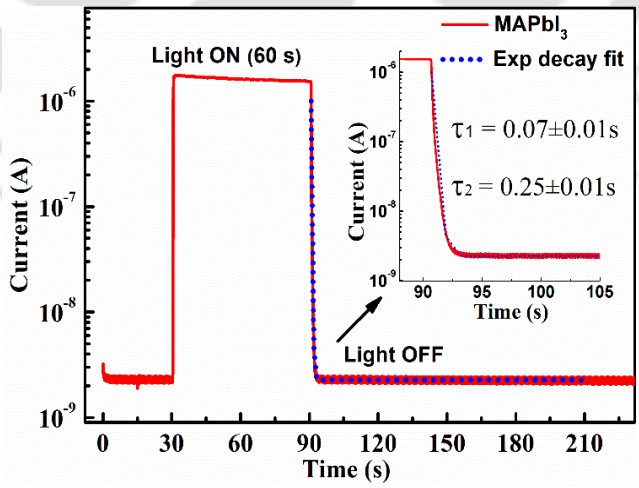

Figure 3.10: *Measured I-t characteristics of $MAPbI_3$ thin film for 60 s illumination. The inset figure shows the current decay curve region after the illumination is stopped at 90 s and the exponential decay fit is represented with the dotted line. By fitting the current decay curve, the decay time constant (τ_1 and τ_2) values are obtained*

To determine the decay time constants, the current decay curve (after illumination is stopped) is fitted using exponential decay Eq. 3.3.

$$I(t) = I_0 + A_1 e^{-(t-t_0)/\tau_1} + A_2 e^{-(t-t_0)/\tau_2} \quad (3.3)$$

Where $I(t)$ is current, I_o is offset, A_1 & A_2 are amplitude, τ_1 & τ_2 are decay time constants, and t_o is the starting point. The values of τ_1 and τ_2 obtained after fitting the decay current curve are 0.07±0.01 sec and 0.25±0.01 sec, where τ_1 and τ_2 values denote the slow decay process due to charges trapped in shallow defects levels.

3.3 Conclusion

In summary, we studied the optical properties of $MAPbI_3$ perovskite thin films using UV-Vis spectroscopy, PL, and PLE measurements. The excitation wavelength variation (500-600 nm) has no significant influence on the PL peaks. From the PL study, the shallow defect states in the bandgap region of the perovskite film could be identified. Understanding the defects in a semiconductor material is essential for designing and assessing the performance of optoelectronic devices. These shallow trap states could also be identified from the photocurrent decay study. The $MAPbI_3$ films have good photosensitivity and show two orders of magnitude change in current. This study gives a comprehensive understanding of the optical and electrical properties of $MAPbI_3$ perovskite thin film, which will help in developing new optoelectronic devices.

3.4 References

1. Baikie, T., et al., *Synthesis and crystal chemistry of the hybrid perovskite $(CH_3NH_3)PbI_3$ for solid-state sensitised solar cell applications.* Journal of Materials Chemistry A, 2013. **1**(18): p. 5628.

2. Sum, T.C. and N. Mathews, *Advancements in perovskite solar cells: photophysics behind the photovoltaics.* Energy & Environmental Science, 2014. **7**(8): p. 2518-2534.

3. Kong, W., et al., *Characterization of an abnormal photoluminescence behavior upon crystal-phase transition of perovskite $CH_3NH_3PbI_3$.* Physical Chemistry Chemical Physics, 2015. **17**(25): p. 16405-16411.

4. Noh, J.H., et al., *Chemical management for colorful, efficient, and stable inorganic-organic hybrid nanostructured solar cells.* Nano Letters, 2013. **13**(4): p. 1764-9.

5. Basumatary, P. and P. Agarwal, *A short review on progress in perovskite solar cells.* Materials Research Bulletin, 2022. **149**: p. 111700.

6. Abbas, H.A., et al., *High efficiency sequentially vapor grown n-i-p $CH_3NH_3PbI_3$ perovskite solar cells with undoped P3HT as p-type heterojunction layer.* APL Materials, 2015. **3**(1): p. 016105.

7. Chiang, C.-H. and C.-G. Wu, *A Method for the Preparation of Highly Oriented $MAPbI_3$ Crystallites for High-Efficiency Perovskite Solar Cells to Achieve an 86% Fill Factor.* ACS Nano, 2018. **12**(10): p. 10355-10364.

8. Yang, X., et al., *Efficient green light-emitting diodes based on quasi-two-dimensional composition and phase engineered perovskite with surface passivation.* Nature Communications, 2018. **9**(1): p. 1-8.

9. Dou, L., et al., *Solution-processed hybrid perovskite photodetectors with high detectivity.* Nature Communications, 2014. **5**(1): p. 5404.

10. Zhu, H., et al., *Lead halide perovskite nanowire lasers with low lasing thresholds and high quality factors.* Nature Materials, 2015. **14**(6): p. 636-42.

11. Wang, X., et al., *Recent progress in organometal halide perovskite photodetectors.* Organic Electronics, 2018. **52**: p. 172-183.

12. Miller, O.D., E. Yablonovitch, and S.R. Kurtz, *Strong internal and external luminescence as solar cells approach the Shockley–Queisser limit.* IEEE Journal of Photovoltaics, 2012. **2**(3): p. 303-311.

13. Fang, H.H., et al., *Photophysics of organic–inorganic hybrid lead iodide perovskite single crystals.* Advanced Functional Materials, 2015. **25**(16): p. 2378-2385.

14. Yamada, Y., et al., *Photocarrier recombination dynamics in perovskite $CH_3NH_3PbI_3$ for solar cell applications.* J Am Chem Soc, 2014. **136**(33): p. 11610-3.

15. Kiligaridis, A., et al., *Excitation wavelength dependence of photoluminescence flickering in degraded $MAPbI_3$ perovskite and its connection to lead iodide formation.* Journal of Luminescence, 2020. **222**: p. 117129.

16. Liu, X., C. Xu, and E.-C. Lee, *Chlorobenzene-Mediated Control of Crystallization in Perovskite Films for High-Performance Solar Cells.* ACS Applied Energy Materials, 2020. **3**(12): p. 12291-12297.

17. Zhou, Y., et al., *Growth control of compact $CH_3NH_3PbI_3$ thin films via enhanced solid-state precursor reaction for efficient planar perovskite solar cells.* Journal of Materials Chemistry A, 2015. **3**(17): p. 9249-9256.

18. Chiang, C.-H., Z.-L. Tseng, and C.-G. Wu, *Planar heterojunction perovskite/ PC $_{71}$BM solar cells with enhanced open-circuit voltage via a (2/1)-step spin-coating process.* Journal of Materials Chemistry A, 2014. **2**(38): p. 15897-15903.

19. Guo, X., et al., *Identification and characterization of the intermediate phase in hybrid organic–inorganic $MAPbI_3$ perovskite.* Dalton Transactions, 2016. **45**(9): p. 3806-3813.

20. Thakur, U., et al., *Investigation into the advantages of pure perovskite film without PbI_2 for high performance solar cell.* Scientific reports, 2016. **6**: p. 35994.

21. Bi, C., et al., *Understanding the formation and evolution of interdiffusion grown organolead halide perovskite thin films by thermal annealing.* Journal of Materials Chemistry A, 2014. **2**(43): p. 18508-18514.

22. Fujiwara, H., et al., *Optical Characteristics and Operational Principles of Hybrid Perovskite Solar Cells.* physica status solidi (a), 2018. **215**(12): p. 1700730.

23. Eom, K., et al., *Depth-resolved band alignments of perovskite solar cells with significant interfacial effects.* Journal of Materials Chemistry A, 2017. **5**(6): p. 2563-2571.

24. Yamada, Y., et al., *Near-band-edge optical responses of solution-processed organic–inorganic hybrid perovskite $CH_3NH_3PbI_3$ on mesoporous TiO_2 electrodes.* Applied Physics Express, 2014. **7**(3): p. 032302.

25. Kovalenko, M.V., L. Protesescu, and M.I. Bodnarchuk, *Properties and potential optoelectronic applications of lead halide perovskite nanocrystals.* Science, 2017. **358**(6364): p. 745-750.

26. Yin, W.-J., T. Shi, and Y. Yan, *Unusual defect physics in $CH_3NH_3PbI_3$ perovskite solar cell absorber.* Applied Physics Letters, 2014. **104**(6): p. 063903.

27. Meggiolaro, D. and F. De Angelis, *First-Principles Modeling of Defects in Lead Halide Perovskites: Best Practices and Open Issues.* ACS Energy Letters, 2018. **3**(9): p. 2206-2222.

28. Heo, S., et al., *Deep level trapped defect analysis in $CH_3NH_3PbI_3$ perovskite solar cells by deep level transient spectroscopy.* Energy & Environmental Science, 2017. **10**(5): p. 1128-1133.

29. Qarony, W., et al., *Excitation Wavelength Dependent Reversible Photoluminescence Peak in Iodide Perovskites.* arXiv: Optics 2018.

30. Ponseca, C.S., Jr., et al., *Organometal halide perovskite solar cell materials rationalized: ultrafast charge generation, high and microsecond-long balanced mobilities, and slow recombination.* J Am Chem Soc, 2014. **136**(14): p. 5189-92.

31. Valverde-Chávez, D.A., et al., *Intrinsic femtosecond charge generation dynamics in single crystal $CH_3NH_3PbI_3$.* Energy & Environmental Science, 2015. **8**(12): p. 3700-3707.

32. Milot, R.L., et al., *Temperature-Dependent Charge-Carrier Dynamics in $CH_3NH_3PbI_3$ Perovskite Thin Films.* Advanced Functional Materials, 2015. **25**(39): p. 6218-6227.

33. Wehrenfennig, C., et al., *High Charge Carrier Mobilities and Lifetimes in Organolead Trihalide Perovskites.* Advanced Materials, 2014. **26**(10): p. 1584-1589.

34. Wang, L., M.T. Wilson, and N.M. Haegel, *Interpretation of photoluminescence excitation spectroscopy of porous Si layers.* 1993. **62**(10): p. 1113-1115

CHAPTER 4

Synthesis and study of $MAPbI_3$ perovskite thin films deposited using two-step method

This chapter discusses the growth, structural, optical and electrical properties of $MAPbI_3$ perovskite thin films deposited by two-step deposition methods. Usually, the perovskite thin films are deposited using one-step solution process. However, the perovskite layer deposition by the one-step spin coating process has the limitation of small area film coverage [1]. Thus, with the motivation of depositing large-area films and improving the stability of the perovskite layer, we have used the two-step method for fabricating the perovskite film by involving the thermal evaporation technique. In the two-step method, the first step is the thermal evaporation (TE) of lead iodide (PbI_2), and the second is the dip coating (DC) in methylammonium iodide (CH_3NH_3I or MAI) solution to fabricate methylammonium lead iodide ($CH_3NH_3PbI_3$ or $MAPbI_3$) perovskite film. At the same time, we have also used the conventional spin coating (SC) method for depositing

PbI_2 film and then DC in MAI to get $MAPbI_3$ for comparative study with the TE+DC method. The film morphology, optical properties, electrical properties, and stability of $MAPbI_3$ perovskite films synthesized by both the two-step methods TE+DC and SC+DC are studied. The effects of depositing PbI_2 film by thermal evaporation and spin coating on perovskite film quality are discussed. Transient current measurements were done to study the carrier generation, trapping and recombination processes in $MAPbI_3$ perovskite thin films deposited by the TE+DC method.

4.1 Experimental details

$MAPbI_3$ thin films were prepared on Corning 1737 glass substrate using the two-step methods TE+DC and SC+DC as described in chapter 2, section 2.2.2. The X-ray diffraction (XRD), Field Emission Scanning Electron Microscope (FESEM) and Atomic Force Microscope (AFM) were used to study the structural and surface morphology of perovskite thin films. Optical absorption, transmission, and reflectance spectra were measured using a UV-Vis-NIR spectrometer. Photoluminescence (PL) spectra were recorded at varying excitation wavelengths (λ_{ex}). Stability tests were done on the perovskite thin films prepared by the two different two-step methods (TE+DC & SC+DC) using UV-Vis absorbance and electrical measurements as a function of time. The current vs. voltage (*I-V*) and current vs. time (*I-t*) measurements on the perovskite films were done in coplanar geometry using the Keithley-2450 source measurement unit at an applied field of 100 Vcm^{-1}. The *I-t* measurements were done in vacuum (0.05 mbar) to avoid surface-related processes induced by chemisorption and desorption of oxygen [2].

4.2 Results and discussion

4.2.1 X-ray diffraction analysis

Fig. 4.1(a-b) shows the XRD patterns of the PbI_2 (vapor-deposited and spin-coated) and $MAPbI_3$ thin films for different dipping time durations.

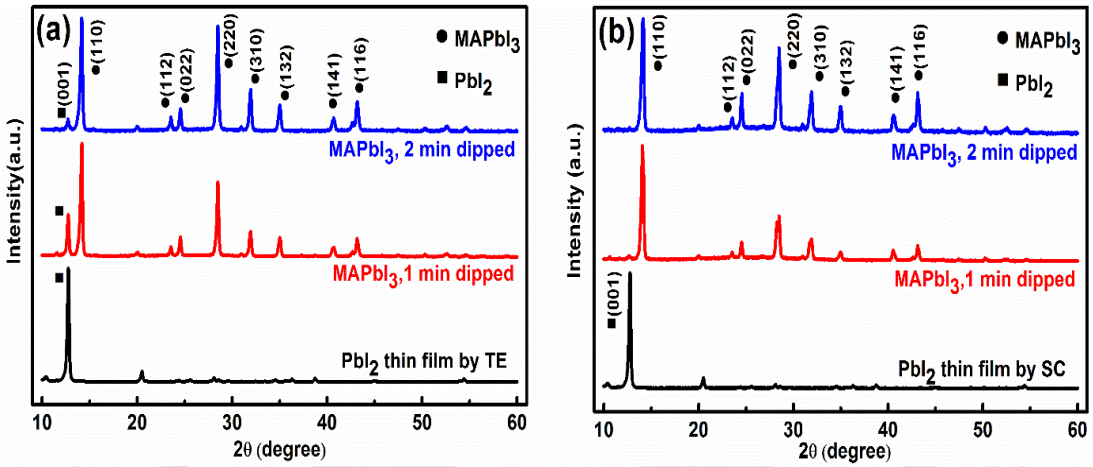

Figure 4.1: *XRD patterns of PbI_2 and $MAPbI_3$ thin films with different dipping times of PbI_2 film in MAI solution. (a) thermally evaporated PbI_2 and $MAPbI_3$ thin films, (b) spin-coated PbI_2 and $MAPbI_3$ thin films*

The indexed XRD peaks confirm the complete formation of $MAPbI_3$ (PbI_2+MAI→$MAPbI_3$) perovskite films after dipping PbI_2 films in MAI solution for about 2 minutes. The observed peaks correspond to the pure tetragonal (β) phase of $MAPbI_3$ films prepared by both the methods (TE+DC and SC+DC) [3-5]. The XRD pattern shows that the perovskite films have high purity with significantly fewer intermediate phases. A preferred orientation along the (110) direction was observed in the XRD pattern of $MAPbI_3$ films synthesized by both methods. After 2 minutes of dipping the TE and SC PbI_2 films in MAI solution, the PbI_2 peak intensity at 2θ value of 12.6° diminishes and the $MAPbI_3$ peaks become prominent [6]. However, $MAPbI_3$ film using the vapor-deposited PbI_2 film shows a small peak of PbI_2 (at a 2θ value of 12.6°), indicating the presence of a small fraction of unreacted PbI_2. The fraction of unreacted PbI_2 is possibly present at the

bottom of the film because the PbI_2 films obtained by vapor deposition are more compact than spin-coated films. Depending on the batch of sample preparation, the vapor-deposited PbI_2 films sometimes require a slightly longer dipping time to react with MAI to form $MAPbI_3$ completely.

4.2.2 FESEM analysis

Figure 4.2(a-b) shows the FESEM images of $MAPbI_3$ films synthesized using the two-step methods. The vapor-deposited PbI_2 films form perovskite film (Fig. 4.2(a)) with large grain sizes up to 1 μm, while the spin-coated PbI_2 films (Fig. 4.2(b)) form perovskite films with smaller grain size and pinholes. The pinholes in the SC+DC films are formed after the solvent evaporation during annealing, which shows the drawback of the solution process for fabricating large-area films or devices. These observations indicate that TE+DC perovskite films are likely to show better device performance because the films are pinhole-free and large grain-sized films exhibit good transport properties due to less grain boundary density [7].

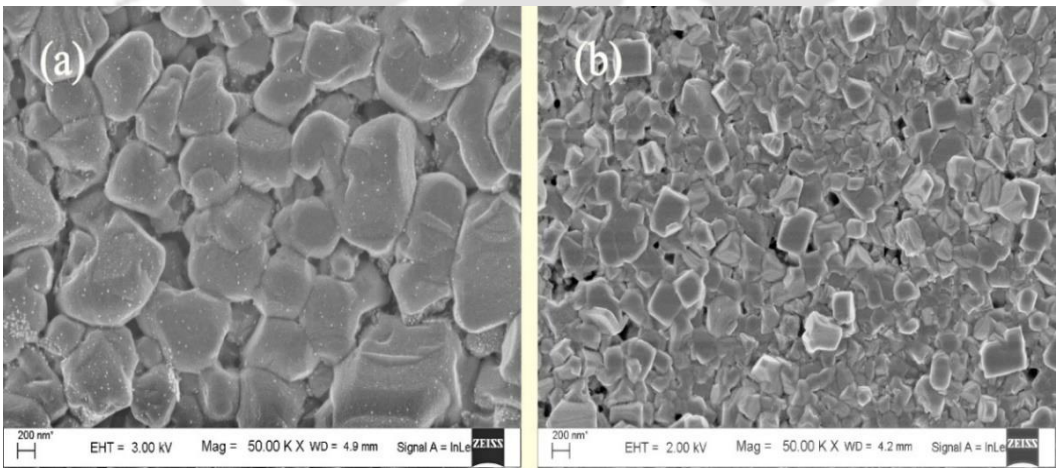

Figure 4.2: *FESEM images of $MAPbI_3$ films prepared by (a) thermal evaporation of PbI_2 and dip coating in MAI solution (b) spin coating of PbI_2 and dip coating in MAI solution*

4.2.3 AFM analysis

Fig. 4.3(a-d) shows the AFM topography images (5 µm × 5 µm) of PbI_2 and $MAPbI_3$ thin films.

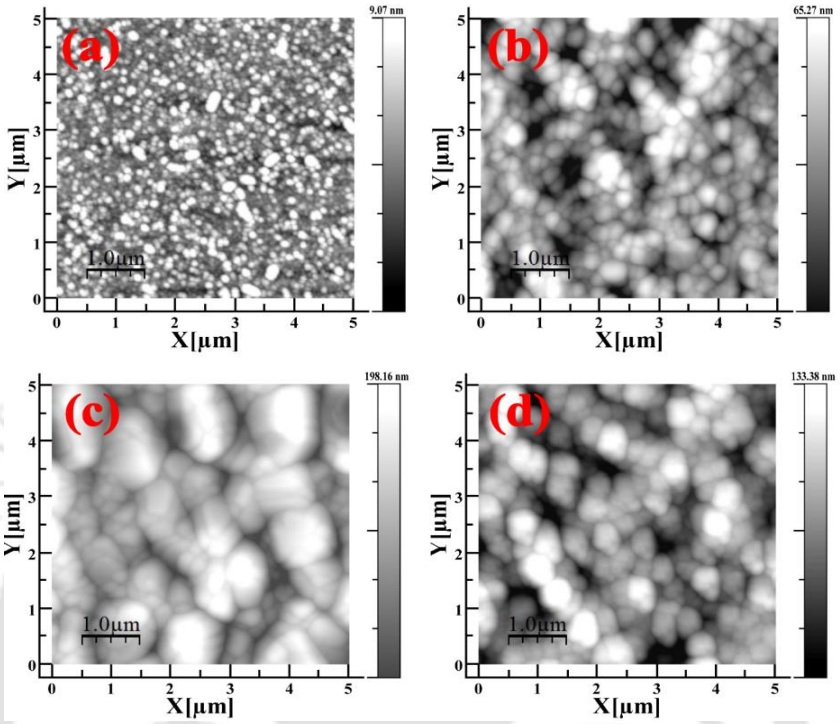

Figure 4.3: *AFM topography images of PbI_2 and $MAPbI_3$ thin films by dip-coating PbI_2 in MAI solution. (a) thermally evaporated PbI_2 film, (b) spin-coated PbI_2 film, (c) $MAPbI_3$ thin film by thermally evaporated PbI_2 film and dip coating and, (d) $MAPbI_3$ thin film by spin-coated PbI_2 film and dip coating*

It is observed that the vapor-deposited PbI_2 films (Fig. 4.3a) are smoother than the spin-coated films (Fig. 4.3b). The vapor-deposited films have uniform coverage and a lower root mean square (RMS) roughness of 2.28±0.40 nm than the spin-coated films with the RMS roughness of 16.35±3.27 nm. The higher roughness is due to the presence of pinholes as observed in the AFM image of spin-coated PbI_2 films. This non-uniformity and pinholes are not suitable for a large-area device. As observed in the FESEM image, $MAPbI_3$ films synthesized by the TE+DC films (Fig. 4.3c) have uniform coverage with a larger grain size than SC+DC films (Fig. 4.3d). The RMS roughness of TE+DC (49.63±8.57 nm) films is higher due to the presence of large size grains than in the SC+DC films (33.39±6.16

nm). In thermal evaporation, the surface energy gets enhanced due to elevated substrate temperature (100 °C). Hence, uniform nucleation and growth of PbI_2 occur throughout the substrate leading to large grain growth in perovskite film with full surface coverage. However, the PbI_2 films spin-coated at room temperature followed by annealing did not give uniform film growth.

4.2.4 UV-Vis analysis

The UV-Vis absorbance spectra of $MAPbI_3$ perovskite thin films prepared by TE+DC and SC+DC are shown in Fig. 4.4(a-b). The absorbance measurements were started after 30 minutes of film deposition. The $MAPbI_3$ perovskite films have a sharp absorption edge at ~780 nm, almost covering the visible range, which shows the characteristic of $MAPbI_3$ perovskite film [3, 8]. This optical absorption nature is consistent with XRD patterns, confirming the perovskite formation. The optical bandgap was estimated from the absorbance data using the Tauc plot $(\alpha h\nu)^{1/n}$ *vs.* $h\nu$, where α is the absorption coefficient (cm^{-1}), $h\nu$ is the photon energy (eV), and n = ½ for direct bandgap material [9]. The calculated bandgaps of fresh $MAPbI_3$ films are 1.55±0.02 eV and 1.54±0.02 eV for TE+DC and SC+DC films, respectively. The bandgap values are slightly lower than the reported values (~ 1.6 eV) in the literature [10]. As shown in Fig. 4.4(c), the transmittance (T) and diffuse reflectance (R) spectra of TE+DC $MAPbI_3$ thin film decrease sharply starting from ~ 780 nm towards lower wavelength, corresponding to its bandgap absorption. The low values of T and R below ~780 nm in the visible region are due to the high absorption coefficient of $MAPbI_3$ perovskite at the photon energies above its bandgap energy.

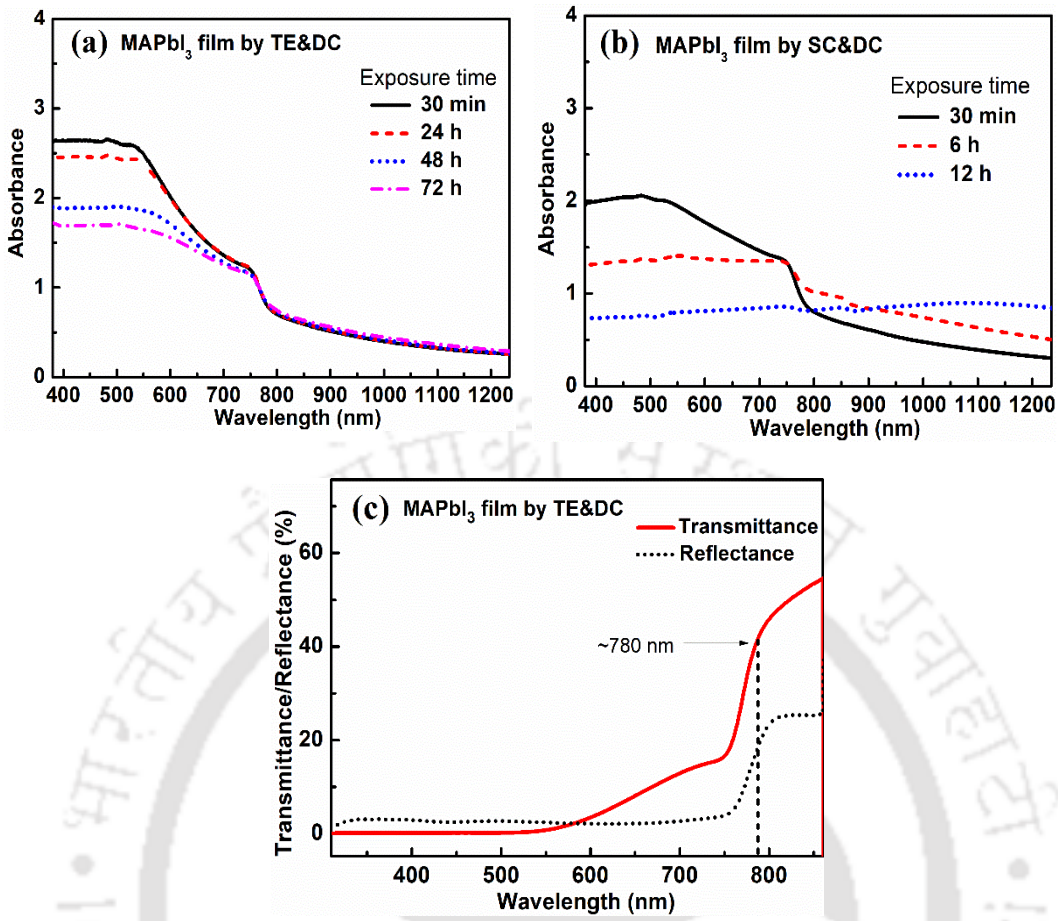

Figure 4.4: *UV-Vis absorbance spectra of $MAPbI_3$ thin films with respect to exposure time in the air, (a) thermal evaporation of PbI_2 and dip coating, (b) spin coating of PbI_2 and dip coating, (c) Transmittance and diffuse reflectance spectra of TE+DC $MAPbI_3$ thin film*

For the stability test of $MAPbI_3$ films, the absorbance spectra were recorded as a function of exposure time by subjecting the $MAPbI_3$ thin films continuously to ambient conditions with a high *RH* of 76% - 88%. It is observed from Fig. 4.4(a) that the absorbance of TE+DC film decreases slowly with time as it starts degrading. Remarkably, the absorbance spectra showed the characteristics of perovskite even up to 72 hrs. Whereas the SC+DC thin-film degraded entirely within 12 hrs, as seen in Fig. 4.4(b). These observations confirm that the degradation rate is relatively slow in TE+DC perovskite films, even at high *RH*, compared to SC+DC films. The fast degradation of SC+DC film is due to pinholes in the film, as seen in the FESEM and AFM images. The complete solution processing steps of SC+DC have led to the formation of pinholes in the $MAPbI_3$

films, thus making them more susceptible to moisture effects [11]. As a result, fast degradation of the films occurs in the air with high humidity, whereas pinhole-free TE+DC films with large size grains exhibit better stability. Eventually, the dark brown fresh films turn to faded yellow after complete degradation.

4.2.5 Electrical conductivity

The current vs. voltage (*I-V*) measurements of as-deposited $MAPbI_3$ thin films by TE+DC and SC+DC were carried out at an incident power density of ~1000 Wm^{-2} to calculate the dark (σ_d) and photo (σ_{ph}) conductivity. The measurements were done at 24 hrs time intervals to see the degradation effect on σ_d and σ_{ph}. The σ_d and σ_{ph} of $MAPbI_3$ films as a function of storage time are shown in Fig. 4.5. Equation (4.1) is used to calculate the electrical conductivity of the $MAPbI_3$ thin film.

$$\sigma = \frac{I \times d}{V \times l \times t} \tag{4.1}$$

Where *I* is the measured current, *V* is the applied voltage, *d* is the separation between the electrodes, *l* is the length of the electrode, and *t* is the thickness of the film.

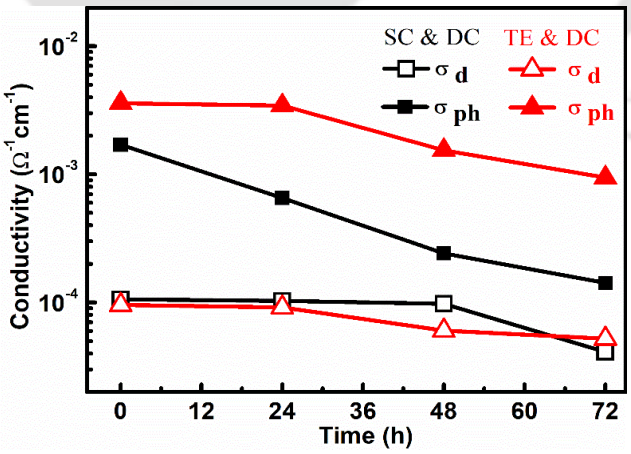

Figure 4.5: *Dark and photoconductivity of as-deposited $MAPbI_3$ thin films measured with respect to storage time*

The TE+DC film has a higher σ_{ph} than the SC+DC film. Further σ_{ph} degrades faster for the SC+DC films with aging. The σ_d for both TE+DC and SC+DC films are almost the same and not much change is observed with storage time. Thus for both TE+DC and SC+DC films, σ_{ph} degrades faster than the σ_d. The σ_{ph} indicates that for almost 24 hrs, no degradation in TE+DC film is observed, whereas the SC+DC film degrades right from the beginning at a constant rate, which is consistent with the UV-Vis absorption spectra with exposure time in air [Fig. 4.4(a-b)]. The TE+DC film starts degrading slowly after 24 hrs, signifying that the rate of degradation in the TE+DC film is slower than the SC+DC film, which is consistent with the degradation rate observed in UV-Vis absorbance spectra (Fig.4.4). This is because the compact and dense films by TE+DC are more resilient to moisture than the porous films by SC+DC, which gets easily affected by moisture. Therefore, it can be concluded that the TE+DC films are more suitable for device application as it has higher photoconductivity and better stability compared to SC+DC films.

4.2.6 PL and PLE analysis

As it has been found that the $MAPbI_3$ thin films by the TE+DC method have better stability than SC+DC films, so the PL and PLE analysis were done only for TE+DC films. Fig. 4.6(a) shows the normalized photoluminescence (PL) spectra of $MAPbI_3$ thin film (TE+DC) at room temperature (~300 K) for a selected range of excitation wavelength (λ_{ex}) from 500 nm to 600 nm. The PL spectra are normalized by the incident photo flux corresponding to the λ_{ex} after considering the reflection (R) losses for quantitative analysis. The normalized peak intensity decreases with increasing $\lambda_{ex,}$ corresponding to the lower absorption coefficient for longer λ photons (already discussed in Chapter-3). A high-intensity PL peak at ~772 nm (1.60 eV) is observed for all the λ_{ex} corresponding to the

bandgap energy of $MAPbI_3$ perovskite film. The peak position is slightly higher than the bandgap value (~1.57 eV) estimated from the UV-Vis absorbance data but close to the reported bandgap value of ~1.60 eV of the tetragonal structure $MAPbI_3$ [12].

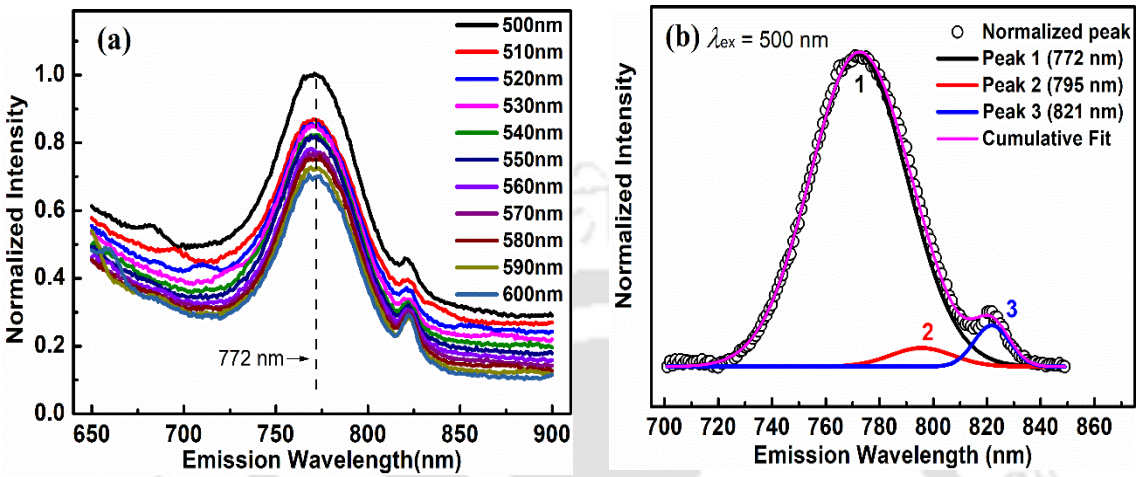

Figure 4.6: *(a) Normalized PL spectra of $MAPbI_3$ thin film at different excitation wavelengths (500-600 nm). The PL spectra are normalized with the photon flux of the respective excitation wavelengths after correcting reflection losses (b) The deconvoluted PL spectrum at λ_{ex}= 500 nm with the deconvoluted peaks peak1, peak2 and peak3*

There is no shift in the peak positions with λ_{ex}, though a decrease in the peak intensity is observed towards the longer λ_{ex} due to decreased photon absorption. The minor peak observed at ~821 nm is identified as an instrumental noise and is supposed not to affect the PL spectra. The normalized PL spectra in the 700 - 850 nm range are deconvoluted to get more insight into the PL emission. The PL spectra are deconvoluted into three peaks named peak1, peak2, and peak3 at the emission wavelengths 772 nm, 795 nm, and 821 nm (instrumental noise), respectively, as shown in Fig. 4.6(b). The deconvoluted PL spectrum for λ_{ex} = 500 nm after proper baseline correction is shown in Fig. 4.6(b).

Similarly, deconvolution is done for all the PL spectra at different λ_{ex}. The adjusted R^2 value of PL peak fitting for all the λ_{ex} (500 - 600 nm) lies between 0.996 to 0.999, indicating a good fit. The central peak at 772 nm is deconvoluted into two peaks, a high-

intensity peak at a photon energy of 1.60 eV (peak1) and a low-intensity peak at a lower photon energy of 1.55 eV (peak2). These peak intensities indicate that majority of the photoexcited carriers emit photons of the energy equivalent to bandgap energy 1.60 eV after relaxation, and only a few carriers emit photons having slightly lower energy of ~1.55 eV. This lower energy emission shows the presence of shallow trap states near the conduction band edge through which a few charge carriers recombine and emits photons of the energy lower than the bandgap energy (1.55 eV). In contrast to the PL spectra for films deposited in one-step (Chapter-3), the PL peak intensity is more for the high energy peak compared to the low energy peak indicating that the defect density at a shallow level is much less in the films deposited by two-step, which could be due to the more dense and compact nature of TE+DC films.

To further understand the PL emission, PLE measurements were done by scanning over the excitation wavelengths. The photoluminescence excitation (PLE) spectra normalized with incident photon flux for emission wavelength (λ_{em}) from 700 nm to 850 nm are shown in Fig. 4.7(a). It is observed that the PLE intensity varies with the λ_{em}; the intensity starts rising slowly from λ_{em} = 700 nm and reaches the maximum at ~770 nm, and again decreases towards higher λ_{em}. The PLE peak intensity is highest at λ_{ex} = 470 nm and decreases towards the longer λ_{ex}. The decrease in normalized PLE intensity with increasing excitation wavelength could be related to the slight decrease in photon absorption with wavelength. From PLE data in Fig. 4.7(a), the PL spectra are reconstructed for a clear illustration, as shown in Fig. 4.7(b). It is realized that the PL spectra in Fig.4.7(b) are similar to the PL spectra shown in Fig. 4.6(a), with the maximum intensity at λ_{em} ~770 nm. The peak intensity is maximum for the shorter λ_{ex} (470 nm) and decreases towards the longer λ_{ex}. The decrease in the PL intensity with increasing λ_{ex} can be correlated to the slight decrease in photon absorption in the 500 nm to 600 nm wavelength.

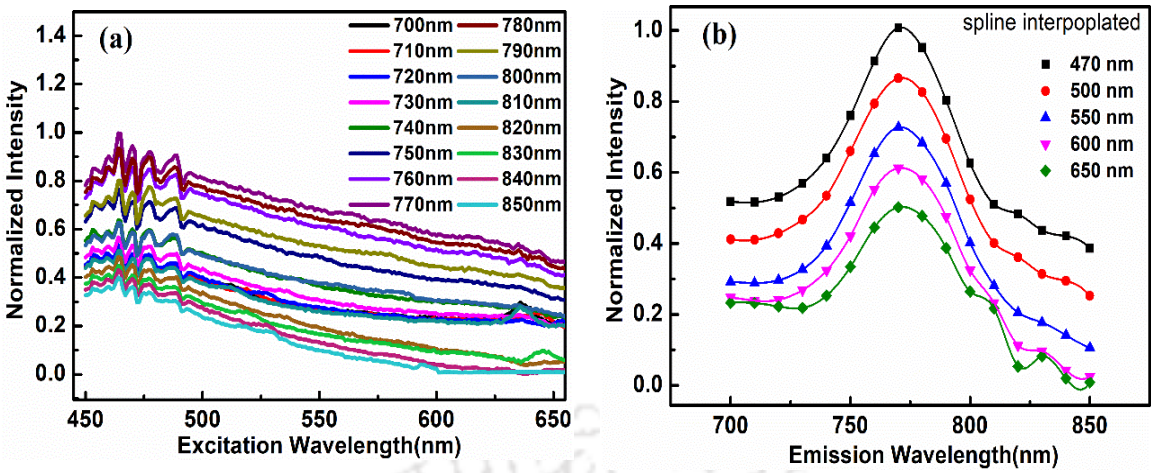

Figure 4.7: *(a) Normalized PLE spectra of $MAPbI_3$ thin film at the different emission wavelengths (700-850 nm). The spectra are normalized with the incident photon flux of the excitation wavelengths and corrected for the reflection losses (b) Reconstructed PL spectra from the PLE spectra in Fig. 4.7(a) at different excitation wavelengths (470-650 nm). The PL data points are spline interpolated*

4.2.7 Transient current measurements of $MAPbI_3$ thin films

In an optoelectronic device, the charge-carrier dynamics and performance are mainly determined by the carrier generation, transport, and recombination processes related to surface and bulk defects [13-15]. The presence of traps and recombination centers in the perovskite films arising from chemical impurities or structural defects affects the device performance [16-18]. Therefore, it is essential to understand the charge transport mechanisms such as charge carrier generation and recombination process in perovskite material. Thus, current Vs. time (*I-t*) measurements for the transient current are done on the stable perovskite films synthesized by the TE+DC method to understand the charge transport mechanisms. Fig. 4.8(a-d) shows the *I-t* characteristics of $MAPbI_3$ films at the different durations of illumination and varying light intensity at different temperatures. Fig. 4.8(e) shows the transient photocurrent at an intensity of 100 Wm^{-2} at 25 °C. An expanded view of the transient photocurrent in Fig. 4.8(e) for 30 sec illumination is shown in Fig. 4.8(f) to get more insight into the photocurrent decay during illumination.

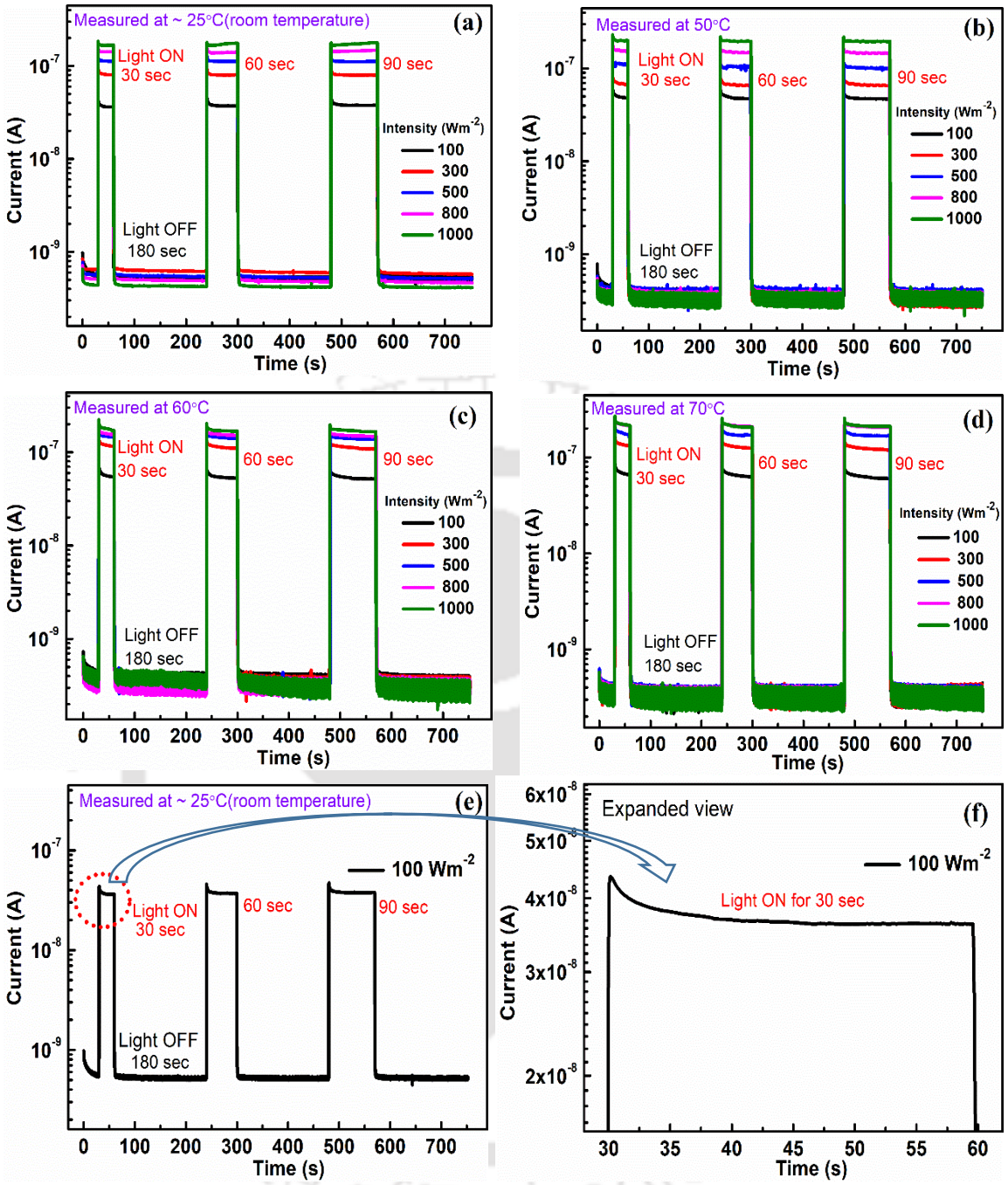

Figure 4.8: *Measured I-t characteristics of $MAPbI_3$ film by TE+DC, (a-d) transient current of $MAPbI_3$ film for different duration of illumination and varying light intensity at different temperatures, (e) transient current of $MAPbI_3$ film for different duration of illumination at 25 °C for illumination intensity of 100 Wm^{-2} and (f) expanded view of transient photocurrent for 30 sec illumination [encircled with dots in fig. (e)]*

It can be observed that the $MAPbI_3$ films show good photosensitivity with more than two orders of magnitude change in current when exposed to full intensity (~1000 Wm^{-2}) of light. As soon as the light is turned on, the current increases instantaneously. This rapid

rise of photocurrent can be attributed to the quick generation of electron-hole pairs at a time scale of picoseconds due to the absorption of photons having comparable energy or more than the bandgap energy. However, a slight decrease in current was observed during continuous illumination before a stabilized value was reached. The thermally generated traps are responsible for the current decay during illumination. These traps could be both shallow and deep with a large capture cross-section and slow re-emission rate. In steady-state, trapping and re-emission rates are similar; thus, a nearly steady-state current value is achieved. In some cases, small oscillations were observed in the transient current under the light which could be due to a competition between the trapping and re-emission of charge carriers in the traps. The stabilized current is about 90% of its maximum value during illumination and was achieved in a time scale of 1-10 seconds of illumination. The stabilized value of current did not depend upon exposure time, as the photocurrent remains almost constant for different exposure times (30 sec, 60 sec and 90 sec) for particular light intensity at a given temperature. However, the stabilized photocurrent increased with light intensity and is weakly dependent upon temperature. The initial decay of current observed in our case during illumination after reaching a peak value is not typical for semiconductor films. Usually, a sharp rise in current followed by a slow rise has been reported in the literature [19]. The major contribution to the photocurrent in these cases comes from the band to band transition of the electrons after the absorption of photons and the subsequent slow rise in current with time is understood in terms of the trapping of excess charge carriers in band tail and defect states followed by subsequent slow re-emission from these states.

After turning off the light, initially, the current decayed sharply, followed by a relatively slow decay before reaching the dark value. The trend is observed in all the measurement conditions, independent of illumination time, light intensity, or film temperature. It can be

noted from Fig. 4.8(a-d) that as we increase the temperature, the noise in the dark current increases, which could be due to continuous trapping and re-emission of the excess carrier generated during illumination.

4.2.7.1 Transient current during illumination

The decay part of the transient current during illumination is fitted with two exponential decay characteristics given by Eq. 4.2 and the obtained time constant values are listed in Table 4.1. The decay curve fitting was done for the first 10 sec of the transient photocurrent from the peak value to avoid the difficulty of fitting the fluctuating photocurrent beyond 10 sec.

Exponential decay Eq.4.2 is used for fitting current decay curves.

$$I(t) = I_0 + A_1 e^{-(t-t_0)/\tau_1} + A_2 e^{-(t-t_0)/\tau_2} \tag{4.2}$$

Where, $I(t)$ is current, I_o is offset, A_1 & A_2 are amplitude, τ_1 & τ_2 are decay time constants and t_o is the starting point. We have written the decay time constants as τ_{L1}, τ_{L2} and τ_{d1}, τ_{d2} for current decay curves under illumination and dark conditions, respectively.

Table 4.1: *Photocurrent decay time constant values obtained by fitting current decay curves at full intensity (~1000 Wm^{-2}) for the first 10 sec of the 30 sec exposure time at different temperatures*

Temperat-ure	25 °C		50 °C		60 °C		70 °C	
decay time constants	τ_{L1}(sec)	τ_{L2}(sec)	τ_{L1}(sec)	τ_{L2}(sec)	τ_{L1}(sec)	τ_{L2}(sec)	τ_{L1}(sec)	τ_{L2}(sec)
	0.19±0.02	0.94±0.05	0.27±0.05	3.76±0.26	0.52±0.01	4.25±0.19	0.42±0.01	7.05±0.39

It is observed that the values of both τ_{L1} and τ_{L2} depend upon temperature. The τ_{L1} varies from 0.19 sec to 0.52 sec as the temperature is increased from 25 ^oC to70 ^oC, whereas a much-pronounced increase in τ_{L2} is observed with temperature, which changes from 0.94 sec to 7.05 sec in the same temperature range. The initial sharp decay is thus due to the

trapping of carriers in the thermally generated traps characterized by a large capture cross-section and a short decay time. On the other hand, the subsequent slow decay during illumination is likely due to the capture of photogenerated carriers by the shallow traps having mostly unoccupied states. These traps have high filling rates and a much lower re-emission rate. As the temperature increases, the re-emission rate increases, and it takes longer to achieve the saturated current value.

4.2.7.2 Transient current after illumination turned off

As shown in Fig. 4.8(a-d), the excess current decays rapidly when the illumination is cut-off. The expanded view of one of these decay curves with the exponential decay fitting is shown in Fig. 4.9. The decay of excess current after turning the light off is similar to that reported for several semiconductor films. Often a much slower current decay followed by an initial sharp decay is observed [2, 20]. In some cases, the current does not return to its dark value and remains at a higher value even after a much longer time, termed persistent photoconductivity (PPC) [20].

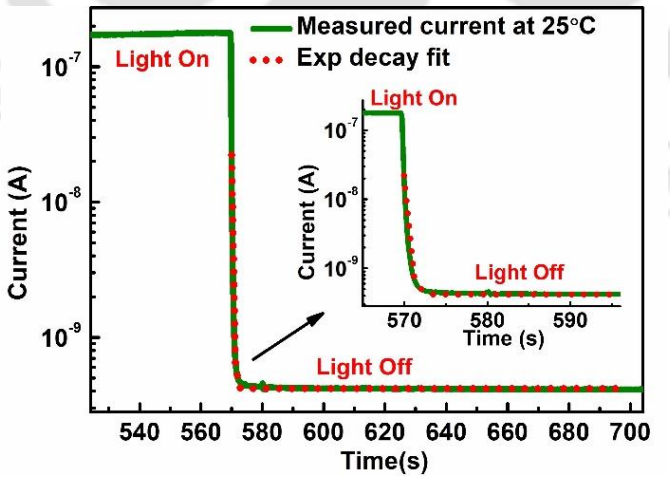

Figure 4.9: *Rapid transient current decay (solid line) of $MAPbI_3$ film after illumination is cut-off and the dotted line represents the exponential decay fit with Eq. 4.2. The figure inset shows the expanded view of the current decay curve region after illumination is stopped*

The initial sharp decay of current in these cases is attributed to the band to band recombination, followed by slow re-emission of charge carriers from traps and subsequent recombination. Therefore, to understand the nature of traps, the decay curves after the illumination is cut-off at varying intensity and temperature are further analyzed. The current decay curve could be best fitted using the exponential decay equation given in Eq. 4.2. The dark current decay time constants τ_{d1} and τ_{d2} values obtained by fitting current decay curves for different exposure times at full intensity illumination and at varying light intensity for different temperatures are listed in Table 4.2 and Table 4.3, respectively.

Table 4.2: *Dark current decay time constant values obtained by fitting current decay curves after different exposure time duration to full intensity (~1000 Wm^{-2}) at different temperatures*

Exposure Time	25 °C		50 °C		60 °C		70 °C	
	τ_{d1}(sec)	τ_{d2}(sec)	τ_{d1}(sec)	τ_{d2}(sec)	τ_{d1}(sec)	τ_{d2}(sec)	τ_{d1}(sec)	τ_{d2}(sec)
30sec	0.10±0.01	0.31±0.01	0.10±0.01	0.30±0.01	0.12±0.01	0.35±0.02	0.11±0.01	0.31±0.02
60sec	0.10±0.01	0.34±0.01	0.09±0.01	0.27±0.01	0.10±0.01	0.32±0.01	0.10±0.01	0.30±0.01
90sec	0.11±0.01	0.37±0.01	0.09±0.01	0.29±0.01	0.12±0.01	0.49±0.10	0.08±0.01	0.23±0.01

Table 4.3: *Dark current decay time constant values obtained by fitting current decay curves after 90 sec illumination at varying light intensity for different temperatures (25 -70 °C)*

Light intensity (Wm^{-2})	25 °C		50 °C		60 °C		70 °C	
	τ_{d1}(sec)	τ_{d2}(sec)	τ_{d1}(sec)	τ_{d2}(sec)	τ_{d1}(sec)	τ_{d2}(sec)	τ_{d1}(sec)	τ_{d2}(sec)
100	0.08±0.01	0.30±0.01	0.10±0.01	0.49±0.03	0.08±0.01	0.28±0.01	0.07±0.01	0.26±0.01
300	0.09±0.01	0.30±0.01	0.10±0.01	0.39±0.02	0.11±0.01	0.37±0.02	0.11±0.01	0.35±0.02
500	0.11±0.01	0.39±0.01	0.08±0.01	0.28±0.01	0.12±0.01	0.40±0.02	0.10±0.01	0.32±0.03
800	0.11±0.01	0.39±0.01	0.12±0.01	0.45±0.01	0.12±0.01	0.43±0.03	0.09±0.01	0.28±0.01
1000	0.11±0.01	0.37±0.01	0.09±0.01	0.29±0.01	0.12±0.01	0.49±0.10	0.08±0.01	0.23±0.01

The τ_{d1} is approximately 0.10 sec and τ_{d2} varies from 0.23 sec to 0.50 sec. There is not much variation in the decay constants values with variation in exposure time and illumination intensity, as the values lie within the error bars. The two different values of decay constants suggest that there are two different levels of the shallow defect. These values indicate that the trapped carriers are slowly re-emitted to the conduction band, and recombination occurs. The shallow defects were also detected in the PL peak analysis. It is found that for the measurement condition of 25 °C, intensity = 1000 Wm^{-2} illumination time = 60 sec, the decay constant values (τ_{d1}= 0.10 s and τ_{d2} = 0.34 s) are slightly larger than the one-step deposited perovskite film (τ_{d1} = 0.07 s and τ_{d2} = 0.25 s) discussed in chapter 3. Thus, the perovskite films prepared by the one-step method have a little shallower trap states than the two-step processed films. This is consistent with the PL spectra, where the low energy peak has smaller intensity than the high-intensity peak for the two-step.

In literature, a phase transition from tetragonal to the cubic structure between 327 K and 330 K (54-57 °C) is reported for $MAbI_3$ films [21]. During this phase change from tetragonal to cubic in $MAbI_3$ films, the extent of rotational freedom of the methylammonium cation changes and this factor has the potential to influence the charge-carrier dynamics and thus the efficiency of charge transport within the perovskite film [21]. However, we did not observe significant changes in the *I-t* characteristics through the phase-changing temperature point. These characteristics indicate that the $MAPbI_3$ perovskites are stable in the operating temperature range of 25-70 °C. Also, the $MAPbI_3$ film did not show any distinct PPC effect in *I-t* characteristics.

4.2.7.3 Study of the recombination process

The intensity dependence of photocurrent has been studied to know the nature of recombination processes. The stabilized photocurrent vs. intensity plots at different

temperatures are shown in Fig. 4.10. As shown in Fig. 4.10, the photocurrent rises with light intensity from 100 to 1000 Wm^{-2}. The stabilized current under illumination depends upon the steady-state carrier concentration, which in turn depends upon the generation rate (a function of illumination intensity) and the recombination rate (a function of trap density, free carrier density and recombination probability). Under illumination, some of the free carriers in the extended states are trapped by the defect states. However, the density of these trapped carriers is a fraction of the photogenerated carrier density. The increase of the steady-state photocurrent with the increases in temperature can be attributed to a reduction in the height of the potential barrier in the grain boundaries caused by the thermal excitation of electrons trapped in states of the grain boundaries [2].

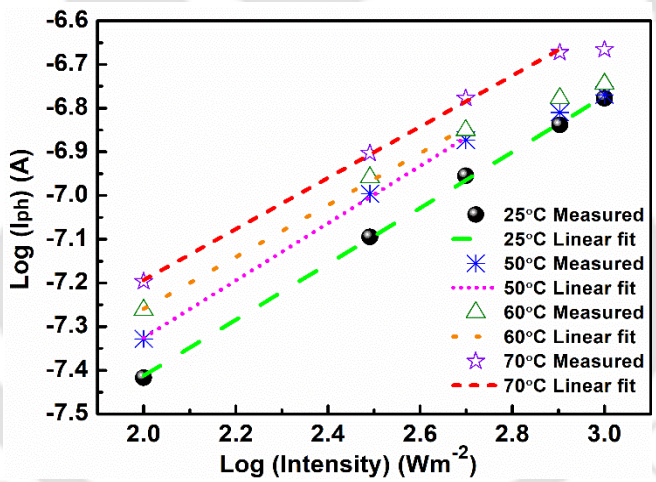

Figure 4.10: *Photocurrents (I_{ph}) of $MAPbI_3$ film at different illumination intensities and temperatures. The linear fit of the photocurrents at varying illumination intensities in a log scale plot determines the exponent value γ in Eq. 4.3*

The curves of log(I_{ph}) vs. log(Intensity) shown in Fig. 4.10 are straight lines, which indicates that the photocurrent follows a power law, as given in Eq. 4.3 below.

$$I_{ph} = \Phi^{\gamma} \tag{4.3}$$

Where I_{ph} is photocurrent, Φ is the light intensity and γ is the exponent.

The values of exponent γ obtained after fitting linear region of photocurrent curves (as shown in Fig. 4.10) are 0.64±0.01, 0.65±0.01, 0.59±0.02 and 0.58±0.01 at different temperatures; 25 °C, 50 °C, 60 °C and 70 °C respectively. The value of γ indicates that the recombination processes are predominantly bimolecular (electron-hole recombination) in nature and the rate of recombination does not change much with the temperature rise. It has also been reported that the bimolecular recombination rate does not change significantly with the change in phase [21]. A close inspection of the γ values indicates that γ~0.64 for T≤ 50 °C and γ~ 0.59 for T≥50 °C. This small change in the value of γ maybe due to the phase change in $MAPbI_3$ at around 54-57 °C [22]. Another reason for the small decrease in the value of the exponent γ could be due to a small decrease in the bimolecular recombination rate. This is because, with the increasing temperature, the interaction between the free carriers (electron and holes) and phonons increases and hence the charge carrier mobility decreases. Thus the probability of recombination of free electrons and holes decreases due to a decrease in mobility of electrons approaching to hole's Coulombic capture radius [21]. An increase in the monomolecular recombination rate with increasing temperature is also reported and is consistent with a charge recombination process assisted by ionized impurities [21]. The traps for either electrons or holes in $MAPbI_3$ may originate from various sources, including elemental vacancies, substitutions, or interstitials [17, 23].

4.2.7.4 Activation energy estimation

Figure 4.11 shows the dark current as a function of inverse temperature. The electrical transport measurements are done in a vacuum. The linear variation of log I_d with $10^3/T$ suggests that the current transport is thermally activated. The activation energy is estimated using the Arrhenius equation given in Eq. 4.4.

$$I_d = I_{do} exp(-E_a/kT) \quad (4.4)$$

Where I_d is the dark current, I_{do} is the pre-factor, E_a is the activation energy, k is the Boltzmann constant, T is the absolute temperature in Kelvin. The fitting yield activation energy of approximately 210 meV is close to the reported value [21]. The small value of activation energy suggests the electrical transport is via the trap states [23, 24].

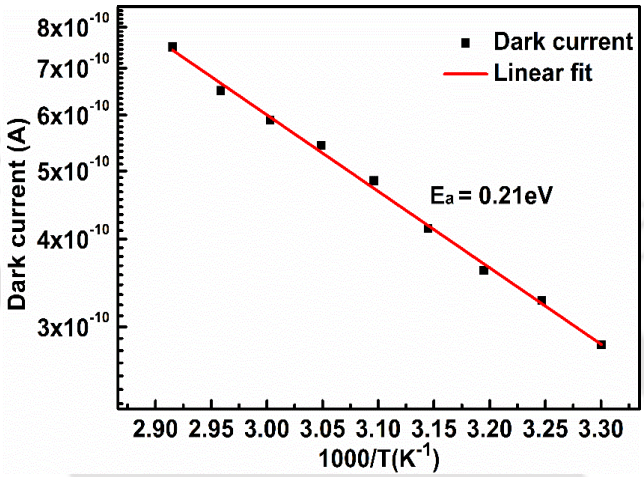

Figure 4.11: *Dark current of $MAPbI_3$ film as a function of temperature. The linear fit of the data points is done to estimate the activation energy using Eq. 4.4*

4.2.8 Stability test of the $MAPbI_3$ perovskite film

The primary issue of halide perovskite material is its degradation due to moisture. Instability in moisture is the major challenge for its practical application and commercialization. So, to check the stability of the perovskite film, current transient measurements at different temperatures were repeated on the same sample used for *I-t* measurements after storing it under a vacuum for 60 days. Fig. 4.12 shows the transient photocurrent of aged $MAPbI_3$ film for different exposure times to 1000 Wm^{-2} illumination at different temperatures.

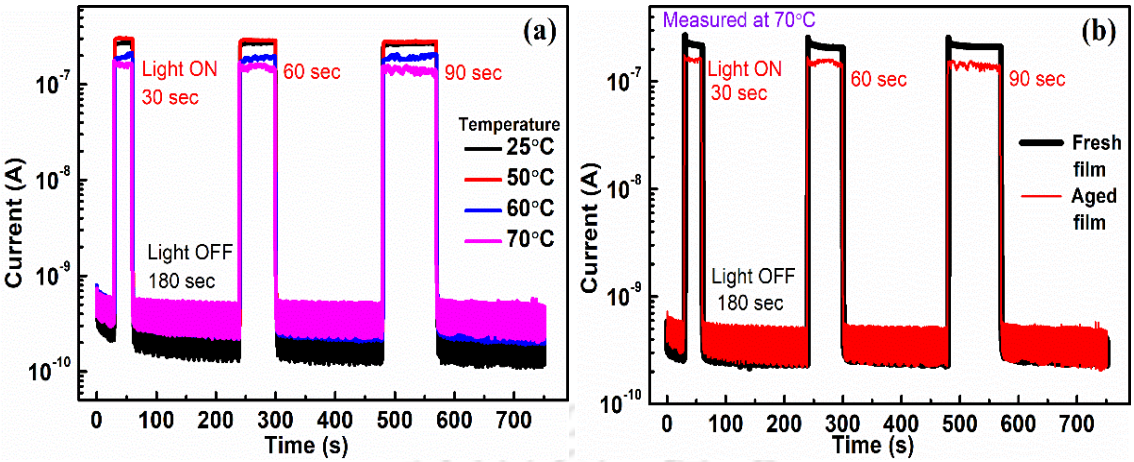

Figure 4.12: *(a) I-t characteristics of aged $MAPbI_3$ film for different exposure times to full intensity (1000 Wm^{-2}) illumination at different temperatures (b) I-t characteristics of fresh and aged $MAPbI_3$ film for different exposure times to full intensity (1000 Wm^{-2}) illumination at 70 °C*

Remarkably, the perovskite film has shown good photosensitivity [Fig. 4.12(a)], with stable transient current similar to the freshly deposited films. Fig. 4.12(b) shows that the *I-t* characteristics of fresh and aged $MAPbI_3$ are similar with almost the same photocurrent values, showing that TE+DC perovskite films have good stability for up to 60 days without significant changes in their optoelectronic properties. The decay constant values (after light off) listed in Table 4.4 confirm that the $MAPbI_3$ films have retained their initial property without significant changes in τ_{d1} and τ_{d2}.

Table 4.4: *Decay time constant values obtained by fitting current decay curves of aged $MAPbI_3$ film after 90 sec light exposure to full intensity (1000 Wm^{-2}) at different temperatures*

Temperat-ure	25 °C		50 °C		60 °C		70 °C	
decay time constants	τ_{d1}(sec)	τ_{d2}(sec)	τ_{d1}(sec)	τ_{d2}(sec)	τ_{d1}(sec)	τ_{d2}(sec)	τ_{d1}(sec)	τ_{d2}(sec)
	0.10±0.01	0.26±0.01	0.12±0.01	0.29±0.01	0.11±0.01	0.31±0.01	0.12±0.01	0.38±0.02

4.3 Conclusion

Highly stable $MAPbI_3$ perovskite thin films could be synthesized using the TE+DC two-step method. The TE+DC $MAPbI_3$ films are pinhole-free with large grain sizes, whereas

the SC+DC films have pinholes and small grain sizes. The $MAPbI_3$ films synthesized using vapor-deposited PbI_2 films showed better photoconductivity and stability than the spin-coated PbI_2 films. PbI_2 films deposited by thermal evaporation are more uniform and reproducible than spin coating films. Because a spin-coated film quality depends a lot on the solution dispensing process on the substrate, solution viscosity and temperature, thus, it is not easy to reproduce a similar quality of films by spin coating technique. Moreover, the material loss in the spin coating process is more compared to thermal evaporation. The dip-coating technique is an easy and quick method for making large-area films. The recombination nature of TE+DC films is almost similar in the temperature range of 25-70 °C, though the phase change of $MAPbI_3$ occurs at 54-57 °C. In adittion two-step deposited films are stable for up to 60 days when stored in a vacuum. Hence, the TE+DC method can be used for large-area solar cell fabrication because it provides better film qualities than spin-coating.

From the XRD analysis, it can be concluded that disadvantages with two-step process, such as the incomplete conversion of PbI_2 to $MAPbI_3$ and uncontrolled particle sizes of perovskite, can be overcome by the one-step process using additives for morphology control. Similar to the one-step deposited films [Chapter 3], the TE+DC films also have strong absorption in the visible region and show good photosensitivity in *I-t* measurements. The decay time constants show that the recombination nature is almost similar for both one-step and two-step films and they have shallow defect levels, as also identified from the PL measurement. In contrast to the one-step deposited films, the PL peak intensity of two-step film is more for the high energy peak compared to the low energy peak indicating that the defect density at a shallow level is much less in the films deposited by two-step TE+DC films.

4.4 References

1. Zheng, L., et al., *Morphology control of the perovskite films for efficient solar cells.* Dalton Transactions, 2015. **44**(23): p. 10582-10593.
2. Gordillo, G., C. Otálora, and A. Ramirez, *A study of trap and recombination centers in $MAPbI_3$ perovskites.* Physical Chemistry Chemical Physics, 2016. **18**(48): p. 32862-32867.
3. Zhou, Y., et al., *Growth control of compact $CH_3NH_3PbI_3$ thin films via enhanced solid-state precursor reaction for efficient planar perovskite solar cells.* Journal of Materials Chemistry A, 2015. **3**(17): p. 9249-9256.
4. Guo, X., et al., *Identification and characterization of the intermediate phase in hybrid organic–inorganic $MAPbI_3$ perovskite.* Dalton Transactions, 2016. **45**(9): p. 3806-3813.
5. Chiang, C.-H., Z.-L. Tseng, and C.-G. Wu, *Planar heterojunction perovskite/ $PC_{71}BM$ solar cells with enhanced open-circuit voltage via a (2/1)-step spin-coating process.* Journal of Materials Chemistry A, 2014. **2**(38): p. 15897-15903.
6. Thakur, U., et al., *Investigation into the advantages of pure perovskite film without PbI_2 for high performance solar cell.* Scientific reports, 2016. **6**: p. 35994.
7. Chen, J., et al., *Origin of the high performance of perovskite solar cells with large grains.* Applied Physics Letters, 2016. **108**(5): p. 053302.
8. Bi, C., et al., *Understanding the formation and evolution of interdiffusion grown organolead halide perovskite thin films by thermal annealing.* Journal of Materials Chemistry A, 2014. **2**(43): p. 18508-18514.
9. Eom, K., et al., *Depth-resolved band alignments of perovskite solar cells with significant interfacial effects.* Journal of Materials Chemistry A, 2017. **5**(6): p. 2563-2571.
10. Noh, J.H., et al., *Chemical management for colorful, efficient, and stable inorganic-organic hybrid nanostructured solar cells.* Nano Letters, 2013. **13**(4): p. 1764-9.
11. Asuo, I.M., et al., *Ambient condition-processing strategy for improved air-stability and efficiency in mixed-cation perovskite solar cells.* Materials Advances, 2020. **1**(6): p. 1866-1876.
12. Kong, W., et al., *Characterization of an abnormal photoluminescence behavior upon crystal-phase transition of perovskite $CH_3NH_3PbI_3$.* Physical Chemistry Chemical Physics, 2015. **17**(25): p. 16405-16411.
13. Hidayat, R., et al., *Revealing the charge carrier kinetics in perovskite solar cells affected by mesoscopic structures and defect states from simple transient photovoltage measurements.* Scientific Reports, 2020. **10**(1): p. 19197.
14. Chen, Y. and H. Zhou, *Defects chemistry in high-efficiency and stable perovskite solar cells.* Journal of Applied Physics, 2020. **128**(6): p. 060903.

15. Wang, F., et al., *Defects engineering for high-performance perovskite solar cells.* npj Flexible Electronics, 2018. **2**(1): p. 22.

16. Si, F., et al., *Effects of defect states on the performance of perovskite solar cells.* Journal of Semiconductors, 2016. **37**(7): p. 072003.

17. Kim, J., et al., *The Role of Intrinsic Defects in Methylammonium Lead Iodide Perovskite.* The Journal of Physical Chemistry Letters, 2014. **5**(8): p. 1312-1317.

18. Sadhukhan, P., et al., *Unraveling the Charge Transport Mechanism in Mechanochemically Processed Hybrid Perovskite Solar Cell.* Langmuir, 2021. **37**(18): p. 5513-5521.

19. Serfaty, A. and N. Joshi, *Fourier-transform analysis of multiexponential curves observed in photoconductivity studies.* Physical Review B, 1990. **41**(12): p. 8545.

20. Paul, G.S. and P. Agarwal, *Persistent photocurrent and decay studies in CdS nanorods thin films.* Journal of Applied Physics, 2009. **106**(10): p. 103705.

21. Milot, R.L., et al., *Temperature-Dependent Charge-Carrier Dynamics in $CH_3NH_3PbI_3$ Perovskite Thin Films.* Advanced Functional Materials, 2015. **25**(39): p. 6218-6227.

22. Baikie, T., et al., *Synthesis and crystal chemistry of the hybrid perovskite $(CH_3NH_3)PbI_3$ for solid-state sensitised solar cell applications.* Journal of Materials Chemistry A, 2013. **1**(18): p. 5628.

23. Yin, W.-J., T. Shi, and Y. Yan, *Unusual defect physics in $CH_3NH_3PbI_3$ perovskite solar cell absorber.* Applied Physics Letters, 2014. **104**(6): p. 063903.

24. Wu, X., et al., *Trap States in Lead Iodide Perovskites.* J Am Chem Soc, 2015. **137**(5): p. 2089-2096.

CHAPTER 5

Fabrication and characterization of (p-i-n) planar heterojunction $MAPbI_3$ based solar cells

This chapter presents the fabrication and characterization of inverted planar heterojunction (p-i-n) $MAPbI_3$ solar cells fabricated using one-step and two-step deposition methods for the perovskite absorber layer. The synthesis of $MAPbI_3$ perovskite thin films using one-step and two-step methods and their optoelectronic properties were already discussed in chapters 3 and 4. Following the optimized deposition method of $MAPbI_3$ perovskite, solar cells with the configuration of *FTO/PEDOT:PSS/$MAPbI_3$/PCBM/BCP/Ag* and *ITO/PEDOT:PSS/$MAPbI_3$/PCBM/ITO/Ag* were fabricated using the one-step and two-step methods, respectively. The absorber layer thickness has a vital role in solar cell performance; thus, PSC were fabricated at different absorber thicknesses using the one-step method. The influence of $MAPbI_3$ layer thickness variation on the solar cell's performance is discussed. A fast degradation was observed in the solar cells fabricated

using the two-step method with a typical device structure of *ITO/PEDOT:PSS/MAPbI$_3$/PCBM/Ag*. This degradation is due to ambient moisture and silver (Ag) diffusion into the PSC. The detrimental effects of Ag diffusion are discussed in earlier reports [1, 2]. Therefore, to prevent the fast diffusion of the silver electrode into the perovskite absorber layer, a thin layer of ITO (Indium tin oxide) was incorporated in between the electron transport layer (ETL) and Ag electrode, which modified the device configuration as *ITO/PEDOT:PSS/MAPbI$_3$/PCBM/ITO/Ag*. After adding the ITO interlayer, the device efficiency and stability improved significantly due to the inhibition of Ag diffusion into the perovskite device.

5.1 Experimental details

$MAPbI_3$-based solar cells of size 0.1 cm^2 were fabricated in p-i-n structure using the one-step and two-step deposition methods. The planar heterojunction solar cells with configuration *FTO/PEDOT:PSS/MAPbI$_3$/PCBM/BCP/Ag* were fabricated using the one-step method by varying the $MAPbI_3$ (absorber) layer thickness from 100 nm to 500 nm. In addition, the planar solar cells with the configuration of *ITO/PEDOT:PSS/MAPbI$_3$/PCBM/ITO/Ag* were fabricated by the two-step method using ITO interlayer for preventing Ag electrode diffusion. The schematics of the solar cell structures are shown in Fig. 5.1 (a-b). The energy band diagram of solar cell structures [Fig. 5.1 (a-b)] with the HOMO (highest occupied molecular orbital level) and LUMO (lowest unoccupied molecular orbital) levels of individual layers and the work function of the electrodes are shown in Fig. 5.1 (c-d). The PEDOT:PSS (Poly(2,3-dihydrothieno-1,4-dioxin)-poly(styrene sulfonate)) and PCBM ((6, 6)-phenyl C61-butyric acid methyl ester) layers acts as HTL and ETL respectively. The ITO (indium tin oxide)

interlayer deposited by RF sputtering and BCP (bathocuproine) by spin coating function as buffer layers between ETL and Ag [Fig 5.1(a-b)].

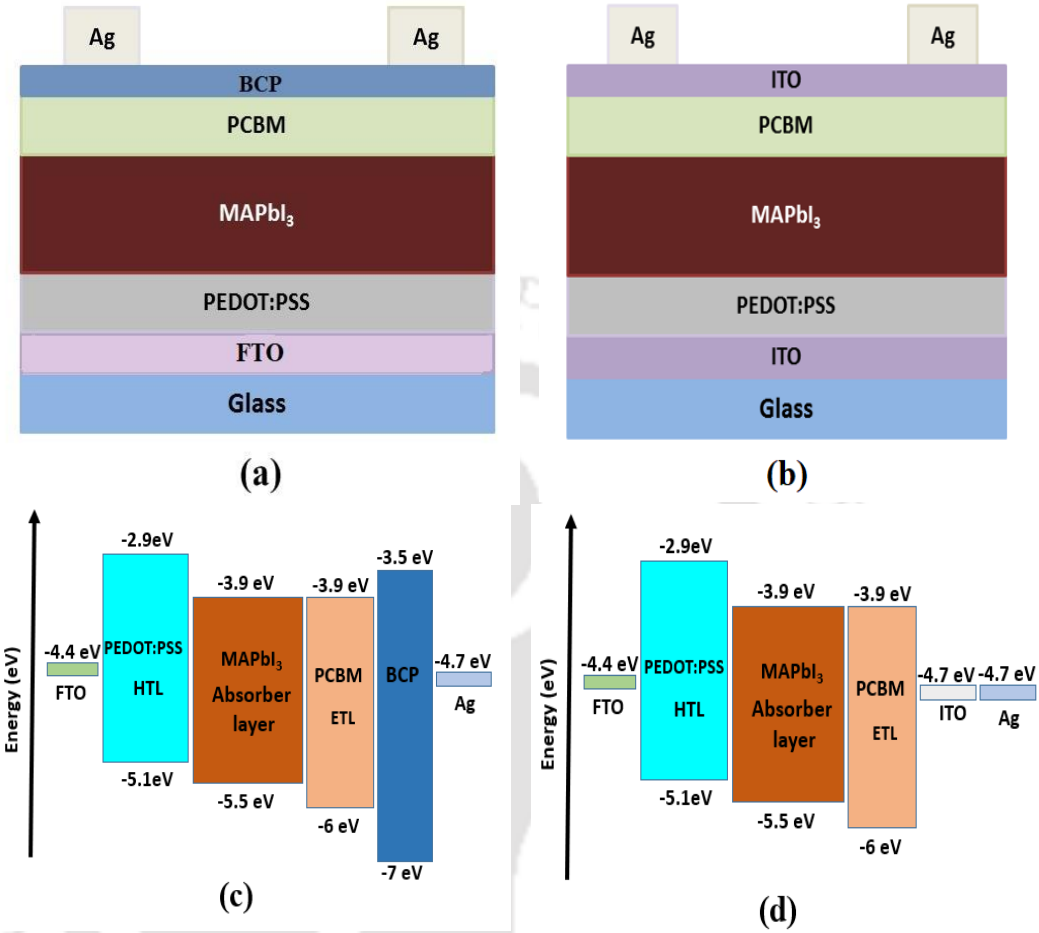

Figure 5.1: *Schematic of p-i-n planar $MAPbI_3$ perovskite solar cell structure fabricated using (a) one-step, and (b) two-step deposition methods, (c-d) Energy band diagram of solar cell structure (a) & (b) showing the individual HOMO and LUMO levels with the work function of the electrodes*

Details of solar cell fabrication are mentioned in section 2.3 of chapter 2. The *I-V* (current-voltage) measurements of solar cells were done using a Keithley 2450 source measurement unit (SMU) under incident power density of 100 $mWcm^{-2}$ using a Xenon lamp with AM1.5 conditions. The fabrication and characterization of the solar cells were carried out in an ambience with moderate relative *RH* of 40-50%. The device stability test was done by *I-V* measurement of the cells in the air (Avg. *RH* = 45%) at different time intervals for the devices stored in a vacuum desiccator.

5.2 Results and discussion

5.2.1 *J-V* characteristics of solar cells fabricated using one-step method

Fig. 5.2(a-b) shows the *J-V* (current density-voltage) characteristics and solar cell performance parameters with varying thickness of the $MAPbI_3$ layer. The J_{sc}, V_{oc}, *FF* and PCE values for all the cells estimated from the *J-V* curve are listed in Table 5.1. A systematic increase in the current density (J_{sc}) is observed with increasing absorber thickness from 100 nm to 400 nm. The J_{sc} increased from 2.24 $mAcm^{-2}$ (100 nm) to 8.53 $mAcm^{-2}$ (400 nm) due to an increase in the number of photon absorption with absorber thickness [3, 4]. A moderate increase in open-circuit voltage (V_{oc}) is also observed with thickness and the highest V_{oc} of 0.96 V is achieved at 400 nm. However, J_{sc} and V_{oc} slightly decreased as the thickness was further increased to 500 nm. This is because the thick absorber layer beyond optimal thickness adds series resistance, due to which J_{sc} starts decreasing. In addition to that, the charge carrier collection at the respective electrodes decreases due to the longer transfer path and the subsequent carrier recombination reduces the V_{oc} [5]. Similarly, power conversion efficiency (PCE) reached the highest value at 400 nm due to increased J_{sc}, V_{oc} and *FF* values. The cells showed the best PCE of ~5% at the absorber thickness of 400 nm, with J_{sc} = 8.53 $mAcm^{-2}$, V_{oc} = 0.96 V and *FF* = 0.6. At a higher thickness of 500 nm, the PCE decreased to 4.47% due to lower J_{sc} and V_{oc}. These efficiencies are lower than the reported values because the cell performance was affected by moisture in the ambience during fabrication and characterization. Moreover, it has been known that single cation perovskites like $MAPbI_3$ are less stable than double or triple cation perovskites [6, 7]. Despite numerous challenges in handling $MAPbI_3$ perovskite in high humidity ambience, we could achieve an efficiency of 5%. It is expected that further optimization in the device by improving the perovskite

film quality, reducing interfacial defects, and fabrication in a humidity-controlled ambience will definitely improve the performance.

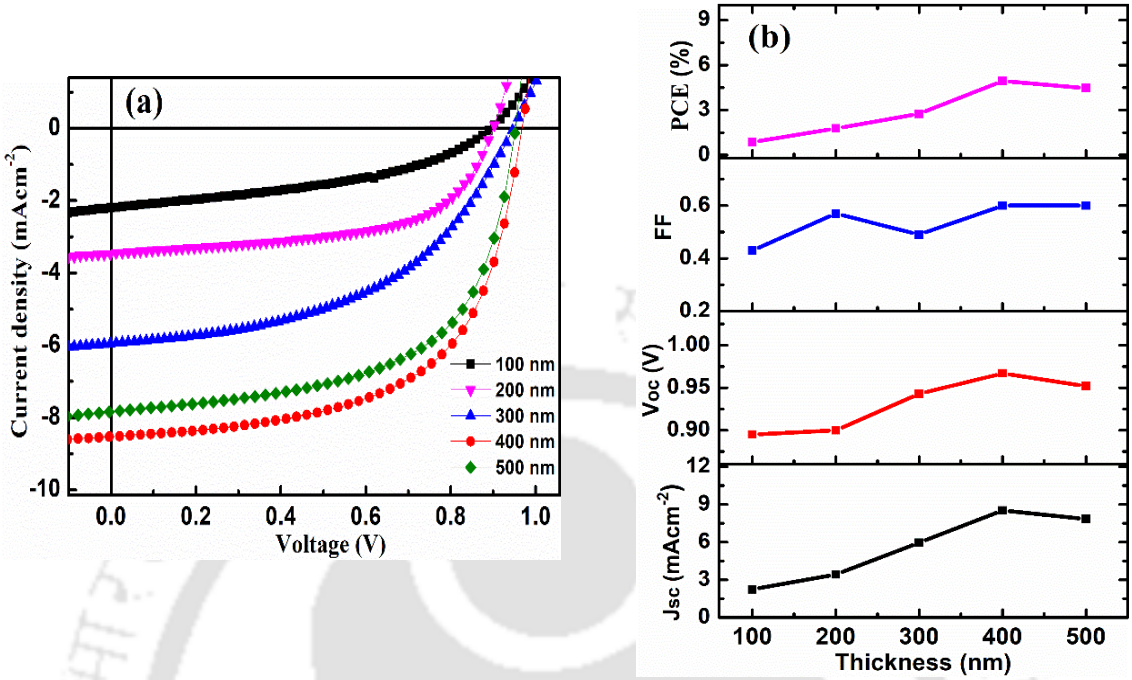

Figure 5.2: *(a) J-V characteristics of $MAPbI_3$ PSC at varying absorber thickness from 100 nm to 500 nm (b) solar cell performance with respect to absorber layer thickness variation*

Table 5.1: *Solar cell performance parameters of $MAPbI_3$ PSC with absorber thickness variation*

Thickness (nm)	J_{sc} (mAcm^{-2})	V_{oc} (V)	*FF*	η(%)
100	2.24	0.89	0.43	0.87
200	3.43	0.90	0.57	1.78
300	5.96	0.94	0.49	2.76
400	8.53	0.96	0.60	4.94
500	7.84	0.95	0.60	4.47

The device stability test of the best performing solar cell (absorber thickness of 400 nm) was performed for 400 hrs by *I-V* measurement of the solar cell in the air (avg. *RH* ~ 45%) at a regular time interval. Fig. 5.3(a-b) shows the *J-V* characteristics and corresponding changes in cell performance parameters with the aging time. The J_{sc} , V_{oc} , *FF* and *PCE* values during aging at different time intervals are listed in Table 5.2.

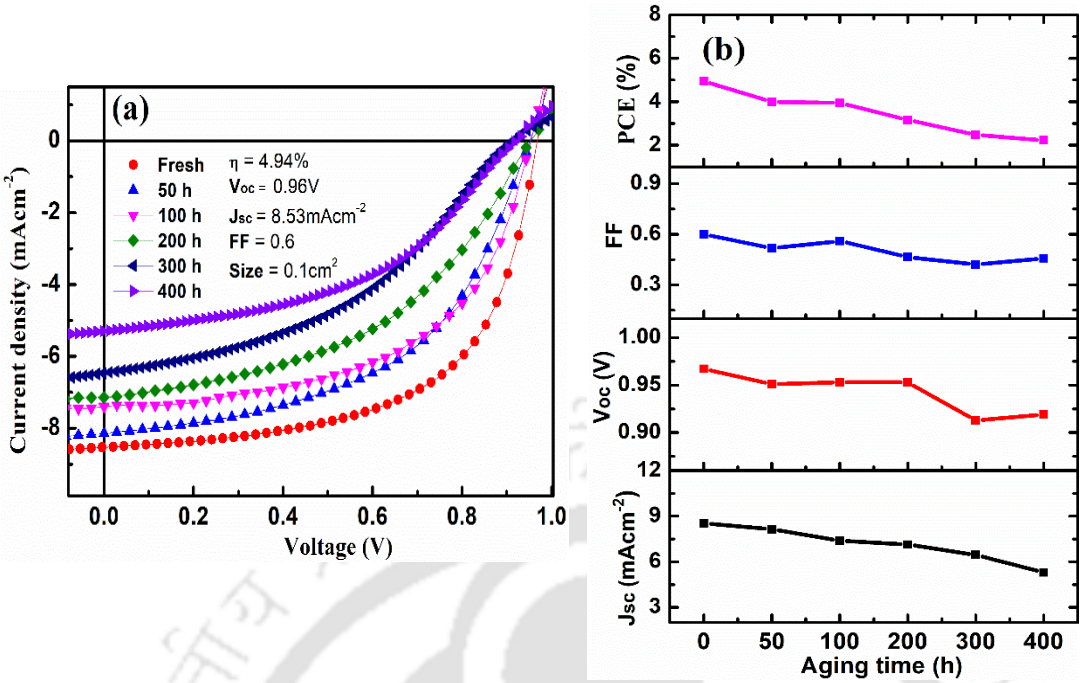

Figure 5.3: *Stability test of $MAPbI_3$ PSC in the air with avg. RH of ~ 45% (a) J-V characteristics and (b) performance of $MAPbI_3$ PSC during aging at different time intervals*

Table 5.2: *Variation in solar cell performance parameters of $MAPbI_3$ PSC with aging*

Aging time (h)	J_{sc} (mAcm^{-2})	V_{oc} (V)	*FF*	η(%)
0	8.53	0.96	0.6	4.94
50	8.13	0.95	0.51	4.00
100	7.39	0.95	0.56	3.94
200	7.13	0.95	0.46	3.16
300	6.45	0.91	0.42	2.48
400	5.29	0.91	0.45	2.22

The deposited fresh device shows a good *J-V* curve; however, the performance degraded slowly with time in the course of aging. The fast deterioration of J_{sc} and *FF* due to the decomposition of $MAPbI_3$ in moisture reduces the PCE [8]. Not much change is observed in the V_{oc} for the first 200 hrs; after that, the V_{oc} decreased slightly and the device exhibited s-shaped *J-V* curve. This is observed due to the degradation of perovskite and defect formation in the perovskite layer after 200 hrs. As observed from the *J-V* curve, the series resistance increases and shunt resistance decreases with perovskite degradation and thus, the cell efficiency reduces to 2.14% after 400 hrs. Eventually, the change of cell

appearance from dark brown to pale yellow indicated the degradation of the $MAPbI_3$ perovskite layer. As the performance degradation is primarily due to degradation of the $MAPbI_3$ layer in the moisture, proper encapsulation of the device is expected to improve the stability [9].

5.2.2 *J-V* characteristics of solar cells fabricated using two-step method

Fig. 5.4(a) shows the *J-V* characteristics of the p-i-n planar PSC (*ITO/PEDOT:PSS/$MAPbI_3$/PCBM/Ag*) fabricated using the two-step method. The device showed the highest J_{sc} of 5.43 $mAcm^{-2}$ and V_{oc} = 0.65 V, *FF* = 0.31, and PCE = 1.08 %. The device performance was low due to the fast degradation of the device due to moisture. Especially fast corrosion of the silver electrode in the device was observed, which affected the cell performance. As reported in the literature, the metal (Ag) electrode diffusion into the perovskite absorber layer in PSC is another potential cause of degradation [1, 10]. Due to Ag diffusion, the halide(I) in perovskite material reacts with Ag and forms silver iodide (AgI); thus, dissociation of $MAPbI_3$ occurs, which ultimately degrades the intrinsic properties of perovskite [11]. In addition, the corrosion of Ag electrodes in halide perovskites accelerates due to humidity which severely affects the device's performance [1]. Thus, the obtained low J_{sc}, V_{oc} and *PCE* are also due to perovskite degradation and shunting in the device.

In order to reduce the Ag diffusion into the perovskite layer, a thin conductive barrier layer of ITO was used. The thin ITO layer of thickness ~ 40 nm was added between the PCBM and Ag electrode, making the device configuration as *ITO/PEDOT:PSS/$MAPbI_3$/PCBM/ITO/Ag*. The ITO has the same work function as Ag (4.7 eV) [Fig 5.1 (d)], so the electrons can easily flow from PCBM to Ag electrode. Fig. 5.4(b) shows the *J-V* characteristics of the cell with an ITO interlayer. After adding the ITO

interlayer, the V_{oc}, J_{sc} and *FF* improved significantly. Thus, the new device showed an improved V_{oc} of 0.86 V, J_{sc} = 19.11 mAcm^{-2} and *FF* = 0.49; hence, the PCE also enhanced from 1% to 8.08%. Remarkably the overall performance enhanced significantly compared to the devices without ITO and fast diffusion of Ag was not visible. This improvement in device performance can be attributed to the role of the stable ITO interlayer in preventing the diffusion of Ag electrodes into the perovskite layer, which is detrimental to the device [12]. Thus, a thin ITO layer functioned as a suitable buffer layer between ETL and the Ag electrode. The short-circuit current density is close to the reported values [13]. However, V_{oc} and *FF* need further improvement to match the reported results [14]. The low V_{oc} and *FF* could be due to defects formed at the interfaces and the different layers during the fabrication process. In addition, the moisture effect during the measurement in ambient has also affected the cell performance as the devices were not encapsulated.

The *J-V* characteristics of the solar cell stability performance test at different time intervals are also shown in Fig. 5.4(a-b). The estimated solar cell parameters values from the *J-V* characteristics are listed in Table 5.3. It is seen that for the cells without ITO, the J_{sc} and V_{oc} degraded quickly, and the cell efficiency declined to 0.15% just within 100 hrs. Remarkably, the degradation rate is comparatively slower in the cells with an ITO interlayer. This is because the ITO interlayer between PCBM and Ag prevented the Ag diffusion and protected the device from fast degradation.

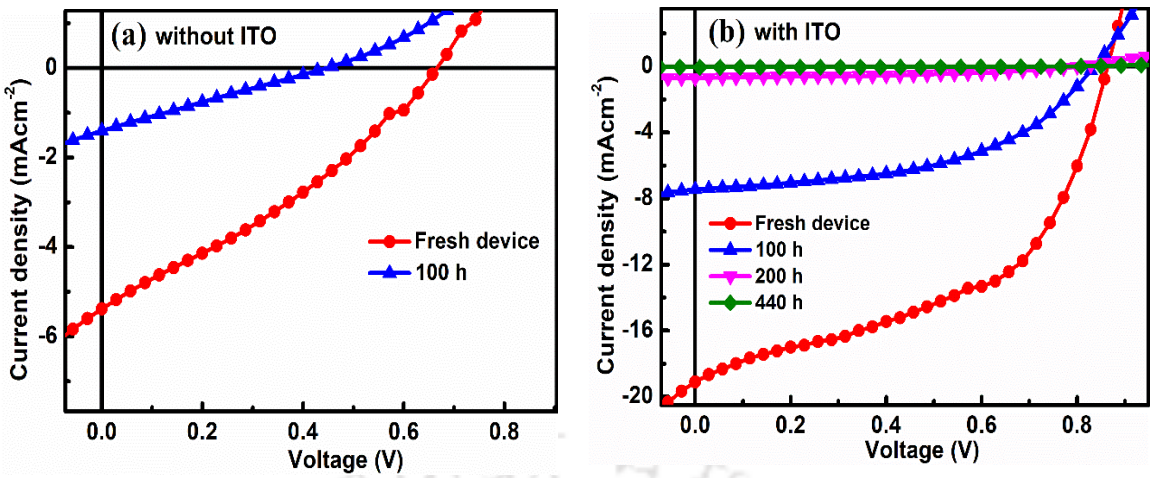

Figure 5.4: *J-V characteristics of $MAPbI_3$ based PSC without and with ITO interlayer, (a) ITO/PEDOT:PSS/$MAPbI_3$/PCBM/Ag and (b) ITO/PEDOT:PSS/$MAPbI_3$/PCBM/ITO/Ag. The J-V curves of the stability test at different time intervals are also shown in the figure*

Table 5.3: *Solar cell performance parameters of $MAPbI_3$ PSC without and with ITO interlayer during aging*

PSC structure	Aging time	J_{sc} (mAcm^{-2})	V_{oc} (V)	*FF*	η(%)
(a) Without ITO	Fresh device	5.43	0.65	0.31	1.08
	100 hrs	1.38	0.44	0.25	0.15
(b) With ITO	Fresh device	19.11	0.86	0.49	8.08
	100 hrs	7.51	0.83	0.48	3.00
	200 hrs	0.71	0.80	0.42	0.23
	440 hrs	0.05	0.79	0.42	0.01

As the perovskite absorber layer starts degrading, it loses the ideal optical and electrical properties, and hence the cell performance degrades [15]. The decrease in the J_{sc} directly indicates the degradation of the $MAPbI_3$ perovskite layer, corresponding to a decline in photon absorption during the decomposition process. The $MAPbI_3$ degradation in high *RH* was well demonstrated by Yang et al. using in situ UV-vis absorbance measurements during the decomposition process [16]. It has been found that the high-energy absorption feature below 500 nm rapidly declines at high *RH* = 98%; however, at lower *RH*, the decomposition was relatively slow. The decrease in J_{sc} and *FF* while aging is the cause of the fast decrease of PCE after 100 hrs. The PCE decreased to ~3% after 100 hrs. However, the V_{oc} remains stable with a slight decrease of ~70 mV even after 440 hrs. The device

with ITO survived longer than the device without ITO due to the effective reduction of the Ag electrode diffusion, which enhances both the efficiency and lifetime of the device. The efficiency of the devices can be further improved by proper encapsulation to minimize the detrimental effect of moisture in the ambience.

5.3 Conclusion

Planar heterojunction $MAPbI_3$ perovskite solar cells were fabricated using one-step and two-step methods in high humidity conditions. In the one-step deposited PSC, the best PCE of ~5% was achieved for absorber thickness of 400 nm and it could retain 40% (PCE = 2.14%) of the initial cell efficiency after 400 hrs. Initially, the performance of the two-step deposited PSC degraded quickly due to the detrimental effect of Ag electrode corrosion. Remarkably, the incorporation of the ITO interlayer improved the performance and stability of the device significantly. The thin ITO film on ETL acted as a suitable interlayer that inhibits the diffusion of the Ag electrode into the perovskite layer through PCBM. The addition of an intermediate ITO layer significantly improved the PCE from 1% to 8%, with improved V_{oc}, J_{sc} and *FF*. Thus, the ITO is a suitable material for preventing Ag diffusion and protecting the device from moisture to some extent. Despite high relative humidity during the fabrication process and measurements, we could achieve cell efficiency of ~8%. Therefore, the cell efficiency can be further improved by fabricating the devices in well-controlled humidity conditions and further optimizing the different layers in the device to minimize the defects causing losses in the devices.

5.4 References

1. Li, H., et al., *Corrosive Behavior of Silver Electrode in Inverted Perovskite Solar Cells Based on Cu:NiO_x*. IEEE Journal of Photovoltaics, 2019. **9**(4): p. 1081-1085.
2. Basumatary, P. and P. Agarwal, *A short review on progress in perovskite solar cells.* Materials Research Bulletin, 2022. **149**: p. 111700.
3. Dixit, H., D. Punetha, and S.K. Pandey, *Improvement in performance of lead free inverted perovskite solar cell by optimization of solar parameters.* Optik, 2019. **179**: p. 969-976.
4. Kumar, R.R., S.K.J.S. Pandey, and Microstructures, *Performance evaluation and material parameter perspective of eco-friendly highly efficient $CsSnGeI_3$ perovskite solar cell.* Superlattices and Microstructures, 2019. **135**: p. 106273.
5. Kanoun, A.-A., et al., *Toward development of high-performance perovskite solar cells based on $CH_3NH_3GeI_3$ using computational approach.* Solar Energy, 2019. **182**: p. 237-244.
6. Deng, Y., et al., *Air-stable, efficient mixed-cation perovskite solar cells with Cu electrode by scalable fabrication of active layer.* Advanced Energy Materials, 2016. **6**(11): p. 1600372.
7. Xu, F., et al., *Mixed cation hybrid lead halide perovskites with enhanced performance and stability.* J. Mater. Chem. A, 2017. **5**(23): p. 11450-11461.
8. Wang, R., et al., *A review of perovskites solar cell stability.* Advanced Functional Materials, 2019. **29**(47): p. 1808843.
9. Li, J., et al., *Encapsulation of perovskite solar cells for enhanced stability: Structures, materials and characterization.* Journal of Power Sources, 2021. **485**: p. 229313.
10. Leijtens, T., et al., *Overcoming ultraviolet light instability of sensitized TiO_2 with meso-superstructured organometal tri-halide perovskite solar cells.* Nature Communications, 2013. **4**(1): p. 1-8.
11. Kato, Y., et al., *Silver Iodide Formation in Methyl Ammonium Lead Iodide Perovskite Solar Cells with Silver Top Electrodes.* Advanced Materials Interfaces, 2015. **2**(13): p. 1500195.
12. Basumatary, P., J. Kumari, and P. Agarwal. *Enhancing the performance and stability of $MAPbI_3$ perovskite solar cells by inserting the ITO layer before the Ag electrode*. in *AIP Conference Proceedings*. 2021. AIP Publishing LLC.
13. Wu, H.-T., et al., *Improving Two-Step Prepared $CH_3NH_3PbI_3$ Perovskite Solar Cells by Co-Doping Potassium Halide and Water in PbI_2 Layer.* Nanomaterials, 2019. **9**(5): p. 666.
14. Heo, J.H., et al., *Hysteresis-less inverted $CH_3NH_3PbI_3$ planar perovskite hybrid solar cells with 18.1% power conversion efficiency.* Energy & Environmental Science, 2015. **8**(5): p. 1602-1608.

15. Basumatary, P. and P. Agarwal, *Two-step fabrication of $MAPbI_3$ perovskite thin films with improved stability.* Bulletin of Materials Science, 2019. **42**(6): p. 268.

16. Yang, J., et al., *Investigation of $CH_3NH_3PbI_3$ Degradation Rates and Mechanisms in Controlled Humidity Environments Using in Situ Techniques.* ACS Nano, 2015. **9**(2): p. 1955-1963.

CHAPTER 6

Optimization of absorber layer parameters for $MAPbI_3$ perovskite solar cells using Sentaurus-TCAD software

This chapter presents the simulation results of $MAPbI_3$ ($CH_3NH_3PbI_3$) perovskite-based solar cells performed using Sentaurus-TCAD software. In this simulation tool, all the electrical simulations are performed using the drift-diffusion transport model, in which the electrostatic Poisson equation and carrier continuity equation for electron and hole are solved iteratively [1]. As discussed earlier, $MAPbI_3$ perovskite has several excellent properties for photovoltaic applications, such as suitable bandgap, high crystallinity, and low-temperature processability [2, 3]. Despite the significant progress of perovskite solar cells (PSC) with high efficiencies, a detailed analysis is needed to understand the critical factors limiting the performance of PSC in depth. In this aspect, the numerical simulation of solar cells gives better insight into these critical factors influencing device performance. In solar cells, the generation and recombination of photogenerated carriers mainly occur

in the absorber layer; thus, the quality of the absorber layer has a significant role in the device's performance [4]. The density of defects is another crucial parameter determining the electrical characteristics of solar cells [5]. So, understanding the impact of defects on the performance of the device is essential in achieving high efficiency. In reality, the defects form due to several factors such as experimental conditions, solvent ratios, and precursor impurities that limit the formation of high-quality pinhole-free perovskite films with superior crystallinity [6, 7]. Likewise, the absorber layer thickness also plays an essential role in the device performance because the photon absorption depends on the absorber (perovskite) thickness [8]. Thus, finding the optimum absorber layer thickness is essential for achieving the best device output.

With this motivation, this simulation study has been carried out to present possible optimization routes for efficiency enhancements of $MAPbI_3$ solar cells by optimizing various parameters such as defect density in the absorber layer, the density of interface defects, and thickness of the perovskite absorber layer. The influence of these parameters on device performance has been discussed in this chapter.

6.1 Simulation details of n-i-p and p-i-n structure $MAPbI_3$ based PSC

The simulation studies were carried out for n-i-p (*FTO/SnO_2/$MAPbI_3$/Spiro-OMeTAD/Ag*) and p-i-n (*FTO/PEDOT:PSS/$MAPbI_3$/PCBM/Ag*) planar configurations of $MAPbI_3$ based PSC under standard conditions of AM 1.5 solar spectrum at room temperature (300 K). The schematics of two different device configurations are shown in Fig. 6.1 (a-b). Planar structures are usually used for device fabrication to avoid a mesoporous scaffold layer and improve reproducibility. Especially these structures are compatible with flexible substrates because the device layers can be processed at low temperatures or replaced with organic layers. Organic charge transport layers have been widely used in planar structures due to

their simple fabrication methods, decreased hysteresis effects, and enhanced device performance [9]. Practically a PSC structure (n-i-p or p-i-n) depends on the choice of suitable charge transport layers and the constraints in using them following a correct sequence of device fabrication steps to avoid adverse effects on the perovskite layer.

For the n-i-p configuration shown in Fig. 6.1 (a), FTO acts as front contact, SnO_2 as ETL, $MAPbI_3$ ($CH_3NH_3PbI_3$) is the absorber layer, spiro-OMeTAD is HTL, and Ag is the metal back contact. SnO_2 is used as ETL because it has several advantages, such as higher mobility, wider bandgap, superior optical transmittance and better stability than widely used TiO_2 ETL [10-13]. Figure 6.1 (b) shows the p-i-n configuration of the PSC, where PEDOT:PSS (Poly(2,3-dihydrothieno-1,4-dioxin)-poly(styrene sulfonate) and PCBM ([6,6]-phenyl-C_{61}-butyric acid methyl ester) act as HTL and ETL respectively and the other layers are the same as specified for the n-i-p configuration. In the n-i-p structure, the light is shone through SnO_2 (ETL) and in the p-i-n structure, light is shone through PEDOT:PSS (ETL).

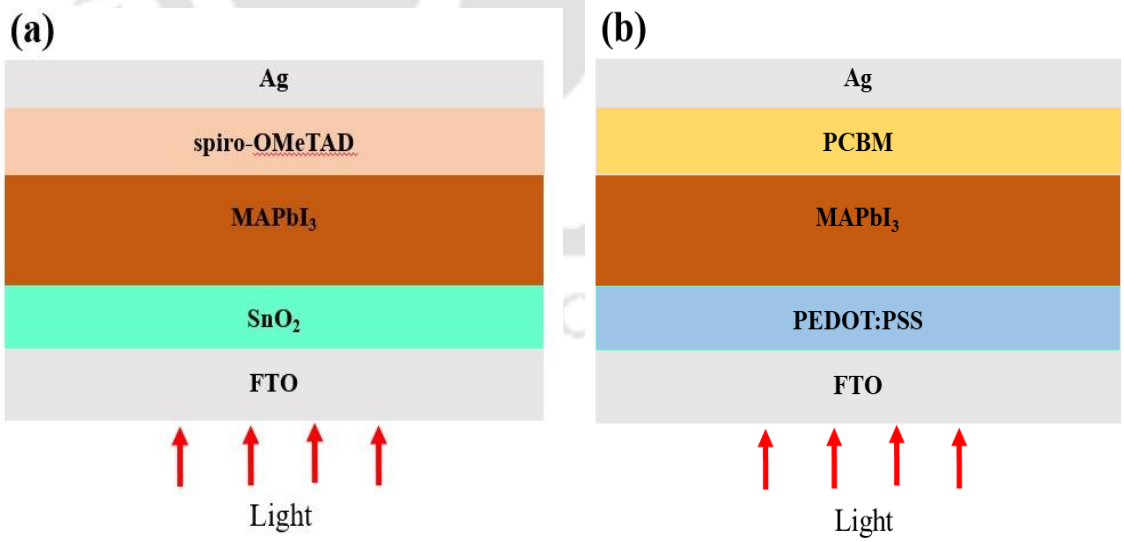

Figure 6.1: *Schematic of the PSC structures used for simulation (a) n-i-p structure FTO/SnO_2/$MAPbI_3$/Spiro-OMeTAD/Ag and (b) p-i-n structure FTO/PEDOT:PSS/$MAPbI_3$/PCBM/Ag*

Through this simulation, the influence of varying bulk defect density, interface defects, and thickness of the perovskite absorber layer on the device performance is studied. In the first series of simulations, the bulk defect density in the absorber layer is varied from 1×10^{14} to 1×10^{19} cm^{-3} for a fixed absorber thickness of 400 nm and interface defect density of 1×10^{6} cm^{-2}. In the next series, the optimal bulk defect density obtained from the first series of simulations is used for studying the role of the varying interface (ETL/$MAPbI_3$ & $MAPbI_3$/HTL) defect density from 1×10^{6} cm^{-2} to 1×10^{12} cm^{-2} at the fixed absorber layer thickness of 400 nm. Finally, the optimum defect (bulk & interface) density values are used to determine the optimum thickness for achieving the best PCE by varying the absorber layer thickness from 200 nm to 1000 nm. The specified bulk and interface defect densities used in this simulation study are within the reported range for $MAPbI_3$ perovskite and are well-considered for simulation studies [15, 16]. The measured complex refractive index (n and k) [using Spectroscopic Ellipsometry] of $MAPbI_3$ thin film synthesized in our lab is used in the simulation. The absorption coefficient (α) of $MAPbI_3$ is calculated from the extinction coefficient (k) using the relation, $\alpha = 4\pi k/\lambda$. The parameter values of different layers are taken from previously reported optimal experimental results and theoretical works [1, 12, 14]. The values of the different parameters and defect properties used in the simulation are listed in Table 6.1 and Table 6.2.

Table 6.1: *Parameters of different layers used in the simulation of $MAPbI_3$ based PSC*

Parameters	FTO	SnO_2	PCBM	$MAPbI_3$	Spiro-OMeTAD	PEDOT:PSS
Thickness (nm)	150	30	200	200-1000*	200	50
Acceptor density, $N_A(cm^{-3})$	-	-	-	1×10^{13}	1×10^{18}	1×10^{19}
Donor density, $N_D(cm^{-3})$	2×10^{19}	1×10^{17}	1×10^{19}	-	-	-
Bandgap energy, E_g (eV)	3.5	3.6	2.1	1.6	3	2.2
Electron affinity, χ (eV)	4.5	4.4	3.9	3.9	2.45	2.9
Relative dielectric permittivity, ε_r	9	9	3.9	30	3	3
Effective conduction band density, N_c (cm^{-3})	2.2×10^{18}	4.36×10^{18}	2.20×10^{17}	2.5×10^{20}	2.5×10^{20}	2.2×10^{15}
Effective valence band density, N_v (cm^{-3})	1.8×10^{19}	2.52×10^{19}	2.20×10^{16}	2.5×10^{20}	2.5×10^{20}	1.8×10^{18}
Mobility of electron, μ_n ($cm^2V^{-1}s^{-1}$)	20	240	1×10^{-3}	50	2×10^{-4}	1×10^{-2}
Mobility of hole, μ_p ($cm^2V^{-1}s^{-1}$)	20	25	2×10^{-3}	50	2×10^{-4}	2×10^{-4}
Lifetime of electron, τ_n (s)	1×10^{-9}	2.83×10^{-2}	1×10^{-9}	1×10^{-6}	1×10^{-7}	1×10^{-9}
Lifetime of hole, τ_p (s)	1×10^{-9}	2.83×10^{-2}	1×10^{-9}	1×10^{-6}	1×10^{-7}	1×10^{-9}
References	[1]	[12]	[14]	[12]	[12]	[14]

* Absorber layer thickness is kept 400 nm for bulk and interface defect density variation simulations; it is varied from 200 nm to 1000 nm when thickness variation is studied.

Table 6.2: *Defect parameters used in the simulation of $MAPbI_3$ based PSC*

Parameters	Bulk trap distribution	Interface trap distribution
Defect type	Neutral	Donor (ETL/$MAPbI_3$) Acceptor ($MAPbI_3$/HTL)
Capture cross section for electrons (cm^2)	1×10^{-15}	1×10^{-15}
Capture cross section for holes (cm^2)	1×10^{-15}	1×10^{-15}
Energetic distribution	Gaussian	Gaussian
Reference for defect energy level	Below Ec	Below Ec
Energy level with respect to Reference (eV)	0.8	0.8
Defect density (varied)	1×10^{14}-1×10^{19} cm^{-3} *	1×10^{6}-1×10^{12} cm^{-2} **

* Bulk defect density is kept constant at 1×10^{14} cm^{-3} for interface defect density and absorber layer thickness variation simulations. ** The interface layer is 10 nm thick for both interfaces and the defects are varied in the same intervals at both the interfaces simultaneously. Interface defect density is kept constant at 1×10^{6} cm^{-2} for bulk defect density variation and 1×10^{7} cm^{-2} for absorber layer thickness variation simulations. Ec - conduction band energy (eV).

In the defect model, a neutral defect type with Gaussian distribution is chosen from the midgap region at 0.8 eV below *Ec*. It has been considered as a perfect method to understand the effect of defect densities of the absorber layer because many defect energy levels are present in the halide perovskite [17]. Yin et al. explained the defect physics in $MAPbI_3$ perovskite corresponding to different defect levels [18]. Defects facilitate the excess carrier recombination, thus decreasing their lifetime. As a consequence, the diffusion

length also decreases. The relationship between diffusion length, carrier mobility, and lifetime is given in Eq. 6.1 [1].

$$L = \sqrt{\mu \frac{kT}{q} \tau} \tag{6.1}$$

where L is diffusion length, μ is electron/hole mobility, kT/q is thermal voltage and τ is carrier lifetime.

The relationship between carrier lifetime and trap densities is given in Eq. 6.2.

$$\tau = \frac{1}{N_t \sigma V_{th}} \tag{6.2}$$

Where N_t is trap density, σ is capture cross-section, V_{th} is the thermal velocity (10^7 cms^{-1}).

6.2 Results and discussion

6.2.1 Simulation results of *FTO/SnO₂/MAPbI₃/Spiro-OMeTAD/Ag* (n-i-p) solar cells

6.2.1.1 Influence of bulk defect density on solar cell performance

In this series of simulations, the effect of defect density in the perovskite (absorber) layer is analyzed by varying the defect density from 1×10^{14} to 1×10^{19} cm^{-3} while keeping the other parameters constant as given in Table 6.1 and 6.2. Fig. 6.2(a). shows the *J-V* characteristics of the PSC (*FTO/SnO₂/MAPbI₃/Spiro-OMeTAD/Ag*) at varying bulk defect densities at a constant interface defect density of 1×10^{6} cm^{-2}. The variations in solar cell performance parameters J_{sc}, V_{oc}, *FF* and *PCE* at different defect densities are shown in Fig. 6.2(b). The *J-V* characteristics show that as the defect density is increased above 10^{15} cm^{-3}, the cell performance starts deteriorating. Especially the V_{oc}, *FF* and *PCE* values start deteriorating considerably with the rise in defect density, while J_{sc} remains less affected initially and then decreases eventually at higher defect density. In this simulation series, the highest PCE of 23.72% was obtained at the defect density of 1×10^{14} cm^{-3}, with V_{oc} of 1.22 V, J_{sc} of 23.33 $mAcm^{-2}$ and *FF* of 0.83.

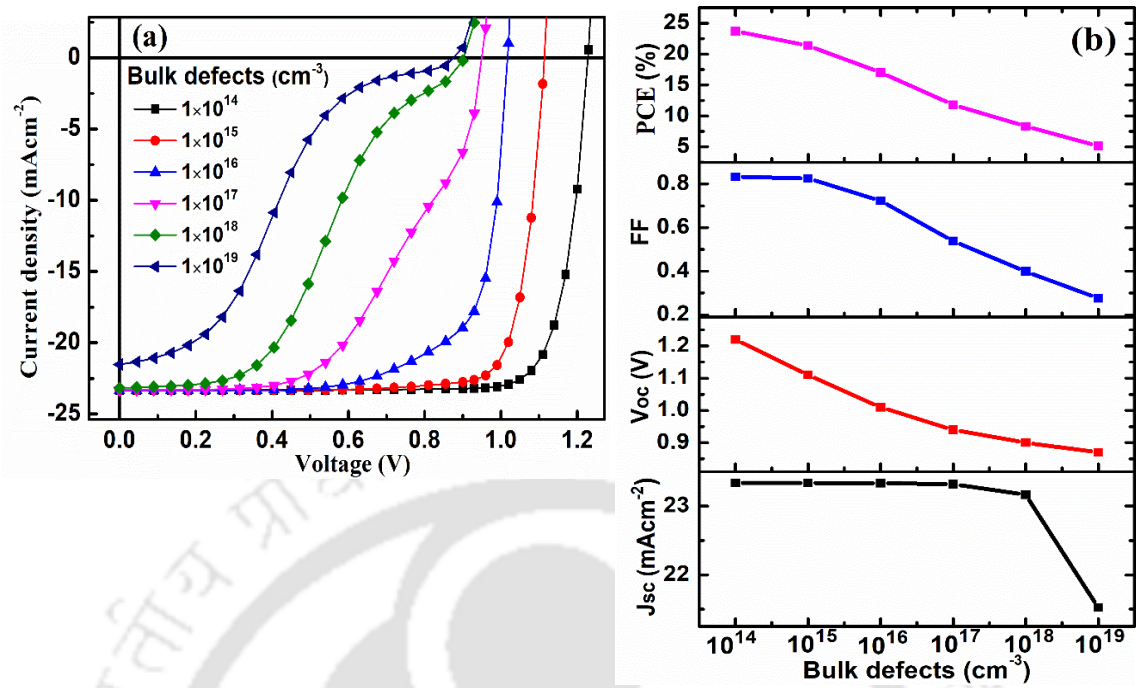

Figure 6.2: *(a) J-V characteristics of the n-i-p PSC (FTO/SnO_2/$MAPbI_3$/Spiro-OMeTAD/Ag) as a function of bulk defect density in the perovskite layer (b) Solar cell performance parameters (J_{sc}, V_{oc}, FF and PCE) variation at different defect densities in the absorber layer*

At defect density above 1×10^{17} cm^{-3}, the device exhibit s-shaped *J-V* characteristics [Fig. 6.2(a)]. In literature, several factors, such as a mismatch between the energy levels of the absorber layer and the charge transport layers leading to a barrier for charge extraction, chemical degradation of the metal contact and low temperature, are ascribed to the s-shaped *J-V* curve frequently observed in PSC [19, 20]. Fig. 6.3 shows the energy band diagrams of the device at different bulk defect densities, and the figure insets show the varying band offsets at the ETL/ $MAPbI_3$ and $MAPbI_3$/HTL interfaces. At the defect density of 1×10^{19} cm^{-3} the spike type barrier height at the ETL/$MAPbI_3$ interface (Fig. 6.3 inset) increases by ~ 0.13 eV, with a difference of ~ 0.27 eV between the tip of the spike and the CB of $MAPbI_3$, which impeded the transfer of photogenerated electrons from perovskite to ETL significantly, resulting in a decrease in J_{sc}, V_{oc} and *FF*. Likewise, kink formation is observed at the $MAPbI_3$/HTL (VB offset) interface with the increase in defect

density, hindering the hole transport from $MAPbI_3$ to HTL. The difference between the valence band of $MAPbI_3$ and the tip of the spike increases by ~ 0.10 eV with an increase in bulk defect density to 1×10^{19} cm^{-3}. Thus, the increased barrier in charge extraction with bulk defect density in the perovskite layer causes the s-shaped *J-V* curve [19, 21]. Simultaneously with the increasing defect density, the recombination rate of the photo-generated carriers increases, which shortens the carrier lifetime [22]. Thus, the diffusion length of charge carriers decreases, leading to reduced J_{sc}, V_{oc} and *FF* values [19, 22, 23].

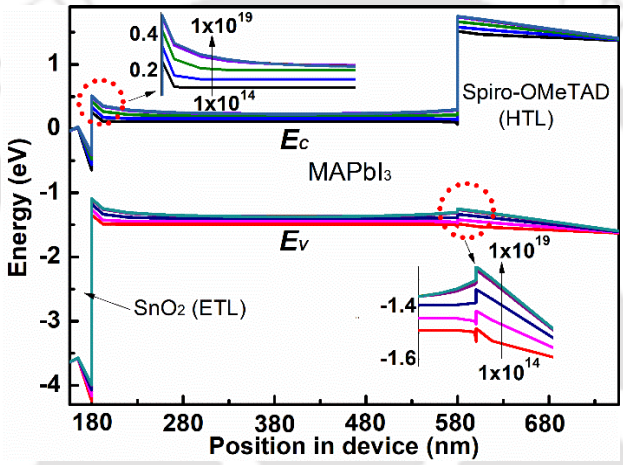

Figure 6.3: *Energy band diagram of the n-i-p PSC at different bulk defect densities of $MAPbI_3$ layer varying from 1×10^{14} to 1×10^{19} cm^{-3}*

When the defect density is raised to 1×10^{19} cm^{-3}, the J_{sc} slightly decreases to 21.52 $mAcm^{-2}$ with substantial decreases in V_{oc} to 0.87 V and *FF* to 0.27, thus reducing the efficiency from 23.72% to 5.16%. From these results, it can be concluded that the defect density of the order 10^{14} cm^{-3} is the optimal value for achieving high efficiency device. These simulation results follow a similar trend to earlier reports [24, 25]. The defect density in the range of 10^{16}-10^{17} cm^{-3} within the bandgap region contributes to the monomolecular recombination [26], as the defects at deep energy levels in the bandgap region act as Shockley-Read-Hall non-radiative recombination centers [17, 18, 26]. However, the defect levels nearer to perovskite E_c (shallow defects) have a lower adverse

effect on performance than the deep defects in the midgap region (0.8 eV below $E_c = E_g/2$) [27]. Thus, reducing the deep defects and maintaining the defect density of the order 10^{14} cm^{-3} in the perovskite absorber layer is essential for improving solar cell performance.

6.2.1.2 Influence of interface defect density on solar cell performance

The interface quality is another critical factor determining the performance of a solar cell. The interface quality between the perovskite absorber layer and charge transport layers is an important factor determining the V_{oc} and *FF* of a solar cell [1]. Therefore, the influence of interface defect density at both the interfaces of the perovskite layer, i.e., ETL/$MAPbI_3$ and $MAPbI_3$/HTL, is studied by varying the defect densities from 1×10^{6} cm^{-2} to 1×10^{12} cm^{-2} at an optimal bulk defect density of 1×10^{14} cm^{-3} (obtained from previous simulation series). The *J-V* characteristics and device performance at different interface defect densities are shown in Fig. 6.4(a-b).

It is observed that the interface defect density up to 1×10^{8} cm^{-2} has no significant impact on the overall cell performance. From the defect density of 1×10^{9} cm^{-2} onwards, the V_{oc}, and *PCE* start deteriorating. The *FF* value slightly increases from 0.83 to 0.86 at a defect density of 1×10^{9} cm^{-2} due to the improvement of squareness in the *J-V* curve as the V_{oc} decreases. As the defect density is increased further (>1×10^{9} cm^{-2}), the *FF* again starts deteriorating. The J_{sc} remains almost constant till the maximum applied defect density of 10^{12} cm^{-2}; however, if we increase the defect density further, the J_{sc} starts decreasing (not shown here). The best efficiency of 23.76% is achieved at a defect density of 1×10^{6} cm^{-2}, with a high V_{oc} of 1.22 V, J_{sc} of 23.33 $mAcm^{-2}$, and *FF* of 0.83. At the maximum interface defect density of 1×10^{12} cm^{-2} the V_{oc} , *FF* and PCE decrease to 0.98 V, 0.63 and 14.6% due to losses at the interface. These results show that the interface's trap density should be below 1×10^{7} cm^{-2} to achieve good device performance. It has also been found that at the

low trap density, the change of trap energy level has no considerable impact on efficiency [28]. Hence, low defects at the interfaces are essential for a high-efficiency device. Experimental procedures, such as defect passivation and interface modification, can effectively reduce the interface traps to improve the device efficiency [9].

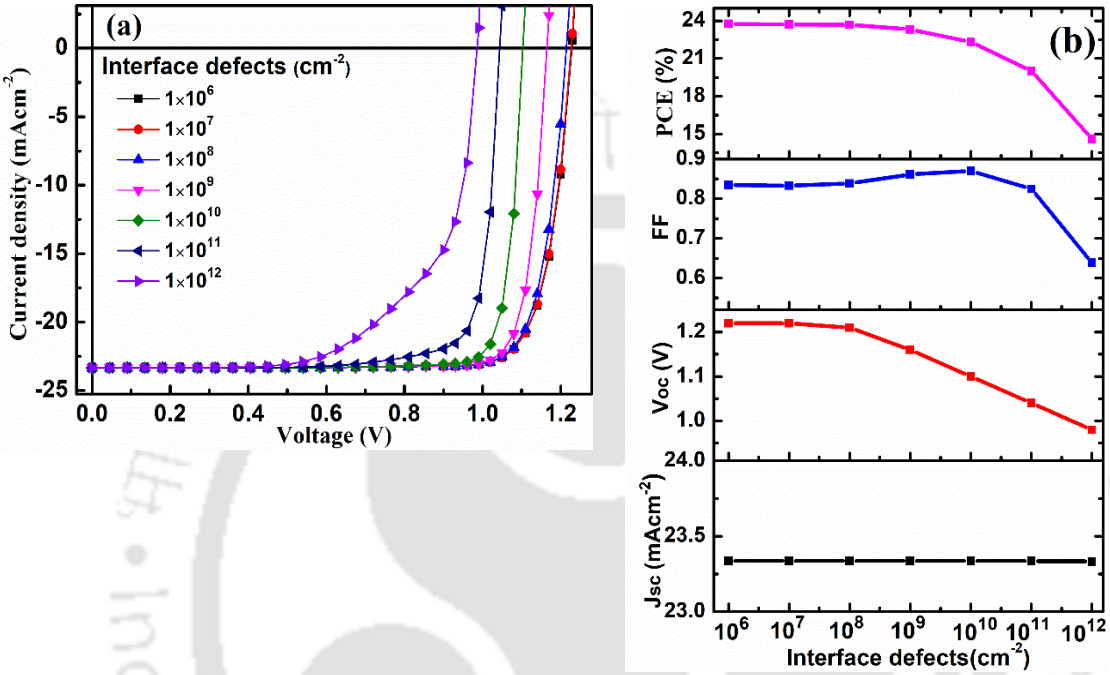

Figure 6.4: *(a) J-V characteristics of n-i-p PSC at different interface defect densities (b) variation of device performance parameters at different interface defect densities*

6.2.1.3 Influence of absorber layer thickness on solar cell performance

The influence of the absorber layer thickness is investigated by changing it from 200 nm to 1000 nm at optimum bulk defects and interface defects of 1×10^{14} cm^{-3} and 1×10^{7} cm^{-2}, respectively. We considered the interface defect density = 1×10^{7} cm^{-2} because this is close to the reported defect density and the cell performance is almost the same as observed for the defect density of 1×10^{6} cm^{-2} (Fig. 6.4(b)) [15]. Fig. 6.5(a-b) shows the *J-V* characteristics for perovskite layer thickness variation from 200 nm to 1000 nm. The absorption of $MAPbI_3$ film estimated for different film thicknesses at λ = 600 nm (α = 1×10^{5} cm^{-1}) is shown in Fig 6.6.

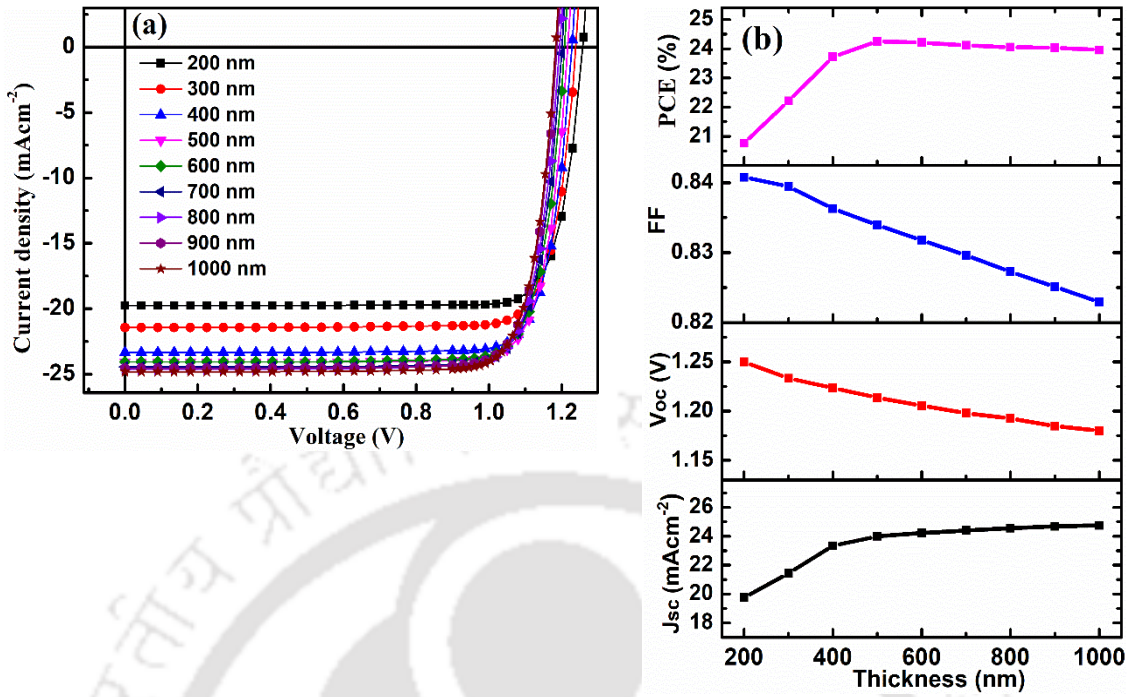

Figure 6.5: *(a) J-V characteristics of n-i-p PSC with different thicknesses of the absorber layer (b) variation of device performance parameters with different thicknesses of the absorber layer*

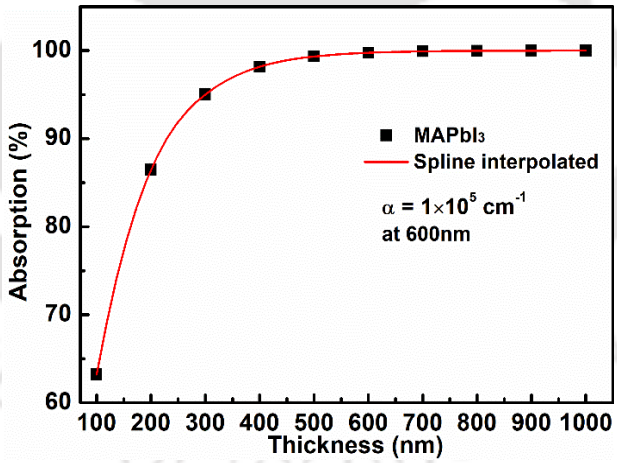

Figure 6.6: *Absorption of $MAPbI_3$ film with respect to film thickness at 600 nm ($\alpha = 1\times10^5$ cm^{-1}). The α is determined from the extinction coefficient (k) using the relation, $\alpha = 4\pi k/\lambda$*

Initially, the J_{sc} value increases with absorber layer thickness up to 500 nm, corresponding to the generation of more *e-h* (electron-hole) pairs due to increasing light absorption; it then saturates from 600 nm onwards, consistent with the absorption graph as shown in Fig 6.6. The film thickness of about 500-600 nm fully absorbs the light; thus, the absorption

saturates after ~ 600 nm. The highest PCE of 24.26% with J_{sc} = 24.07 mAcm^{-2}, V_{oc} = 1.21 V and *FF* = 0.83 is obtained at 500 nm, which implies that this thickness is optimum for sufficient light absorption and charge carriers from the perovskite layer are efficiently extracted. Further increase in absorber layer thickness (>500 nm) reduces the PCE due to the decline in V_{oc} and *FF* values. Because, for the thick absorber layer, the charge carrier collection at the respective electrode decreases as the transfer route of the photo-generated carriers increases; thus, the recombination rate increases, consequently reducing V_{oc} [29]. The slight decrease in V_{oc} (~70 mV) with the thickness is ascribed to the increment in the dark saturation current due to an increase in the recombination of the charge carriers [30]. This can be explained by the relation given in Eq. 6.3, showing the dependency of V_{oc} on the photo-generated current and dark saturation current.

$$V_{oc} = \frac{kT}{q} ln\left(\frac{J_{sc}}{J_o} + 1\right) \tag{6.3}$$

where kT/q is the thermal voltage, J_{sc} is the photo-generated current density, and J_o is the dark saturation current density.

The FF drops with absorber layer thickness due to an increase in series resistance. Ideally, the absorber layer thicknesses should be slightly less than the diffusion length (L_d) of carriers to efficiently extract the photogenerated carriers before recombining. The diffusion length of charge carriers depends on the lifetime (τ) and the mobility (μ) of carriers. The lifetime and mobility depend on film crystallinity, grain size and grain boundaries determined by chemical composition and perovskite processing technique [31]. The achieved J_{sc}, V_{oc} and *PCE* values at an optimum absorber layer thickness of 500 nm are higher than recently reported $MAPbI_3$ based solar cells [2, 3, 32, 33].

External quantum efficiency (EQE) is another essential characteristic for evaluating solar cell performance, which is defined as the ratio of electrons extracted from the solar cell

and incident photon flux on the solar cell. Fig 6.7 shows the EQE of $MAPbI_3$ PSC at different thicknesses of perovskite layers.

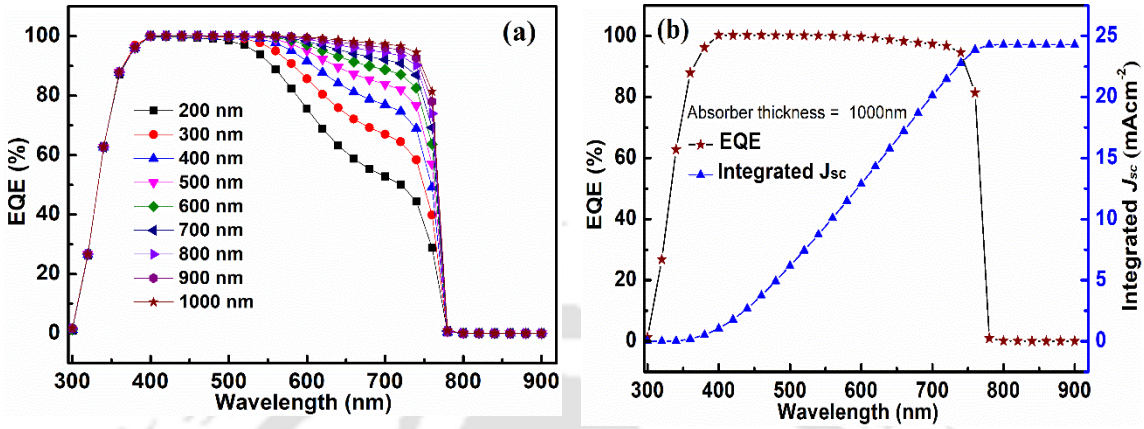

Figure 6.7: *(a)External Quantum efficiency (EQE) of $MAPbI_3$ solar cells with respect to absorber layer thickness variation (200 - 1000 nm) (b) EQE curve and integrated current density of perovskite solar cell at an absorber layer thickness of 1000 nm*

The EQE curve is almost constant up to 500 nm and at long wavelength > 500 nm, the EQE increases with perovskite thickness. This is because, when the absorber layer thickness is low, high-energy photons (< 500 nm) having high absorption coefficients are fully absorbed, whereas the fraction of low energy (high λ > 500 nm) photons with low absorption coefficients remains unabsorbed and does not generate *e-h* pairs. As the thickness increases, a larger fraction of the low-energy photons is absorbed, generating more *e-h* pairs and then enhancing the short circuit current and EQE of the long λ region of the spectrum. However, at higher thickness above 500 nm, the EQE value gradually saturates, which means the further increase of photo absorption is much smaller and this is consistent with the absorption graph shown in Fig 6.5. Thus, the increase of J_{sc} value with thickness is well correlated with EQE. The EQE curve cuts off sharply at ~775 nm (1.6 eV) due to band edge absorption corresponding to the bandgap energy (1.6 eV) of $MAPbI_3$ perovskite. Fig 6.7(b) shows that the integrated J_{sc} (~24.29 $mAcm^{-2}$) based on the

EQE spectra is consistent with the J_{sc} value (~24.76 mAcm^{-2}) obtained from the *J-V* curve [Fig 6.5(b)].

6.2.2 Simulation results of *FTO/PEDOT:PSS/MAPbI$_3$/PCBM/Ag* (p-i-n) solar cells

6.2.2.1 Influence of bulk defect density on solar cell performance

Fig. 6.8(a). shows the *J-V* characteristics of the inverted structure (p-i-n) PSC (*FTO/PEDOT:PSS/MAPbI$_3$/PCBM/Ag*) at varying bulk defect densities in the absorber layer. In this series of simulations, the effect of defect density in the perovskite layer is analyzed by varying the defect density from 1×10^{14} to 1×10^{19} cm^{-3} at a constant interface defect density of 1×10^{6} cm^{-2}. The other constant parameters are given in Table 6.1 and 6.2. It is observed that the cell performance starts declining at the defect density of 1×10^{15} cm^{-3}, and as it is increased further, the cell performance starts deteriorating substantially. Fig. 6.8(b) shows the variations in solar cell performance parameters J_{sc}, V_{oc}, *FF* and *PCE* at different defect densities. The V_{oc}, *FF*, and PCE start deteriorating as the defect density increases above 1×10^{15} cm^{-3}, while J_{sc} remains constant until 1×10^{17} cm^{-3} and eventually decreases at higher defect density. The highest efficiency of 21.91 % is achieved at a defect density of 10^{14} cm^{-3}, with a high V_{oc} of 1.22 V, J_{sc} of 21 mAcm^{-2}, and *FF* of 0.85. At the highest defect density of 1×10^{19} cm^{-3} the J_{sc}, V_{oc}, *FF* and PCE decreases to 9.65 mAcm^{-2}, 0.71 V, 0.39 and 2.72%, respectively, due to an increase in the recombination rate of charge carriers, as discussed already. However, unlike in n-i-p cells, the s-shaped *J-V* curve is not observed at high defect density. Fig 6.9 shows the energy band diagram at different defect densities and the figure insets show the enlarged image of the band offsets at the interfaces of $MAPbI_3$. The figure insets show that the kink at the $MAPbI_3$/ETL interface slightly increases by ~ 0.10 eV at the defect density of 1×10^{19} cm^{-3}. Also, the difference between the spike tip and VB of $MAPbI_3$ at the $MAPbI_3$/HTL

interface slightly increases by ~ 0.03 eV at the maximum defect density of 1×10^{19} cm^{-3}. These slight changes in band offsets did not significantly hinder the charge flow from $MAPbI_3$ to charge transport layers; thus, the s-shape *J-V* curve is not observed for this cell configuration, although the performance degrades with the increase in defect density.

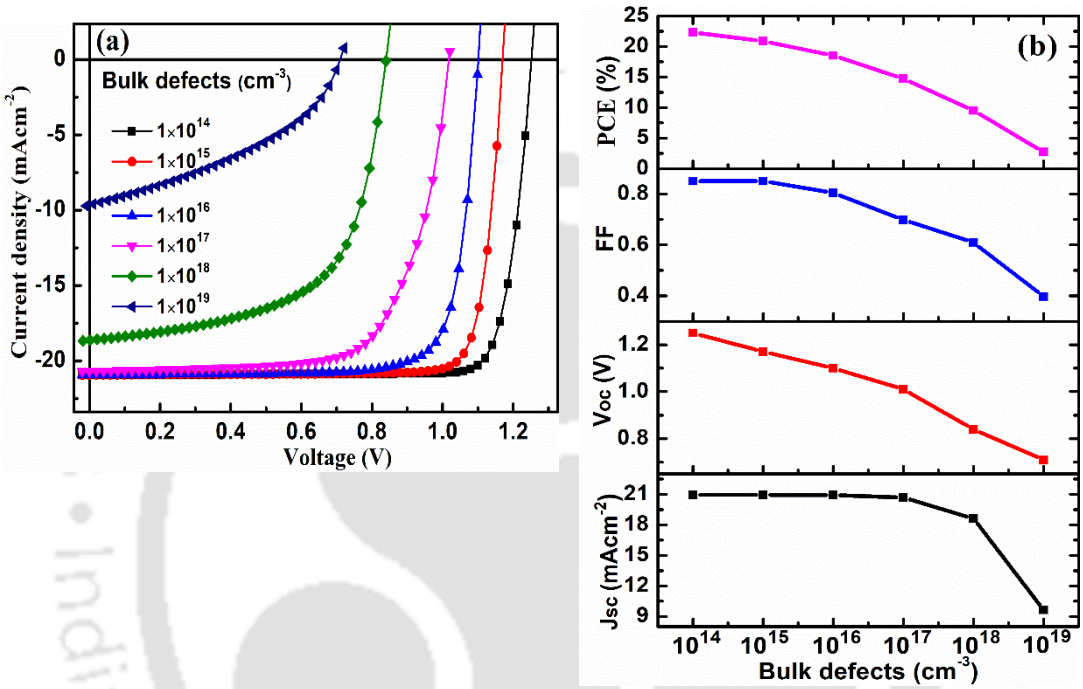

Figure 6.8: *(a) J-V characteristics of the p-i-n PSC (FTO/PEDOT:PSS/$MAPbI_3$/PCBM/Ag) as a function of defect densities in the perovskite layer (b) Solar cell performance parameters (J_{sc}, V_{oc}, FF and PCE) variation at different defect densities in the absorber layer*

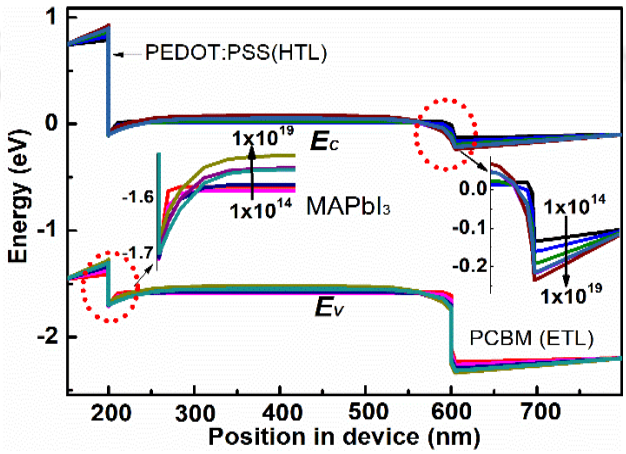

Figure 6.9: *Energy band diagram of the p-i-n PSC at different bulk defect densities of $MAPbI_3$ layer varying from 1×10^{14} to 1×10^{19} cm^{-3}*

6.2.2.2 Influence of interface defect density on solar cell performance

In this series of simulations, the influence of interface defect density at both the interfaces of the $MAPbI_3$ layer, i.e., ETL/$MAPbI_3$ and $MAPbI_3$/HTL, is studied by varying the defect densities from 1×10^{6} cm^{-2} to 1×10^{12} cm^{-2} at a constant bulk defect density of 1×10^{14} cm^{-3}. The *J-V* characteristics and device performance at various interface defect densities are shown in Fig. 6.10(a-b).

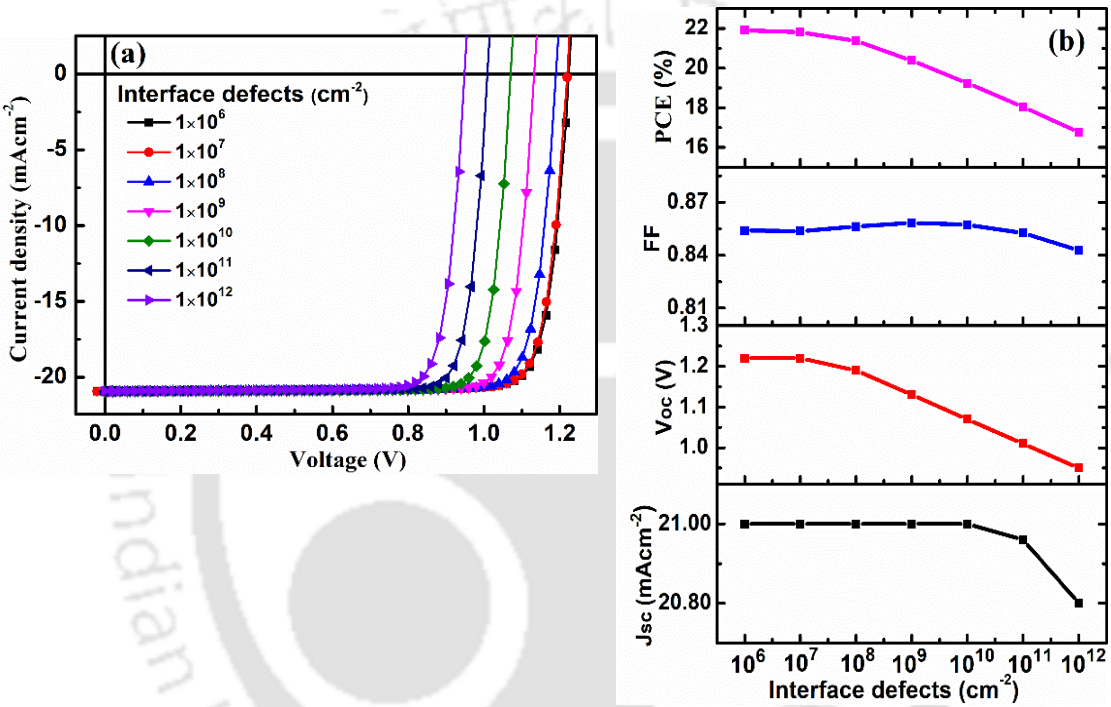

Figure 6.10: *(a) J-V characteristics of p-i-n PSC at different interface defect densities (b) variation of device performance parameters at different interface defect densities*

Defect density up to 1×10^{7} cm^{-2} has an insignificant impact on the overall cell performance and shows a PCE of 21.81% with a high V_{oc} of 1.22 V, J_{sc} of 21 $mAcm^{-2}$, and *FF* of 0.85. With a further increase in the defect density above 1×10^{8} cm^{-2}, the V_{oc} and *PCE* deteriorate faster than J_{sc} and *FF*. At the maximum defect density of 1×10^{12} cm^{-2} the J_{sc}, V_{oc} and PCE decrease to 20.80 $mAcm^{-2}$, 0.95 V and 16.76%, respectively. Though the J_{sc} is least affected by the given range of interface defects, it starts to decline faster at a higher concentration of defects. As discussed earlier, defects passivation and interface modification can effectively reduce the carrier recombination to reduce losses at the

interfaces. Interfacial engineering of the transport layer interface is a promising route to suppress non-radiative recombination in perovskite devices and compensates for a non-ideal band alignment at the interface [34].

6.2.2.3 Influence of absorber layer thickness on solar cell performance

In this simulation series, the absorber layer thickness has been varied from 200 nm to 1000 nm at an interval of 100 nm. Fig. 6.11(a-b) shows the *J-V* characteristics of absorber layer thickness variation from 200 nm to 1000 nm at optimum bulk and interface defects of 1×10^{14} cm^{-3} and 1×10^{7} cm^{-2}.

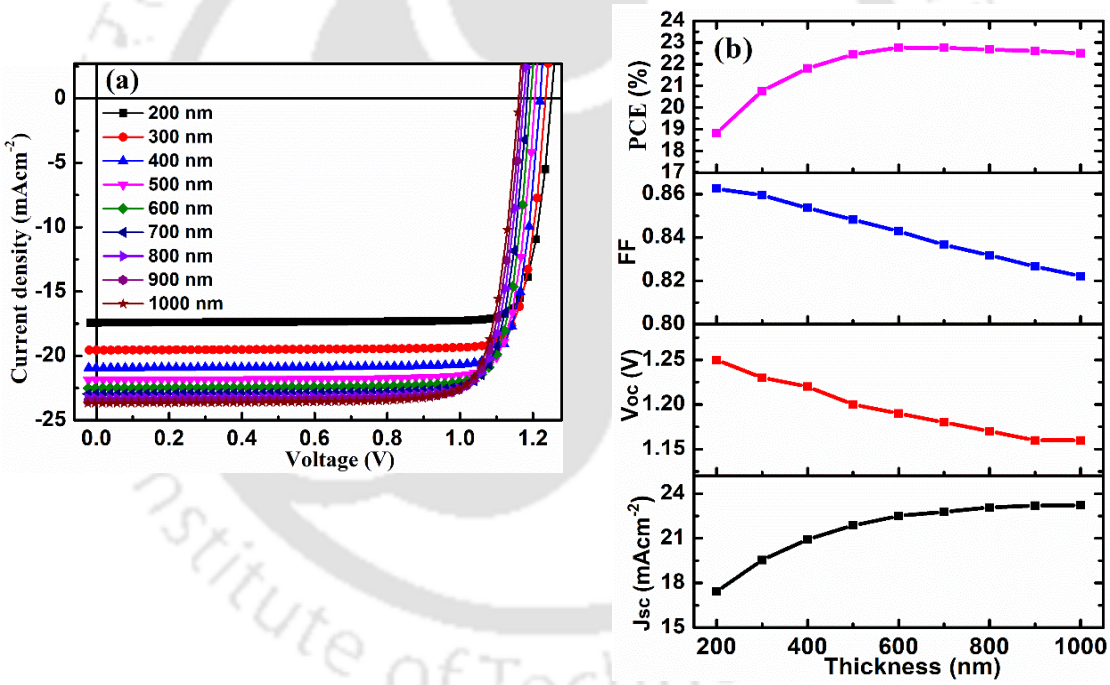

Figure 6.11: *a) J-V characteristics of p-i-n PSC with different thicknesses of the absorber layer (b) variation of device performance parameters with different thicknesses of the absorber layer*

It is observed in Fig 6.11(b) that the J_{sc} value increases linearly with thickness till 600 nm and then slowly saturates at higher thickness. Since the absorber material ($MAPbI_3$) is the same in both cell configurations, the variation in J_{sc} is similar to that in the n-i-p PSC and consistent with the light absorption pattern of $MAPbI_3$ at different thicknesses (Fig 6.6).

The simulation results show the best PCE of 22.77 % for the absorber layer thickness of 600 nm, with V_{oc} = 1.19 V, J_{sc} = 22.51 mAcm^{-2}, and *FF* = 0.84. When the perovskite (absorber) thickness is increased further, the PCE decreases due to the reduction in V_{oc} and *FF*, as discussed for the n-i-p configuration device. The best PCE in this simulation study is higher than the recently reported $MAPbI_3$ based inverted PSC [34, 35].

Fig 6.12(a) shows the EQE of p-i-n PSC with different thicknesses of perovskite layers. In the low wavelength region <500 nm, no change in EQE is observed; however, it is enhanced in the wavelength region >500 nm, corresponding to higher photon absorption with increasing absorber layer thickness.

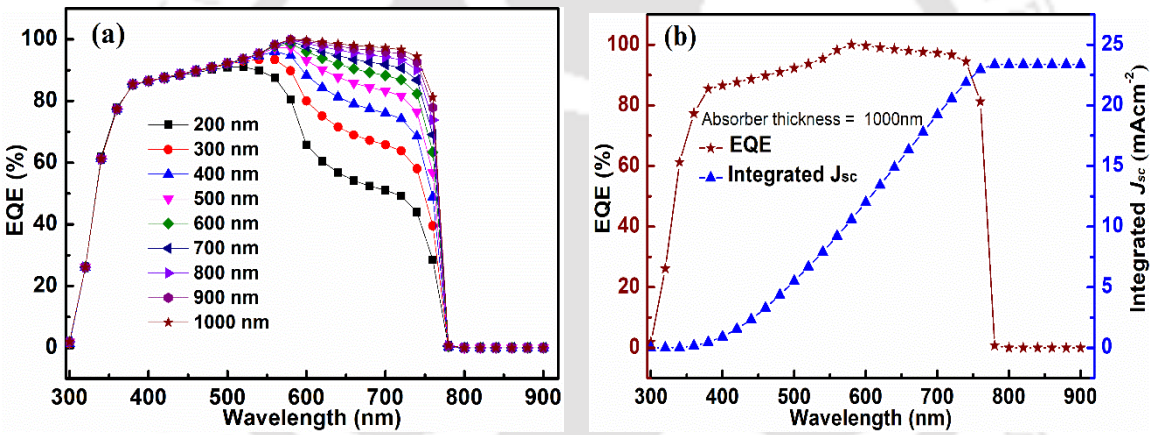

Figure 6.12: *(a) External Quantum efficiency (EQE) of perovskite solar cell with respect to absorber layer thickness variation (200 nm- 1000 nm) (b) EQE and integrated current density of perovskite solar cell at an absorber layer thickness of 1000 nm*

Similar to the n-i-p configuration cell, the EQE increases very slowly after the thickness of 500 nm in the long-wavelength region (>500 nm). This variation in EQE is consistent with the variation in J_{sc} values with respect to thickness and cuts off at ~775 nm (1.6 eV) due to band edge absorption of $MAPbI_3$ perovskite. Below 500 nm, the EQE declines due to parasitic absorption of PEDOT:PSS corresponding to its bandgap energy ~ 2.2 eV. Although reducing the PEDOT:PSS thickness can slightly enhance the EQE and cell efficiency; but, it is difficult to practically achieve a quality film of thickness less than

50 nm. Thus, the thickness of PEDOT:PSS is kept at 50 nm, which is often considered in the simulation and fabrication of PSC as well. Fig 6.12(b) illustrates that the integrated J_{sc} (~23.38 $mAcm^{-2}$) based on the EQE spectra agrees well with the J_{sc} value (~23.52 $mAcm^{-2}$) from the *J-V* curve [Fig 6.11(b)].

6.3 Comparative analysis of the simulation results of n-i-p and p-i-n solar cell configuration

The simulation results (J_{sc}, V_{oc}, *FF*, and *PCE*) of n-i-p and p-i-n structure PSC at varying bulk defects density, interface defects density and absorber layer thickness variation are listed in Table 6.3. While varying one parameter the other two are kept at constant values.

Table 6.3: *Solar cell parameters (J_{sc}, V_{oc}, FF, and PCE) of n-i-p and p-i-n structure PSC at varying bulk defects density, interface defects density and absorber layer thickness variation*

Parameters	J_{sc} ($mAcm^{-2}$)		V_{oc} (V)		*FF*		*PCE* (%)	
Bulk defects (cm^{-3})	Interface defects = 1×10^6 cm^{-2} & Thickness = 400 nm							
	n-i-p	p-i-n	n-i-p	p-i-n	n-i-p	p-i-n	n-i-p	p-i-n
1×10^{14}	23.33	21	1.22	1.22	0.83	0.85	23.72	21.91
1×10^{15}	23.33	20.94	1.11	1.16	0.82	0.85	21.39	20.87
1×10^{16}	23.33	20.91	1.01	1.10	0.72	0.80	17.04	18.53
1×10^{17}	23.31	20.68	0.94	1.01	0.53	0.69	11.80	14.71
1×10^{18}	23.16	18.62	0.90	0.84	0.39	0.60	8.32	9.54
1×10^{19}	21.52	9.65	0.87	0.71	0.27	0.39	5.16	2.72
Interface defects (cm^{-2})	Bulk defects = 1×10^{14} cm^{-3} & Thickness = 400 nm							
1×10^6	23.33	21	1.22	1.22	0.83	0.85	23.72	21.91
1×10^7	23.33	21	1.22	1.22	0.83	0.85	23.71	21.81
1×10^8	23.33	21	1.21	1.19	0.83	0.85	23.68	21.37
1×10^9	23.32	20.94	1.16	1.13	0.86	0.85	23.31	20.38
1×10^{10}	23.32	20.94	1.10	1.07	0.86	0.85	22.33	19.24
1×10^{11}	23.31	20.96	1.04	1.01	0.82	0.85	20.01	18.04
1×10^{12}	23.30	20.80	0.98	0.95	0.63	0.84	14.60	16.76
Thickness (nm)	Bulk defects = 1×10^{14} cm^{-3} & Interface defects = 1×10^7 cm^{-2}							
200	19.75	17.42	1.25	1.25	0.84	0.86	20.77	18.82
300	21.44	19.55	1.23	1.23	0.83	0.85	22.21	20.77
400	23.33	21	1.22	1.22	0.83	0.85	23.71	21.81
500	24	21.87	1.21	1.20	0.83	0.84	**24.26**	22.45
600	24.22	22.51	1.20	1.19	0.83	0.84	24.21	**22.77**
700	24.39	22.96	1.19	1.18	0.82	0.83	24.11	22.76
800	24.56	23.28	1.19	1.17	0.82	0.83	24.05	22.68
900	24.69	23.51	1.18	1.16	0.82	0.82	24.03	22.61
1000	24.76	23.52	1.18	1.16	0.82	0.82	23.96	22.51

The simulation results show that the impact of the bulk defect density variation on the *J-V* characteristics is different for n-i-p and p-i-n PSC. While increasing the defect density beyond 1×10^{17} cm^{-3}, the significant increase of energy barrier at the interfaces (ETL/$MAPbI_3$ & $MAPbI_3$/HTL) causes s-shaped *J-V* curve in n-i-p cells, whereas p-i-n cells did not show an s-shaped *J-V* curve due to lower barrier height at the interfaces. The light enters through SnO_2 in n-i-p PSC, so the *e-h* pair generation is more near the SnO_2/$MAPbI_3$ junction and in p-i-n structure, the *e-h* pair generation is more near the PEDOT:PSS/$MAPbI_3$ junction as the light enters through PEDOT:PSS. So, the J_{sc} of p-i-n cells is lower than n-i-p cells due to absorption losses in PEDOT:PSS (2.2 eV), corresponding to its lower bandgap than SnO_2 (3.6 eV). As discussed earlier, the increase in defect density (in $MAPbI_3$) reduces the carrier mobility, so the overall carrier transport gets more affected in p-i-n configuration due to the lower mobility of the charge carrier in PEDOT:PSS than SnO_2. Thus the impact of defects on J_{sc} of p-i-n structure is more pronounced at a high defect density of 1×10^{18} cm^{-3}. However, for both structures, the V_{oc} and *FF* vary in a similar fashion and are approximately in the same range. The *PCE* is slightly higher for n-i-p structure than p-i-n cell due to the higher J_{sc} value of n-i-p cell, as both cells have almost the same V_{oc} and *FF* values. In both cell configurations, the efficiency enhances almost linearly by reducing the bulk defect density.

The interface defect density variation has almost a similar role in both cell structures. The V_{oc}, *FF* and *PCE* decrease with increasing interface defects. Though the J_{sc} remains almost constant in the specified range for both cell types, it decreases at the higher defect density $>1\times10^{13}$ cm^{-2}. During thickness variation, initially, the J_{sc} values increase with the thickness and then slowly saturate from 500 nm to 600 nm onwards in both the cell types, whereas the V_{oc} decreases slightly by 70 mV and 90 mV with thickness. The V_{oc} and *FF* decrease with thickness because of increasing recombination in the perovskite layer and

an increase in series resistance. The PCE reaches the highest at the optimum thickness and decreases again with a further increase in thickness. At the optimized parameters, the n-i-p cell shows the best efficiency of 24.26%, which is higher than the p-i-n cell with an efficiency of 22.77%. For n-i-p cells, the best efficiency is obtained at an optimum absorber layer thickness of ~ 500 nm, whereas for p-i-n best efficiency is achieved at ~600 nm, perhaps due to parasitic absorption loss in PEDOT:PSS. Likewise, the EQE is slightly higher in n-i-p cells in the low wavelength region <500 nm. Thus the n-i-p cell having the structure *FTO/SnO_2/$MAPbI_3$/Spiro-OMeTAD/Ag* is superior in efficiency to p-i-n (*FTO/PEDOT:PSS/$MAPbI_3$/PCBM/Ag*) structure device. Further investigation of the influence of varying various parameters, such as thickness, doping concentration, etc., on the charge transport layers will unveil more information. Both the cell structures are widely studied with numerous modifications in the device structure to investigate their performance and enhance their efficiency and stability.

6.4 Conclusion

We studied the effect of different critical parameters on n-i-p and p-i-n structure $MAPbI_3$ solar cells using the Sentaurus-TCAD simulation tool. The impact of density of bulk defects and interface defects and absorber layer thickness on the performance of PSC is investigated and optimal values of the parameters are found to obtain high-efficiency perovskite solar cells. The results show that both types of defects have a crucial role in device performance. Decreasing the density of defects can significantly improve the device's performance. The simulation results from this investigation suggest that maintaining the bulk trap density of less than 1×10^{15} cm^{-3} is key to high-efficiency solar cells and avoiding the s-shape in the *J-V* curve. In addition, reducing interface defect densities below 1×10^{7} cm^{-2} can effectively improve cell performance. So, to have a high-

efficiency PSC, both bulk and interface traps should be optimized simultaneously. Thus increasing crystallinity of the absorber layer by careful control of the growth conditions and mitigation of interface defects by passivation are essential for increasing device efficiency. It is found that absorber layer thickness ~500-600 nm is optimum for obtaining high-efficiency $MAPbI_3$ solar cells. At optimized device parameters the n-i-p configuration PSC (*FTO/SnO_2/$MAPbI_3$/Spiro-OMeTAD/Ag*) show the best PCE of 24.26% at optimal absorber layer thickness of 500 nm, with high V_{oc} = 1.21 V, J_{sc} = 24.07 $mAcm^{-2}$, and *FF* = 0.83. In p-i-n configuration (*FTO/PEDOT:PSS/$MAPbI_3$/PCBM/Ag*), the best PCE of 22.77 % is obtained for the absorber layer thickness of 600 nm, with V_{oc} = 1.19 V, J_{sc} = 22.51 $mAcm^{-2}$, and *FF* = 0.84. This study provides some guidelines that can help boost the efficiency of this type of cells.

6.5 References

1. Kumar, R.R., S.K.J.S. Pandey, and Microstructures, *Performance evaluation and material parameter perspective of eco-friendly highly efficient CsSnGeI3 perovskite solar cell.* Superlattices and Microstructures, 2019. **135**: p. 106273.
2. Wang, F., et al., *Toward efficient, moisture-resistant and lead-leakproofness perovskite solar cells: Coordination-driven reconstructing homogeneous amorphous perovskitoid/crystalline perovskite photoabsorber*. Chemical Engineering Journal, 2022. **428**: p. 132528.
3. Xie, L., et al., *Fluorinated Oligomer Wrapped Perovskite Crystals for Inverted $MAPbI_3$ Solar Cells with 21% Efficiency and Enhanced Stability*. ACS Applied Materials & Interfaces, 2021. **13**(22): p. 26093-26101.
4. Ball, J.M. and A.J.N.E. Petrozza, *Defects in perovskite-halides and their effects in solar cells.* Nature Energy, 2016. **1**(11): p. 1-13.
5. Montoya De Los Santos, I., et al., *Optimization of $CH_3NH_3PbI_3$ perovskite solar cells: A theoretical and experimental study.* Solar Energy, 2020. **199**: p. 198-205.
6. Wu, J., et al., *DMF as an additive in a two-step spin-coating method for 20% conversion efficiency in perovskite solar cells.* ACS applied materials & interfaces, 2017. **9**(32): p. 26937-26947.
7. Chang, J., et al., *Boosting the performance of planar heterojunction perovskite solar cell by controlling the precursor purity of perovskite materials.* Journal of Materials Chemistry A, 2016. **4**(3): p. 887-893.

8. Baloch, A.A., et al., *Practical efficiency limit of methylammonium lead iodide perovskite ($CH_3NH_3PbI_3$) solar cells*. The Journal of Physical Chemistry Letters, 2018. **9**: p. 426-434.

9. Basumatary, P. and P. Agarwal, *A short review on progress in perovskite solar cells.* Materials Research Bulletin, 2022. **149**: p. 111700.

10. Yang, G., et al., *Recent progress in electron transport layers for efficient perovskite solar cells.* Journal of Materials Chemistry A, 2016. **4**(11): p. 3970-3990.

11. Jiang, Q., et al., *Enhanced electron extraction using SnO_2 for high-efficiency planar-structure $HC(NH_2)_2PbI_3$-based perovskite solar cells.* Nature Energy, 2016. **2**(1): p. 1-7.

12. Zhao, P., et al., *Numerical simulation of planar heterojunction perovskite solar cells based on SnO_2 electron transport layer.* ACS Applied Energy Materials, 2019. **2**(6): p. 4504-4512.

13. Xiong, L., et al., *Review on the Application of SnO_2 in Perovskite Solar Cells.* Advanced Functional Materials, 2018. **28**(35): p. 1802757.

14. Mandadapu, U., et al., *Simulation and analysis of lead based perovskite solar cell using SCAPS-1D.* Indian Journal of Science and Technology, 2017. **10**(11): p. 65-72.

15. Chouhan, A.S., N.P. Jasti, and S. Avasthi, *Effect of interface defect density on performance of perovskite solar cell: Correlation of simulation and experiment.* Materials Letters, 2018. **221**: p. 150-153.

16. Izadi, F., et al., *Effect of interface defects on high efficient perovskite solar cells.* Optik, 2021. **227**: p. 166061.

17. Yin, W.J., T. Shi, and Y.J.A.M. Yan, *Unique properties of halide perovskites as possible origins of the superior solar cell performance.* Advanced Materials, 2014. **26**(27): p. 4653-4658.

18. Yin, W.-J., T. Shi, and Y. Yan, *Unusual defect physics in $CH_3NH_3PbI_3$ perovskite solar cell absorber.* Applied Physics Letters, 2014. **104**(6): p. 063903.

19. Saive, R., *S-Shaped Current–Voltage Characteristics in Solar Cells: A Review.* IEEE Journal of Photovoltaics, 2019. **9**(6): p. 1477-1484.

20. Werner, J., et al., *Sputtered rear electrode with broadband transparency for perovskite solar cells.* Solar Energy Materials and Solar Cells, 2015. **141**: p. 407-413.

21. Tress, W. and O. Inganäs, *Simple experimental test to distinguish extraction and injection barriers at the electrodes of (organic) solar cells with S-shaped current–voltage characteristics.* Solar Energy Materials and Solar Cells, 2013. **117**: p. 599-603.

22. Rai, S., B.K. Pandey, and D.K. Dwivedi, *Modeling of highly efficient and low cost $CH_3NH_3Pb(I_{1-x}Cl_x)_3$ based perovskite solar cell by numerical simulation.* Optical Materials, 2020. **100**: p. 109631.

23. Sundqvist, A., et al., *Origin of the S-Shaped JV Curve and the Light-Soaking Issue in Inverted Organic Solar Cells.* Advanced Energy Materials, 2016. **6**(6): p. 1502265.

24. Jamal, M.S., et al., *Effect of defect density and energy level mismatch on the performance of perovskite solar cells by numerical simulation.* Optik, 2019. **182**: p. 1204-1210.

25. Zhang, A., Y. Chen, and J. Yan, *Optimal design and simulation of high-performance organic-metal halide perovskite solar cells.* IEEE Journal of Quantum Electronics, 2016. **52**(6): p. 1-6.

26. Saba, M., et al., *Correlated electron–hole plasma in organometal perovskites.* Nature Communications, 2014. **5**(1): p. 1-10.

27. Yousefi, M., et al., *Improving the efficiency of CZTSSe solar cells by engineering the lattice defects in the absorber layer.* Solar Energy, 2020. **208**: p. 884-893.

28. Basyoni, M.S.S., et al., *On the Investigation of Interface Defects of Solar Cells: Lead-Based vs Lead-Free Perovskite.* IEEE Access, 2021. **9**: p. 130221-130232.

29. Kanoun, A.-A., et al., *Toward development of high-performance perovskite solar cells based on $CH_3NH_3GeI_3$ using computational approach.* Solar Energy, 2019. **182**: p. 237-244.

30. Ouslimane, T., et al., *Impact of absorber layer thickness, defect density, and operating temperature on the performance of $MAPbI_3$ solar cells based on ZnO electron transporting material.* Heliyon, 2021. **7**(3): p. e06379.

31. Adhyaksa, G.W.P., et al., *Understanding Detrimental and Beneficial Grain Boundary Effects in Halide Perovskites.* Advanced Materials, 2018. **30**(52): p. 1804792.

32. Tan, C., et al., *Increasing stability of SnO_2-based perovskite solar cells by introducing an anionic conjugated polyelectrolyte for interfacial adjustment.* ACS Applied Materials & Interfaces, 2021. **13**(21): p. 24575-24581.

33. Wang, F., et al., *Interface dipole induced field-effect passivation for achieving 21.7% efficiency and stable perovskite Solar cells.* Advanced Functional Materials, 2021. **31**(5): p. 2008052.

34. An, Q., et al., *Enhancing the Open-Circuit Voltage of Perovskite Solar Cells by up to 120 mV Using π-Extended Phosphoniumfluorene Electrolytes as Hole Blocking Layers.* Advanced Energy Materials, 2019. **9**(33): p. 1901257.

35. Yang, D., et al., *Stable Efficiency Exceeding 20.6% for Inverted Perovskite Solar Cells through Polymer-Optimized PCBM Electron-Transport Layers.* Nano Letters, 2019. **19**(5): p. 3313-3320.

CHAPTER 7

Conclusion and future scope

This chapter summarizes the work reported in the present thesis on the fabrication and studies on $MAPbX_3$ perovskite materials and solar cells. The thin films of $MAPbI_3$ were fabricated using one-step and two-step deposition methods and solar cells were fabricated with the optimized deposition parameters. The motivation of the present thesis work was to study methylammonium lead iodide ($MAPbI_3$) perovskite thin films for application in solar cells. Keeping that in mind, perovskite thin films were deposited by two different methods, i.e. one-step and two-step (TE+DC and SC+DC) methods using thermal evaporation (vacuum technique), spin coating and dip-coating technique. Then we studied the structural, optical and electrical properties of the perovskite thin films and with the optimized deposition parameters, p-i-n planar structure solar cells were fabricated. The stability of thin films and solar cells was checked in ambient moisture. In addition, we have also demonstrated high-efficiency $MAPbI_3$ based solar cells using the Sentaurus-

TCAD simulation tool for both n-i-p and p-i-n planar structures by optimizing the absorber layer parameters. The overall conclusion of the thesis work and future research scopes are given in the following section.

7.1 Thesis conclusion

- The structural, optical and electrical properties of $MAPbI_3$ perovskite thin films prepared by one-step solution method are studied. The luminescence properties of $MAPbI_3$ perovskite thin films are studied using photoluminescence (PL) and photoluminescence excitation (PLE) spectroscopy. The λ_{ex} variation from 500 nm to 600 nm has no significant influence on the PL peak position, though peak intensity slightly depends upon the λ_{ex} due to variation in the absorption coefficient with wavelengths.
- The deconvolution of the broad PL spectra (at 1.58 eV) reveals the presence of two peaks; an intense peak at 1.58 eV (peak1) and a small intensity peak at 1.64 eV(peak2). The peak at ~1.64 eV corresponds to the bandgap of $MAPbI_3$, whereas the high-intensity peak at photon energy ~1.58 eV is observed due to the presence of shallow trap states. The significant contribution to the PL peak (peak2) is from the radiative recombination via these shallow trap states.
- The slow decay of photocurrent observed in the transient photocurrent measurements further confirmed the presence of shallow trap states in $MAPbI_3$ perovskite. These shallow traps can be attributed to the point defects such as iodine (I) and methylammonium (MA) vacancies in $MAPbI_3$ perovskite. On further analysis, it is found that the emission from the perovskite film surface region of approximately 50-60 nm depth effectively contributes to the PL peak.

- In the two-step deposited $MAPbI_3$ films, the TE+DC films show better structural and electrical properties than the SC+DC films. As seen in the AFM images, we could achieve highly uniform PbI_2 films using the vapor deposition technique compared to the SC technique. Thus $MAPbI_3$ films prepared by TE+DC have uniform coverage and fewer pinholes than SC+DC films. The vapor-deposited PbI_2 gives perovskite films with large grains of size up to 1 μm, whereas the spin-coated PbI_2 films give smaller grain-sized (up to 500 nm) perovskite films.
- Moreover, the TE+DC films show better stability than SC+DC films. These observations indicate that TE+DC $MAPbI_3$ perovskite films are likely to show better device performance.
- The TE+DC $MAPbI_3$ perovskite films show good photosensitivity and stable transient current response in the temperature range of 25 - 70 °C. The two different decay constants obtained after fitting the current decay curve (after light off) suggest two different shallow defect levels.
- It is found that for the a given measurement condition (Temperature 25 °C, intensity = 1000 Wm^{-2} illumination time = 60 sec) the decay constant values (τ_{d1}= 0.10 s and τ_{d2} = 0.34 s) are slightly larger than the one-step deposited perovskite film (τ_{d1} = 0.07 s and τ_{d2} = 0.25 s). This means that the perovskite films prepared by the one-step method have a little shallower trap states than the two-step processed films. These shallow defects were also detected in the PL peak analysis.
- The one-step fabricated PSC showed the best efficiency (η) of ~5% with V_{oc} of 0.96 V and *FF* of 0.6 at the absorber layer thickness of ~400 nm. While varying the absorber layer thickness, it was observed that the efficiency increases with absorber layer thickness up to 400 nm and then decreases at higher thickness. The

cell performance degraded slowly while aging and even after 400 hrs (Avg *RH* ~ 45%); the PSC retained 40% of the initial cell efficiency (i.e 2.14%).

- In the two-step fabricated PSC the thin layer of ITO on ETL played an essential role by inhibiting Ag electrode diffusion into the perovskite layer through PCBM. After using the ITO interlayer, the cell performance improved drastically due to inhibition of Ag electrode diffusion and some protection from the moisture.
- Despite high relative humidity during the fabrication process and measurements, the fresh device could show the efficiency of ~8% with V_{oc} of 0.86 V, J_{sc} of 19.11 $mAcm^{-2}$ and *FF* of 0.49 at the initial condition and decreases below 1% after 200 hours. The cell efficiency can be further improved by optimizing the different layers and minimizing the devices' interfacial defects and losses. Moreover, fabrication of the devices in well-controlled humidity conditions is also expected to improve cell performance.
- In the simulation study, the influence of bulk defect density in the absorber layer, interface defects, and absorber layer thickness on device performance has been studied on n-i-p (*FTO/SnO_2/$MAPbI_3$/Spiro-OMeTAD/Ag*) and p-i-n (*FTO/PEDOT:PSS/$MAPbI_3$/PCBM/Ag*) planar configurations of $MAPbI_3$ based PSC.
- With increasing bulk defect density of absorber layer from 1×10^{12} cm^{-3} to 1×10^{19} cm^{-3}, the V_{oc} and *FF* decrease significantly, which results in a decrease in PCE.
- The interface defects variation at ETL/$MAPbI_3$ and $MAPbI_3$/HTL in the range of 1×10^{6} cm^{-2} to 1×10^{12} cm^{-2} have a similar role in both types of cell structures. The V_{oc}, *FF* and *PCE* decrease with increasing interface defects. Though the J_{sc} remains almost constant in the specified range, it decreases at the higher defect density $>1\times10^{13}$ cm^{-2}.

- During thickness variation from 200 nm to 1000 nm, the J_{sc} value increases with the thickness and then slowly saturates after 500 - 600 nm, consistent with the absorption of $MAPbI_3$ perovskite. In contrast, the V_{oc} decreases slightly (70 mV, 90 mV) with thickness in both the cell types.
- At the optimized parameters, the n-i-p cell shows the best efficiency of 24.26%, which is higher than the p-i-n cell with an efficiency of 22.77%. For n-i-p cells, the best efficiency is obtained at an optimum absorber thickness of ~ 500 nm, whereas for p-i-n best efficiency is achieved at ~ 600 nm. This difference in optimal absorber thickness is due to parasitic absorption loss in PEDOT:PSS. However, reducing the thickness of PEDOT:PSS will enhance cell efficiency.

7.2 Scope for future work

The present thesis mainly focuses on improving the efficiency of $MAPbI_3$ planar heterojunction solar cells. The present work can be extended in several ways, as described below.

- Since the device performance needs to be improved, some improvements such as minimizing the defects in the films and interfacial defects by passivating defects in the devices can enhance the device output.
- Choosing suitable ETL or HTL with proper band alignment and incorporating buffer interlayers will further improve the device's efficiency.
- Moreover, fabricating the n-i-p (*FTO/SnO_2/$MAPbI_3$/Spiro-OMeTAD/Ag*) devices with low defect density in well-controlled humidity conditions and its encapsulation will enhance the performance and lifetime.
- Using the simulation tool, tandem solar cells can be designed and simulated to achieve high-efficiency PSC.

List of publications

1. **Pilik Basumatary**, Juhi Kumari and Pratima Agarwal, "Probing the defects states in $MAPbI_3$ perovskite thin films through photoluminescence and photoluminescence excitation spectroscopy studies*" Optik, 266,* 169586 *(2022); https://doi.org/10.1016/j.ijleo.2022.169586*
2. **Pilik Basumatary** and Pratima Agarwal, "A short review on progress in perovskite solar cells" *Mater Res Bull 149:111700 (2022); https://doi.org/10.1016/j.materresbull.2021.111700*
3. **Pilik Basumatary**, Juhi Kumari and Pratima Agarwal, "Enhancing the performance and stability of $MAPbI_3$ perovskite solar cells by inserting the ITO layer before the Ag electrode" *AIP Conf. Proc. 2369, 020022 (2021); https://doi.org/10.1063/5.0061034*
4. **Pilik Basumatary** and Pratima Agarwal, "Photocurrent transient measurements in $MAPbI_3$ thin films", *J. Mater. Sci.: Mater. Electron 31, 10047–10054 (2020); https://doi.org/10.1007/s10854-020-03549-7*
5. **Pilik Basumatary** and Pratima Agarwal, "Two-step fabrication of $MAPbI_3$ perovskite thin films with improved stability", *Bull. Mater. Sci. 42:268 (2019); https://doi.org/10.1007/s12034-019-1959-1*
6. **Pilik Basumatary,** Anterdipan Singh and Pratima Agarwal, "Optimization of absorber layer parameters for high efficiency $MAPbI_3$ perovskite solar cells" (*Under review*)
7. **Pilik Basumatary** and Pratima Agarwal, "Fabrication of $MAPbI_3$ perovskite solar cells in high humidity conditions" *(manuscript under preparation)*

List of publications (*not related to thesis*)

8. Juhi Kumari, **Pilik Basumatary**, Manvendra Singh Gangwar, Pratima Agarwal, "Molybdenum oxide (MoO_{3-x}) as an emitter layer in silicon based heterojunction solar cells", *Materials Today: Proceedings 39, 5 (2020); https://doi.org/10.1016/j.matpr.2020.08.527*
9. Jai Shree Bhardwaj, **Pilik Basumatary**, Ankit Kumar Singh and Pratima Agarwal, "Comparative study of chemically and thermally reduced graphene oxide based on their specific surface area, structural and electrical properties" *AIP Conf. Proc. 2220, 020157 (2020); https://doi.org/10.1063/5.0001413*
10. Venkanna Kanneboina, **Pilik Basumatary**, and Pratima Agarwal, "Influence of deposition temperature on indium tin oxide thin films for solar cell applications'', *AIP Conf. Proc. 2091, 020016 (2019); https://doi.org/10.1063/1.5096507*
11. Shubhangi Bhardwaj, **Pilik Basumatary** and Pratima Agarwal, "Influence of argon flow rate on structural and optical properties of TiO_2 thin films deposited by RF sputtering", *AIP Conf. Proc. 1953, 100043 (2018); https://doi.org/10.1063/1.5032979*

List of papers presented in international/national conferences

1. **Pilik Basumatary,** Juhi Kumari and Pratima Agarwal, "Signature of defect states in PL spectra of $MAPbI_3$ perovskite films", *XXI International Workshop on Physics of Semiconductor Devices,* IIT Delhi, New Delhi, 14th -17th December 2021. (ID-73, page-451)

2. **Pilik Basumatary,** Juhi Kumari and Pratima Agarwal, "Enhancing the performance and stability of $MAPbI_3$ perovskite solar cells by inserting the ITO layer before the Ag electrode", *National Conference on Physics and Chemistry of Materials*, Govt. Holkar Science College, Indore, 14th-16th December 2020. (NCPCM-1044).

3. **Pilik Basumatary** and Pratima Agarwal, "Charge Carrier Dynamics in $CH_3NH_3PbI_3$ Perovskite Thin Film", *3rd International Conference on Solar Energy Photovoltaic-2019,* KIIT Bhubaneswar, Bhubaneswar, 19th - 22nd December 2019. (P-0313)

4. **Pilik Basumatary** and Pratima Agarwal, "$MAPbI_3$ perovskite solar cells using ITO as an interlayer", *Research Conclave-2019,* IIT Guwahati, Guwahati, 14th - 17th March 2019 **(Awarded best poster prize).**

5. Venkanna Kanneboina, **Pilik Basumatary**, and Pratima Agarwal, "Influence of deposition temperature on indium tin oxide thin films for solar cell applications", *International Conference on Renewable and Alternate Energy,* Assam Science and Technology University, Guwahati, 4th - 6th December 2018. (ICRAE18-077, page-50)

6. **Pilik Basumatary** and Pratima Agarwal, "Two step fabrication of $MAPbI_3$ perovskite thin films with improved stability", *Materials & Technologies for Energy Conversion and Storage,* BARC, Mumbai, 25th - 29th September 2018. (ID-3125, page-153)

7. **Pilik Basumatary**, Shubhangi Bhardwaj and Pratima Agarwal, "Large area uniform $MAPbI_3$ thin films for perovskite solar cells using two step technique", *National Conference on Advances in Spectroscopic Techniques and materials*, Indian Schools of Mines, Dhanbad, 14th to 16th March 2018. (OL-23, page-31)

8. **Pilik Basumatary** and Pratima Agarwal, "Large area $MAPbI_3$ perovskite thin films by two step method with improved stability", *XIX International Workshop on The Physics of Semiconductor Devices,* IIT Delhi, New Delhi, 11th -15th December 2017. (ID-279, page-130) **(Awarded best poster prize).**

9. Ramakrishna Madaka, **Pilik Basumatary,** V. Kanneboina, and Pratima Agarwal, "Amorphous silicon thin film solar cells fabricated on different substrates", *XIX International Workshop on The Physics of Semiconductor Devices,* IIT Delhi, New Delhi, 11th -15th December 2017. (ID-279, page-1-3) **(Awarded best poster prize).**

10. **Pilik Basumatary** & Pratima Agarwal, "Large area uniform $MAPbI_3$ thin films for Perovskite solar cells using two step technique", *17th International Conference on Thin Films,* CSIR-NPL, New Delhi, 13th-17th November 2017. (P237-K32, page-165)

11. **Pilik Basumatary** & Pratima Agarwal, "Synthesis of uniform $MAPbI_3$ thin film for large area Perovskite solar cells using thermal evaporation", *International Conference on Energy Options for Tomorrow: Technology to Sustainability,* The Neotia University, Kolkata, 17^{th}-19^{th} April 2017. (Page-19)

12. Venkanna Kanneboina, **Pilik Basumatary**, Ramakrishna M & Pratima Agarwal, "Spectroscopic Ellipsometry Investigation of Optical and Structural Properties of a-Si:H Thin films", *International Conference on Energy Options for Tomorrow: Technology to Sustainability,* The Neotia University, Kolkata, 17^{th}-19^{th} April 2017. (Page-43)

13. **Pilik Basumatary** and Pratima Agarwal, "Synthesis of uniform $MAPbI_3$ thin film for large area Perovskite solar cells using thermal evaporation and dip coating", *National Seminar on Advances in Material Science,* Gauhati University, Guwahati, 24^{th} and 25^{th} March 2017.

14. Ramakrishna Madaka, **Pilik Basumatary** and Pratima Agarwal, "Study of morphological evolution in hydrogenated amorphous silicon (a-Si:H) thin films by atomic force microscopy", *National Conference on Hard and Soft Condensed Matter Physics,* Tezpur University, Tezpur, 2^{nd} to 4^{th} March 2017

15. **Pilik Basumatary** and Pratima Agarwal, "Study of compact-TiO_2 layer for perovskite solar cell", *National Conference on Recent Advances in Nanoscience and Nanotechnology,* North-Eastern Hill University, Shillong, 8^{th} and 9^{th} September 2016. (POS-12, page-42)

List of workshops attended

1. *"5th International Conference on Emerging Electronics, IEEE-ICEE 2020"* IIT Delhi, New Delhi, 26th-28th November 2020.
2. *"Advances in Functional Materials"*, KIIT Bhubaneswar, Bhubaneswar, 26th-28th August 2020.
3. *"Photophysics of Metal Halide Perovskite: From Material to Devices"*, IIT Roorkee, Roorkee, 6th July 2020.
4. *"International Workshop & Conference on Perovskite & Hybrid Photovoltaics"*, IIT Delhi, New Delhi, 4th - 8th February 2019.
5. *"Low Voltage Direct Current (LVDC) Power Distribution Systems and its promotion",* North Eastern Council, Shillong, 18th May 2018.
6. *"4th National Workshop on NEMS/MEMS & Theranostic Devices"*, NANO workshop, IIT Guwahati, Guwahati, 26th -28th February 2018.
7. *"Training Programme on Organic Photovoltaics and Electronics Technology"*, National Physical Laboratory, New Delhi, 18th - 22nd September 2017.
8. *"One-Day Workshop on Vacuum Technology and its Application in Optical science"*, IIT Guwahati, Guwahati, 19th August 2017.
9. *"INUP Hands-on Training workshop on Nanofabrication Technologies"*, IIT Bombay, Mumbai, 20th - 24th February 2017.
10. *"National Workshop on Advanced Probing Techniques in TEM"*, IIT Guwahati, Guwahati, 15th & 16th February 2016.